

TSUNAMI INDUCED WAVE AND CURRENT AMPLIFICATION AND
SEDIMENTATION IN CLOSED BASINS

A THESIS SUBMITTED TO
THE GRADUATE SCHOOL OF NATURAL AND APPLIED SCIENCES
OF
MIDDLE EAST TECHNICAL UNIVERSITY

BY

ROZITA KIAN

IN PARTIAL FULFILLMENT OF THE REQUIREMENTS
FOR
THE DEGREE OF DOCTOR OF PHILOSOPHY
IN
CIVIL ENGINEERING

NOVEMBER 2015

Approval of the thesis:

**TSUNAMI INDUCED WAVE AND CURRENT AMPLIFICATION AND
SEDIMENTATION IN CLOSED BASINS**

submitted by **ROZITA KIAN** in partial fulfillment of the requirements for the degree of **Doctor of Philosophy in Civil Engineering Department, Middle East Technical University** by,

Prof. Dr. M. Gülbin Dural-Ünver
Dean, Graduate School of **Natural and Applied Sciences** _____

Prof. Dr. Ahmet Cevdet Yalçın
Head of Department, **Civil Engineering** _____

Prof. Dr. Ahmet Cevdet Yalçın
Supervisor, **Civil Engineering Department, METU** _____

Examining Committee Members:

Assist. Prof. Dr. Gülizar Özyurt Tarakçıoğlu
Civil Eng. Dept., METU _____

Prof. Dr. Ahmet Cevdet Yalçın
Civil Eng. Dept., METU _____

Doç. Dr. Utku Kanoğlu
Engineering Sciences., Dept., METU _____

Prof. Dr. Yalçın Yüksel
Civil Eng. Dept., Yıldız Teknik University _____

Prof. Dr. Burcu Altan Sakarya
Civil Eng. Dept., METU _____

Date: 13.11.2015

I hereby declare that all information in this document has been obtained and presented in accordance with academic rules and ethical conduct. I also declare that, as required by these rules and conduct, I have fully cited and referenced all material and results that are not original to this work.

Name, Last Name : Rozita Kian

Signature :

ABSTRACT

TSUNAMI INDUCED WAVE AND CURRENT AMPLIFICATION AND SEDIMENTATION IN CLOSED BASINS

Kian, Rozita

Ph.D., Department of Civil Engineering

Supervisor: Prof. Dr. Ahmet Cevdet Yalçiner

November 2015, 163 pages

Wave and current amplification inside the basins are related to different parameters. Wave period is one of the important parameters which governs the amplification inside the basins. If the period of incident wave coincides with one of the periods of free oscillations in the basin then resonant oscillation and amplification happens. Resonance inside harbors due to tsunami waves can exacerbate the damages by amplifying the water level changes, and currents. This phenomenon is important and cause unexpected amplifications and hence affects the harbor operations and management due to not only extreme water elevations but also morphological changes.

Generally tsunamis in shallow water zone lead to sea water level rise and fall, strong currents, forces (drag, impact, uplift, etc.), drawdown, scour, and morphological changes (erosion, deposition), debris and debris flow, dynamic water pressure, resonant oscillations and seiches. As a result ground material under the tsunami motion move and scour/erosion/deposition patterns can be observed in the region. Tsunamis carry vast amount of materials and cause morphological erosion and/or

deposition on coastal utilities inside basins and harbors. In addition tsunamis cause functional failure in the ports due to depth change and damage. Modes of sediment transport can be determined according to the Rouse number values. Sediment transport modes are in the form of bed load, suspended load and wash load.

In this study the response and behavior of water motions inside the enclosed basins under long wave conditions are investigated by using numerical model (NAMI DANCE). The spatial and temporal changes of main tsunami parameters and their adverse effects on harbor performance are studied specifically monitoring the wave and current amplifications and consequent variation of sediment motion in terms of Rouse number, In the case studies the resonance analysis in L-type basins, the effects of incident wave period and basin geometry are investigated. The possible effects of tsunamis and or long waves to Belek region in Antalya and Haydarpassa harbour are also investigated as other case studies in terms of tsunami induced sedimentation and amplification effects under tsunamis. The results are presented with discussions.

Keywords: Wave, Current, Amplification, Sedimentation, Morphology change, Rouse Number, FFT, NAMI DANCE

ÖZ

KAPALI BASENLERDE TSUNAMIYE BAĞLI DALGA VE AKINTI YÜKSELMELERİ VE KUM HAREKETLER

Kian, Rozita

Doktora., İnşaat Mühendisliği Bölümü
Tez Yöneticisi: Prof. Dr. Ahmet Cevdet Yalçın

Kasım 2015, 163 sayfa

Basenlerde dalga ve akıntı yükselmeleri çeşitli parametrelere bağlıdır. Dalga periyodu bunlar arasında önemlilerinden biridir. Basene giren dalga periyodu, basenin rezonans periyodu ile çakışması durumunda beklenmedik basen içinde uzun periyotlu dalga oluşabilir. Kapalı basenlerde tsunamiye bağlı rezonans yükselmeleri akıntı hızlarının artmasına neden olarak hasarın artışına neden olabilir. Bu tür olaylar liman derinliklerinde değişiklikler yaparak limanların düzenli çalışmasını olumsuz etkiler yaratabilirler.

Genel olarak tsunamiler sığ sularda su düzeyi yükselmeleri ve çökmeleri, su çekilmeleri, kuvvetli akıntılar, seyy salınımları, sürüklenme, çarpma ve kaldırma kuvvetleri yaratarak Zemin malzemesinin yer değiştirmesi ile aşınma, oyulma ve birikmelere neden olurlar. Tsunamilerin rusubat taşınması, aşınma ve birikmeye neden olması, basen ve limanlardaki kıyı tesislerinin düzenli çalışmasını da su derinliği değişimleri yaratarak etkiler. Basenlerdeki kum hareketlerinin modları, boyutsuz

Rouse sayısı ile incelenebilir. Kum hareketinin farklı nodları tabanda sürüklenme, askıda yer deęiřtirme ve yıkama biçiminde sınıflandırılabilir. Bu modlar Rouse sayısı kullanılarak tabanda sürüklenme, askıda yer deęiřtirme ve yıkama biçiminde sınıflandırılabilir.

Bu çalışmada NAMI DANCE isimli tsunami sayısal modeli kullanılarak, tsunami parametrelerinin alansal ve zamansal deęiřimleri ve bunların liman hizmetlerinin başarımlarına olumsuz etkilerisü düzeyi ve akıntı yükselmeleri ve kum hareketleri gözetilerek çıkarılmıştır. Uygulama çalışmalarından birinde L-tipi basenlerde gelen dalganın ve basen şeklinin sonuçlara etkileri incelenmiştir. Dięer uygulamalarda Antalya Belek Bölgesi ve Haydarpařa limanının hem kum hareketleri hem de su düzeyi ve akıntı yükselmeleri durumları araştırılmış olup sonuçlar tartılıřılarak sunulmuřtur.

Anahtar Kelimeler: Dalga, Akıntı, Artırma, Birikme, Morfology deęiřme, Rouse sayısı, FFT, NAMI DANCE

“To My Beloved Family”

ACKNOWLEDGEMENTS

I would like to express my sincere appreciation to Prof. Dr. Ahmet Cevdet Yalçın for his endless and very valuable supports, academic supervision, and for his heartfelt efforts to provide opportunities to open up new frontiers in my researches. I would like to thank Prof. Dr. Ayşen Ergin, Dr. Isikhan Güler, Assist. Prof. Dr. Gülizar Özyurt Tarakcioğlu and Dr. Cüneyt Baykal for their hearty supports and great sympathy throughout my thesis, and also for their contributions to my coastal engineering education with their valuable knowledge and experiences.

I would like to acknowledge Dr. Andrey Zaitsev for his valuable collaboration and efforts in the development of numerical code NAMI DANCE in my research.

I would like to thank Dr. Ceren Özer Sözdinler for her valuable helps and Research Assistants Betül Aytöre and Aykut Pamuk for providing data needed for case study.

I dedicate my thanks to the guidance of all referred studies, which throw fresh light on my studies.

My most willingly thanks are to my dear friends and colleagues in METU Ocean Engineering Research Center for their great efforts to amuse and encourage me even at hard times.

Words are inadequate to express my thanksgiving to my beloved family for their everlasting supports, endless love and encouragement.

I gratefully acknowledge TÜBİTAK (The Scientific and Technological Research Council of Turkey) 2215 Program of fellowship for foreign students for providing financial support to my studies as Ph.D. Scholarship.

TABLE OF CONTENTS

ABSTRACT	v
ÖZ	vii
ACKNOWLEDGEMENTS.....	x
TABLE OF CONTENTS	xi
LIST OF FIGURES.....	xiii
LIST OF TABLES	xxi
LIST OF SYMBOLS	xxv
CHAPTERS	
1. INTRODUCTION.....	1
2. LITERATURE SURVEY	3
2.1. Resonance in Enclosed Basins (Ports and Harbors)	3
2.1.1. Amplification of Wave.....	5
2.1.2. Amplification of Current Velocities.....	6
2.2. Harbor Damage.....	8
2.3. Harbor Resonance.....	9
2.3.1. Free Oscillations in Closed Basins.....	18
2.4. Sedimentation.....	21
2.4.1. Rouse Number.....	27
3. METHODOLOGY	33
3.1. Numerical Model (NAMI DANCE).....	34
3.2. Fast Fourier Transform Technique (FFT).....	35

3.3. Verification of the Model.....	35
4. NUMERICAL TESTS FOR SEDIMENTATION AND AMPLIFICATION IN L TYPE BASINS.....	45
4.1. Simulation	46
4.2. Results of Numerical Tests and Comparisons.....	47
5. SEDIMENTATION BY TSUNAMI, CASE STUDY IN ANTALYA	79
5.1. Discussion and Remarks	101
6. SEDIMENTATION AND RESONANCE IN HARBORS; A CASE STUDY IN HAYDARPASA HARBOR	103
6.1. Source input.....	106
6.2. Simulations:.....	108
6.3. Resonance Periods in Haydarpaşa Basin	116
6.4. Long Wave Effects on Haydarpaşa Basin.....	118
6.5. Amplification in Haydarpaşa Harbor.....	121
7. CONCLUSIONS.....	141
Suggestions for Future Studies:	146
REFERENCES	147
APPENDICES	
A. APPLIED EQUATIONS IN THE MODEL.....	157
A.1. Non-Linear Shallow Water Equation (NLSWE).....	157
A.2. Stability of the Model	160
CURRICULUM VITAE	161

LIST OF FIGURES

FIGURES

Figure. 2.1 Surface profiles for the first four seiche modes in closed and open-ended rectangular basins of uniform depth. (Source: Rabinovich, A. B., Seiches and harbor oscillations, 2008).....	13
Figure 2.2. Diagram of provided model by Takahashi et al. (2000)	22
Figure 2.3. An example of the Hjulström-Sundborg Diagram (Weiss 2004).....	26
Figure 2.4. Settling Velocity Vs. Diameter- Settling velocity W_s of a sand grain (diameter d , density 2650 kg/m^3) in water at $20 \text{ }^\circ\text{C}$, computed with the formula of Soulsby (1997)	29
Figure 2.5. Sediment Property vs. Diameter	30
Figure. 3.1. Regular closed square shaped-flat bottom basin with ($d=100\text{m}$)-shore to shore distance ($L=5013\text{m}$). The crest of the initial impulse is parallel to one of the sides. Wave propagation in a) $t=2\text{sec}$, b) $t=4\text{sec}$, c) $t=6\text{sec}$, d) $t=10\text{sec}$, e) $t=24\text{sec}$ and f) $t=60\text{sec}$	42
Figure. 3.2. Regular closed square shaped-flat bottom ($d=500\text{m}$)-shore to shore distance ($L=5013\text{m}$). The crest of the initial impulse is circular at the center of the basin. Wave propagation in a) $t=0\text{sec}$, b) $t=2\text{sec}$, c) $t=30\text{sec}$, d) $t=52\text{sec}$	43
Figure. 4.1. L-type harbor used in simulations. LA is the vertical dimension and LB is the horizontal dimension of the L shaped basin.	46
Figure. 4.2. The bathymetry of L-type basin used in simulations with 10 selected gauge points (red stars).	47
Figure. 4.3. The spatial distribution of maximum water surface elevation (m) computed by the simulation of sinusoidal line crest long wave with 1m wave amplitude with $T=16\text{s}$, $T=46\text{s}$, $T=90\text{s}$, $T=146\text{s}$, $T=328\text{s}$ for $LA/LB=0.8$ in the left column and $LA/LB=1$ in the right column from a to j respectively.....	48

Figure. 4.4. The spatial distribution of maximum current velocity (m/s) computed by the simulation of sinusoidal line crest long wave with 1m wave amplitude with T=16s, T=46s, T=90s, T=146s, T=328s for LA/LB=0.8 in the left column and LA/LB=1 in the right column from a to j respectively.....	50
Figure. 4.5. The spatial distribution of minimum Rouse Number computed by the simulation of sinusoidal line crest long wave with 1m wave amplitude with T=16s, T=46s, T=90s, T=146s, T=328s for LA/LB=0.8 in the left column and LA/LB=1 in the right column from a to j respectively. The maximum velocity vectors are also shown on each case.....	52
Figure. 4.6. The spatial distribution of maximum water elevation for L-type a) with close end boundary, b) with open end boundary, maximum current velocity c) with close end boundary, d) with open end boundary, minimum Rouse Number e) with close end boundary, f) with open end boundary computed by the simulation of sinusoidal line crest long wave with 1m wave amplitude with T328s for LA/LB=1.....	57
Figure. 4.7. The spatial distribution of maximum water elevation for L-type with open (red line) and close (black line) boundary in a) g57, b) g63, c) g33 and d) g42 during 40min simulation of sinusoidal line crest long wave with 1m wave amplitude with T328s for LA/LB=1.....	58
Figure. 4.8. The spatial distribution of maximum current velocity for L-type with open (red line) and close (black line) boundary in a) g57, b) g63, c) g33 and d) g42 during 40min simulation of sinusoidal line crest long wave with 1m wave amplitude with T328s for LA/LB=1.....	59
Figure. 4.9. Time history of water surface elevation a) when LA/LB=1, b) when LA/LB=0.8, time history of current velocity c) when LA/LB = 1 d) when LA/LB=0.8 in gauge 20.....	60
Figure. 4.10. Time history of water surface elevation a) when LA/LB=1, b) when LA/LB=0.8, time history of current velocity c) when LA/LB=1, d) when LA/LB=0.8 in gauge 25.....	61

Figure. 4.11. Time history of water surface elevation a) when LA/LB=1, b) when LA/LB=0.8, time history of current velocity c) when LA/LB=1, d) when LA/LB=0.8 in gauge 33.....	62
Figure. 4.12. Time history of water surface elevation a) when LA/LB=1, b) when LA/LB=0.8, time history of current velocity c) when LA/LB=1, d) when LA/LB=0.8 in gauge 42.....	63
Figure. 4.13. Time history of water surface elevation a) when LA/LB=1, b) when LA/LB=0.8, time history of current velocity c) when LA/LB=1, d) when LA/LB=0.8 in gauge 57.....	64
Figure. 4.14. Time history of water surface elevation a) when LA/LB=1, b) when LA/LB= 0.8, time history of current velocity c) when LA/LB is equal to 1 d) when LA/LB=0.8 in gauge 63.....	65
Figure. 4.15. Time history of water surface elevation a) when LA/LB=1, b) when LA/LB=0.8, time history of current velocity c) when LA/LB=1, d) when LA/LB=0.8 in gauge 72.....	66
Figure. 4.16. Time history of water surface elevation a) when LA/LB=1, b) when LA/LB=0.8, time history of current velocity c) when LA/LB=1, d) when LA/LB=0.8 in gauge 79.....	67
Figure. 4.17. Time history of water surface elevation a) when LA/LB=1, b) when LA/LB=0.8, time history of current velocity c) when LA/LB=1, d) when LA/LB=0.8 in gauge 86.....	68
Figure. 4.18. Time history of water surface elevation a) when LA/LB=1, b) when LA/LB=0.8, time history of current velocity c) when LA/LB=1, d) when LA/LB=0.8 in gauge 91.....	69
Figure 5.1. Tsunami source used in simulations and bathymetry of the area (Pamuk, 2014).....	81
Figure 5.2. The Study Domain.....	81
Figure 5.3. Distribution of the maximum current velocity during the 90 min simulation.....	82
Figure 5.4. Distribution of maximum flow depth during the 90 min simulation.....	83
Figure 5.5. Minimum Rouse Numbers in each grid during the simulation.....	83

Figure 5.6. Instantaneous Rouse Numbers for 55th minute	84
Figure 5.7. Instantaneous Rouse Numbers for 70th minute	85
Figure 5.8. Instantaneous Rouse Numbers for 80th minute	85
Figure. 5.9. The bathymetry and the gauge points used in the simulations in Belek region in Antalya, a) time history of water surface elevation, b) time history of low depth, c) time history of current velocity d) time history of Rouse number during 90min simulation in Gauge A.	89
Figure. 5.10. The bathymetry and the gauge points used in the simulations in Belek region in Antalya, a) time history of water surface elevation, b) time history of low depth, c) time history of current velocity d) time history of Rouse number during 90min simulation in Gauge B.	90
Figure. 5.11. The bathymetry and the gauge points used in the simulations in Belek region in Antalya, a) time history of water surface elevation, b) time history of low depth, c) time history of current velocity d) time history of Rouse number during 90min simulation in Gauge C.	91
Figure. 5.12. The bathymetry and the gauge points used in the simulations in Belek region in Antalya, a) time history of water surface elevation, b) time history of low depth, c) time history of current velocity d) time history of Rouse number during 90min simulation in Gauge D.	92
Figure. 5.13. The bathymetry and the gauge points used in the simulations in Belek region in Antalya, a) time history of water surface elevation, b) time history of low depth, c) time history of current velocity d) time history of Rouse number during 90min simulation in Gauge E.....	93
Figure. 5.14. The bathymetry and the gauge points used in the simulations in Belek region in Antalya, a) time history of water surface elevation, b) time history of low depth, c) time history of current velocity d) time history of Rouse number during 90min simulation in Gauge F.....	94
Figure. 5.15. The bathymetry and the gauge points used in the simulations in Belek region in Antalya, a) time history of water surface elevation, b) time history of low depth, c) time history of current velocity d) time history of Rouse number during 90min simulation in Gauge G.	95

Figure. 5.16. The bathymetry and the gauge points used in the simulations in Belek region in Antalya, a) time history of water surface elevation, b) time history of low depth, c) time history of current velocity d) time history of Rouse number during 90min simulation in Gauge H.	96
Figure. 5.17. The bathymetry and the gauge points used in the simulations in Belek region in Antalya, a) time history of water surface elevation, b) time history of low depth, c) time history of current velocity d) time history of Rouse number during 90min simulation in Gauge I.	97
Figure. 5.18. The bathymetry and the gauge points used in the simulations in Belek region in Antalya, a) time history of water surface elevation, b) time history of low depth, c) time history of current velocity d) time history of Rouse number during 90min simulation in Gauge J.	98
Figure. 5.19. The bathymetry and the gauge points used in the simulations in Belek region in Antalya, a) time history of water surface elevation, b) time history of flow depth, c) time history of current velocity d) time history of Rouse number during 90min simulation in Gauge K.	99
Figure. 5.20. The bathymetry and the gauge points used in the simulations in Belek region in Antalya, a) time history of water surface elevation, b) time history of low depth, c) time history of current velocity d) time history of Rouse number during 90min simulation in Gauge L.	100
Figure. 6.1 Haydarpasa Harbor in Istanbul	105
Figure. 6.2. The location of impulse a) dome shaped source inside the rhombohedral shape basin (R1), b) dome shaped source outside the rhombohedral shape basin (R2), c) sinusoidal line source parallel to the main breakwater (R3), d) sinusoidal line source perpendicular to the main breakwater (R4), at numerical gauge locations G1, G2, G3, G4.	107
Figure. 6.3. Dome shaped wave (5m amplitude) propagation as time history in a) $t = 0$, b) $t = 10s$, c) $t = 30s$, c) $t = 60s$ by the simulation (R1) of dome shaped inside the rhombohedral shape basin.	107

Figure. 6.4. The spatial distribution of maximum water surface elevation, maximum current velocity, and the maximum momentum flux computed by the simulation (R1) of dome shaped source.....	110
Figure. 6.5. The spatial distribution of maximum water surface elevation, maximum current velocity, and the maximum momentum flux computed by the simulation (R2) of dome shaped source.....	111
Figure. 6.6 Line impulse in sinusoidal shape (1m amplitude) with crest line parallel to the main breakwater axis in x direction propagates as time history in a) t = 0, b) t = 10s, c) t = 30s, d) t = 60s, by the simulation (R3).	112
Figure. 6.7. Line impulse in sinusoidal shape (1m amplitude) with crest line perpendicular to the main breakwater axis in x direction propagates as time history in a) t = 0, b) t = 10s, c) t = 30s, d) t = 60s, , by the simulation (R4).	112
Figure 6.8. The spatial distribution of maximum water surface elevation, maximum current velocity, and the maximum momentum flux computed by the simulation (R3) of sinusoidal shaped line source with the crest parallel to the main breakwater.....	113
Figure. 6.9. The spatial distribution of maximum water surface elevation, maximum current velocity, and the maximum momentum flux computed by the simulation (R4) of sinusoidal shaped line source with the crest perpendicular to the main breakwater.....	113
Figure. 6.10. The time histories of water level at numerical gauge locations 1-6 (a-f respectively), computed by the simulations (R1, R2, R3 and R4) for the first 3 minutes of simulation.	114
Figure. 6.11. The time histories of current velocities at numerical gauge locations 1-6 (a-f respectively), computed by the simulations (R1,R2, R3 and R4) for the first 3 minutes of simulation.	115
Figure. 6.12. Long wave with 1m amplitude and 90s period, propagates towards the Haydarpasa Harbor in a) t = 10, b) t = 90s, c) t = 200s.....	120

Figure. 6.13. The spatial distribution of maximum water surface elevation (m) computed by the simulation of sinusoidal line crest long wave with 1m wave amplitude with a) T=67s, c) T=90s, c) T=154s, d) T=200s, e) T=800s and f) T=900s respectively.....	122
Figure. 6.14. The spatial distribution of maximum water surface elevation (m) computed by the simulation of sinusoidal line crest long wave with 2m wave amplitude with a) T=67s, c) T=90s, c) T=154s, d) T=200s, e) T=800s and f) T=900s respectively.....	123
Figure. 6.15. The spatial distribution of maximum current velocity (m/s) computed by the simulation of sinusoidal line crest long wave with 1m wave amplitude with a) T=67s, c) T=90s, c) T=154s, d) T=200s, e) T=800s and f) T=900s respectively.	124
Figure. 6.16. The spatial distribution of maximum current velocity (m/s) computed by the simulation of sinusoidal line crest long wave with 2m wave amplitude with a) T=67s, c) T=90s, c) T=154s, d) T=200s, e) T=800s and f) T=900s respectively.	125
Figure. 6.17. The spatial distribution of minimum Rouse Number computed by the simulation of sinusoidal line crest long wave with 1m wave amplitude with a) T=67s, c) T=90s, c) T=154s, d) T=200s, e) T=800s and f) T=900s respectively. The maximum velocity vectors are also shown on each case.....	126
Figure. 6.18. The spatial distribution of minimum Rouse Number computed by the simulation of sinusoidal line crest long wave with 2m wave amplitude with a) T=67s, c) T=90s, c) T=154s, d) T=200s, e) T=800s and f) T=900s respectively. The maximum velocity vectors are also shown on each case.....	127
Figure. 6.19. Haydarpasa Harbor a) bathymetry and the gauge points used in the simulations, b) Rouse Number, c) time history of water surface elevation d) time history of current velocity in G7.	129
Figure. 6.20. Haydarpasa Harbor a) bathymetry and the gauge points used in the simulations, b) Rouse Number, c) time history of water surface elevation d) time history of current velocity in G6.	130

Figure. 6.21. Haydarpasa Harbor a) bathymetry and the gauge points used in the simulations, b) Rouse Number, c) time history of water surface elevation d) time history of current velocity in G5. 131

Figure. 6.22. Haydarpasa Harbor a) bathymetry and the gauge points used in the simulations, b) Rouse Number, c) time history of water surface elevation d) time history of current velocity in G4. 132

Figure. 6.23. Haydarpasa Harbor a) bathymetry and the gauge points used in the simulations, b) Rouse Number, c) time history of water surface elevation d) time history of current velocity in G3. 133

Figure. 6.24. Haydarpasa Harbor a) bathymetry and the gauge points used in the simulations, b) Rouse Number, c) time history of water surface elevation d) time history of current velocity in G2. 134

Figure. 6.25. Haydarpasa Harbor a) bathymetry and the gauge points used in the simulations, b) Rouse Number, c) time history of water surface elevation d) time history of current velocity in G1. 135

Figure. 6.26. Haydarpasa Harbor a) bathymetry and the gauge points used in the simulations, b) Rouse Number, c) time history of water surface elevation d) time history of current velocity in G8. 136

LIST OF TABLES

TABLES

Table 2.1. Modes of free oscillations in closed basins with simple geometric shape and constant width (in Rabinovich, 2008 from Wilson, 1972)	134
Table 2.02. Modes of free oscillations in semi-closed basins with simple geometric shape (in Rabinovich, 2008, modified from Wilson, 1972).....	15
Table 2.03. Mode of free oscillations in rectangular and circular geometric shape basins with uniform depth (Rabinovich, 2008).....	26
Table 2.4. Typical constants.....	268
Table 2.05. Modes of transport according to the Rouse Number (Yeh, 2008)	268
Table 2.06. Distribution of grain size in Belek (Ergin et al., 2007)	30
Table 3.1. Periods of free oscillations in regular shaped closed square 5013m shore to shore distance basin, flat bottom, $d=100$. The crest of the initial impulse is parallel to one of the basin sides	37
Table 3.03. Periods of free oscillations in regular shaped closed square 5013m shore to shore distance in the basin, flat bottom, $d=500$ m. The crest of the initial impulse is parallel to one of the basin sides.....	39
Table 3.3. Periods of free oscillations in regular shaped closed square 5013m shore to shore distance basin, flat bottom, $d=1000$ m. The crest of the initial impulse is parallel to one of the basin sides	40
Table 3.4. Periods of free oscillations in regular shaped semi-enclosed square 5013m shore to shore distance basin, flat bottom ($d = 500$ m). The imputed wave is time dependent 10s period circular shaped sinusoidal motion in vertical direction at the center of the domain (yalciner et al., 2007) (second column); the initial wave input is in the form of initially static gaussian shape uplift of water surface with 100m diameter (third column).....	40

Table 4.1. Maximum water surface elevation, maximum current velocity and minimum Rouse Number in g20, g25, g33, g42, g57, g63, g72, g79, g86 and g91 in L-type basin in 16sec wave period in columns 4, 5, 6 respectively. Sinusoidal line crest 1m wave amplitude is from the basin entrance (LA/LB=1). X coordinate of the gauge point (second column), Y coordinate of the gauge point (third column). The simulation duration is 40min	71
Table 4.04. Maximum water surface elevation, maximum current velocity and minimum Rouse Number in g20, g25, g33, g42, g57, g63, g72, g79, g86 and g91 in L-type basin in 46sec wave period in columns 4, 5, 6 respectively. Sinusoidal line crest 1m wave amplitude is from the basin entrance (LA/LB=1). X coordinate of the gauge point (second column), Y coordinate of the gauge point (third column). The simulation duration is 40min	72
Table 4.03. Maximum water surface elevation, maximum current velocity and minimum Rouse Number in g20, g25, g33, g42, g57, g63, g72, g79, g86 and g91 in L-type basin in 90sec wave period in columns 4, 5, 6 respectively. Sinusoidal line crest 1m wave amplitude is from the basin entrance (LA/LB=1). X coordinate of the gauge point (second column), Y coordinate of the gauge point (third column). The simulation duration is 40min	73
Table 4.04. Maximum water surface elevation, maximum current velocity and minimum Rouse Number in g20, g25, g33, g42, g57, g63, g72, g79, g86 and g91 in L-type basin in 146sec wave period in columns 4, 5, 6 respectively. Sinusoidal line crest 1m wave amplitude is from the basin entrance (LA/LB=1). X coordinate of the gauge point (second column), Y coordinate of the gauge point (third column). The simulation duration is 40min	74
Table 4.05. Maximum water surface elevation, maximum current velocity and minimum Rouse Number in g20, g25, g33, g42, g57, g63, g72, g79, g86 and g91 in L-type basin in 328sec wave period in columns 4, 5, 6 respectively. Sinusoidal line crest 1m wave amplitude is from the basin entrance (LA/LB=1). X coordinate of the gauge point (second column), Y coordinate of the gauge point (third column). The simulation duration is 40min	265
Table 5.1. Fault parameters of tsunami source (Pamuk, 2014).....	80

Table 6.01. Periods (s) of free oscillations in Haydarpasa Port. Static dome shape wave with 5m amplitude inside the rhombohedral shape basin (first column), Static dome shape wave with 5m amplitude outside the rhombohedral shape basin (second column), Crest line impulses are in parallel (third column) and perpendicular (forth column) directions to the main breakwater with 1m amplitude and 10sec period of sinusoidal wave	117
Table 6.05. Maximum water surface elevation, maximum current velocity and minimum Rouse Number in G7, G6, G5, G4, G3, G2, G1 and G8 in Haydarpasa Harbor in 67sec wave period in columns 4, 5, 6 respectively. Sinusoidal line crest 1m wave amplitude is 1km far from the main breakwater. X coordinate of the gauge point (second column), Y coordinate of the gauge point (third column).	137
Table 6.03. Maximum water surface elevation, maximum current velocity and minimum Rouse Number in G7, G6, G5, G4, G3, G2, G1 and G8 in Haydarpasa Harbor in 90sec wave period in columns 4, 5, 6 respectively. Sinusoidal line crest 1m wave amplitude is 1km far from the main breakwater. X coordinate of the gauge point (second column), Y coordinate of the gauge point (third column).	138
Table 6.04. Maximum water surface elevation, maximum current velocity and minimum Rouse Number in G7, G6, G5, G4, G3, G2, G1 and G8 in Haydarpasa Harbor in 154sec wave period in columns 4, 5, 6 respectively. Sinusoidal line crest 1m wave amplitude is 1km far from the main breakwater. X coordinate of the gauge point (second column), Y coordinate of the gauge point (third column).	138
Table 6.05. Maximum water surface elevation, maximum current velocity and minimum Rouse Number in G7, G6, G5, G4, G3, G2, G1 and G8 in Haydarpasa Harbor in 200sec wave period in columns 4, 5, 6 respectively. Sinusoidal line crest 1m wave amplitude is 1km far from the main breakwater. X coordinate of the gauge point (second column), Y coordinate of the gauge point (third column).	138

Table 6.06. Maximum water surface elevation, maximum current velocity and minimum Rouse Number in G7, G6, G5, G4, G3, G2, G1 and G8 in Haydarpassa Harbor in 800sec wave period in columns 4, 5, 6 respectively. Sinusoidal line crest 1m wave amplitude is 1km far from the main breakwater. X coordinate of the gauge point (second column), Y coordinate of the gauge point (third column)..... 139

Table 6.07. Maximum water surface elevation, maximum current velocity and minimum Rouse Number in G7, G6, G5, G4, G3, G2, G1 and G8 in Haydarpassa Harbor in 900sec wave period in columns 4, 5, 6 respectively. Sinusoidal line crest 1m wave amplitude is 1km far from the main breakwater. X coordinate of the gauge point (second column), Y coordinate of the gauge point..... 139

LIST OF SYMBOLS

A_n	:		Amplitude of the sea level oscillation
B	:		Width of basin
C	:		Concentration at boundary of both layers
CB	:		Mean concentration of bed load layer
CS	:		Mean Concentration of suspended load layer
d	:		Median grain size
D	:		Total water depth ($\eta+h$)
f	:		Darcy friction factor
g	:		Gravitational Acceleration
hB	:		Depth of bed load layer
h	:		Undisturbed water depth
i	:		number of grid node in x direction
j	:		number of grid node in y direction
k	:		number of increment in time
k	:		Bottom friction coefficient
L	:		Length of basin
M	:		Discharge flux in x-direction
N	:		Discharge flux in y-direction
n	:		Manning's coefficient
P	:		Pick-up rate
P	:		Hydrostatic pressure
qB	:		Bed load rate
$R0$:		Rouse number
s	:		Density of sand in

		water
t	:	Time
T	:	Wave period
T_n	:	Period of free surface oscillation
u, v	:	Depth-averaged water particle velocities in the cross-shore x and long-shore y directions, respectively
V_{max}	:	Maximum velocity
u^*	:	Shear velocity
wex	:	Exchange load
ws	:	Settling velocity
ZB	:	Bed level
X_{st}	:	Amplitude of forcing function in the undamped natural frequency
β	:	Ratio of sediment diffusion to momentum diffusion coefficients
ϕ	:	Phase angle
η	:	Water surface elevation
$\eta(x, y, t)$:	Water surface elevation with respect to the undisturbed water level
ζ	:	Damping factor
w_f	:	Circular forcing frequency
ρ	:	Density of sea water
τ_{ij}	:	Shear stress in i direction on the j normal plane
τ_x, τ_y	:	Bottom friction in x and y directions

CHAPTER 1

INTRODUCTION

Complex combination of land, air and water behavior makes the coastal area one of the important parts in the world to pay attention. Since many activities like tourism, industry, agriculture, fisheries take place in coastal area; also energy source, mineral and gas and petroleum sources are directly connected to this area, it is obvious that coastal area should be noticed and invested socially and economically.

Ports, harbors as enclosed basins are the main examples of coastal structures that people need for efficiently using the coastal areas. These coastal structures usually have encounter natural hazards with small or huge damaging scales. Oscillation effects and morphological changes are two of important tasks in the basins under short and long waves attack. Tsunamis as long waves lead to sedimentation as erosion and accretion in the basins which in this study its relation to the current pattern is noticed. Also wave and current amplifications may generally cause problems in ports and harbors especially in shipping and cargo transportation. The wave amplification due to tsunamis has been studied by many researchers but the current amplification has not been paid attention in studies.

In this study, oscillation and sedimentation in harbors as a closed basin are discussed. In Chapter 2, a brief literature survey is given in order to provide background information.

In Chapter 3, the numerical model, NAMI DANCE, used in simulations in order to compute the time history and maximum and/or minimum values of water surface elevation, current velocity, Rouse number, flow depth and momentum flux in determined gauge points or estimated critical points with the governing equations are explained. Then the Fast Fourier Technique, used to obtain the energy spectrum from the time history of water surface elevation, is explained. The resonance periods are determined by using energy spectrum curves, the maximums represent the resonance periods. At the end of this chapter the model verifications performed by re-modeling some of simulations of Yalciner and Pelinovsky (2007) in rectangular basins in order to calculate the basin resonance in enclosed and semi-enclosed basins. Computed results are plotted with different initial parameters to compare and discuss.

The long wave induced oscillations in enclosed basins and their effect as wave and current amplifications in L-type basins are presented in Chapter 4. Then the morphology changes as a result of wave amplification and current pattern are studied according to the Rouse number changes in L-type basins. How the shape and dimension parameters of these basins affect the results are also discussed.

Sediments movement as a morphology change issue is one of the important and challenging topics paid attention a lot in coastal areas. But the sedimentation as a result of tsunami and other long waves has not been noticed that much. Pamuk (2014) studied about sediment movement by using Rouse number as a non-dimensional parameter and considering friction matrix in Antalya, Turkey. In Chapter 5, sedimentation by sedimentation in Antalya region is studied using the minimum and time history of Rouse number during 90 minutes simulation. Unlike Pamuk studies, friction is assumed a fixed and constant value; instead a sediment property matrix is assigned to the grids. The results are presented and discussed.

In Chapter 6, the morphology change, resonance periods, wave and current amplifications discussed throughout the study are applied to a case study in Haydarpaşa Harbor, Turkey and results are presented.

In Chapter 7, conclusions and future recommendations are given.

CHAPTER 2

LITERATURE SURVEY

2.1. Resonance in Enclosed Basins (Ports and Harbors)

Wave amplification inside the basins are related to different parameters. Wave period is one of the important parameters which governs the amplification inside the basins. If the period of incident wave coincides with one of the periods of free oscillations in the basin then resonant oscillation and amplification happens. This phenomenon is very important and causes the unexpected amplifications and hence affects the harbor operations and management (Kian et al., 2015a, b). Proper assessment of the dynamic mooring forces on ships and docks is very important task which should be considered in harbor planning. If the period of the wave in the harbor reaches the natural period of the mooring ships or docks it makes serious problems in loading and unloading in some ports for several days. Uttermost cases lead to very great damages right behind the mooring lines have departed. Therefore, it is necessary to predict the wave amplitude in different locations of a harbor according to the existence wave period. Ippen (1966) found that the resonance in harbors closely affects the maximum wave amplitude in different parts of a harbor. A specific harbor can amplify the wave amplitudes in a determined incident wave period.

The resonant oscillations in harbors have been called as sicche, surging by different investigators. The term harbor oscillations will be used here instead since surge defines a “once only” motion, and seiche refers to the free oscillations of a closed body of water, i.e. lakes. According to Wiegel (1964) the harbor oscillation may be

the oscillation of the harbor at one or more of its harmonic frequencies, or oscillating at the frequency of the long period wave train exciting it. If the vertical motions are due to the tsunami or storm surge, the vertical motions may be magnify.

Oscillations in hydraulic and coastal problems have been studied since early 20th. The oscillation topics in the study field include free and forced oscillations in enclosed or semi-enclosed basins with regular or irregular bathymetries. Lee (1971) developed an exact solution method for rectangular harbor theory applied for regular shape basin, and a numerical approach as an arbitrary harbor theory for arbitrary basins. In order to obtain Navier Stokes solution by considering nonlinear resonance terms Yao (1999) applied a wave theory to determine long-time solutions of nonlinear differential equations. Many old numerical models calculate wave amplitudes of the basins due to certain periods. The critical period as a period of free oscillations is obtained by several simulations applying waves with different periods to create highest amplitude. In this thesis a short cut numerical method is used with only one run according to Yalciner and Penilovsky (2007), Yalciner et al. (1996a, b) which is explained in chapter 3 instead of old and classical methods with several simulations to evaluate modes of free oscillations in irregular basins.

Wemelsfelder (1957) proved that harbor oscillation is connected with natural periods of the harbor. The reflections and interface waves from the edge of harbors can lead to wave height amplifications and also extend the wave activity duration due to tsunamis.

How does an incident single surge affect on harbor oscillations? Some of them certainly must be able to set up oscillations, just as hitting a drum with a stick causes the drum membrane to vibrate. LeMehaute (1960) found that this type of oscillation might be important in a harbor with a wide entrance, but less important for harbors with narrow entrance, because of limited time to increase the energy density in harbor to higher levels.

2.1.1. Amplification of Wave

Amplification of waves lead to harbor damage by direct and/or indirect effects at first, and then resonance in harbors exacerbate the damage. Numerical modeling of tsunamis in harbors are discussed in two categories i) the harbor damage and ii) the harbor resonance. First, an overview of those possibilities are introduced and described. In order to determine the level of tsunami hazard and develop measures to increase resilience, the effects of main tsunami hydrodynamic parameters in shallow zone and at land area investigated. Distribution of resilience against disasters in harbors, water level and current amplifications, and some examples of tsunami induced hazards in harbors from different prefectures during the 2011 Japan event are compiled and presented based on an extensive literature survey.

The main tsunami hydrodynamic parameters are; (i) maximum positive amplitude, (ii) maximum current velocity, (iii) maximum flow depth, (iv) maximums of hydrodynamic forces, (v) maximum of momentum flux, (vi) maximum negative amplitude, (vii) the arrival time of the first wave, (viii) the arrival time of maximum wave, and (ix) the duration of the inundation and withdrawal of tsunami. Since basins' depths are shallow at all long wave conditions, the tsunami surge modeling in a harbor becomes applicable by using the governing equations under long wave conditions. Those are used to compute and evaluate the effects of main tsunami hydrodynamic parameters in shallow zone and at land in order to determine the level of tsunami hazard and develop the measures to increase the level of the resilience of the study area.

After several experiments, LeMehaute (1955) concluded that the in rectangular harbors, the wave amplitude can reach 5 times the incident wave amplitude if the entrance size is reduced enough. If the entrance is too small the friction will act as a significant factor and the amplitude of the oscillations decrease. Nakano (1963) investigated about the effect of diffraction energy in the bays opening to the oceans surrounded by cliffs. He assumed the rectangular bay with flat bathymetry without friction. He found that the smaller the width of the bay with respect to its length, the

energy density of the standing wave will be larger. It was also found that the shallower the bays, the energy density will increase more.

2.1.2. Amplification of Current Velocities

Currents with enough strength propagating the entrance of a narrow bay may cause oscillations (Nakano and Abe, 1958). Therefore, the mechanism is formed by unsymmetrical Von Karman vortices. These kind of oscillations may be the same in some basins, but infrequent in others. Also they may be abundant or uncommon in a certain year. The natural periods of the ports and harbors in relation to the exciting energy determines the amount of occurrences (Wiegel, 1964). The significant periods of harbor oscillation pertain to the basin size. These ranges are about 2-3 minutes at Terminal Island in California, 7-11 minutes in some harbors of Netherlands, 1-20 minutes at Haydarpasa harbor in Turkey, 15-40 minutes in several Japanese ports. Wemelsfelder (1957) proved that harbor oscillation is relating to the natural periods of the harbors by measuring the periods of oscillations in four harbors as a function of tide stage. The periods are function of tide phase; hence, the harbor oscillates at one of the natural periods.

It is easier to observe the vertical motions when they are larger. Small vertical motions are accompanied by proportionally larger horizontal motion of the water. As the period of horizontal water motion matches with the natural period of surge, sway, or way of moored ships, larger resonance phenomenon happens which leads to a significant motion of the moored ships. For example, damages in Los Angeles Harbor happened while the ships are moving longitudinally during the surging and transversely during the swaying due to the large horizontal displacements (Knapp and Vanoni, 1945; Carr, 1953).

Strong tidal currents can also cause oscillations in the harbors (Rabinovich, 2008). For example, in Naruto Strait as a narrow channel between the Shikoku and Awaji islands in Japan where Pacific Ocean and the Inland Sea connects, there are such types of oscillations. The tidal currents move huge volume of water between Pacific

and the Inland Sea twice per day with the velocity of 13-15 km/h. As the velocity increases up to 20 km/h significant seiche oscillations with 2.5 min wave period created because of the flood tidal currents (Honda et al., 1908). These oscillations take place right after low tide and cease near high tide

Nakano (1933) illustrated the phenomenon considering the heavy currents passing the bay or harbor mouth as a source of seiche. This is similar to the manner of air jet passing the mouth of a pipe and generates standing oscillation. *Nakano and Abe* (1959) showed that flows with high speed which exceeds specific critical number can make von Karman vortexes on both sides of the channel. Therefore, if the fundamental periods match the typical vortex periods (Eq.2.1), oscillations in bays and harbors are probable to occur.

$$T_{\text{vor}} = l/u, \quad (2.1)$$

where l is the distance between vortexes, and u is the vortex's speed ($u = 0.4V$ to $0.6V$, where V , is the speed of the tidal currents). For the case of Naruto tidal currents, the experiments showed that values of T_{vor} match with the occurred seiche period of 2.5 min.

Tsunami induced currents inside the ports and harbors are very complicated. Eddies and gyres can be generated where the currents are concentrated. Therefore, scouring occurs around breakwaters and then sediments deposit at the basins in ports and harbors (PIANC, 2014).

To conclude, resonance inside harbors due to tsunami waves can exacerbate the damages by amplifying the water level changes, currents, and momentum fluxes. An example of assessing possible amplifications due to resonance is presented in thesis for consideration of future work. The presented study has been focused on the distribution of water level and current velocity amplifications due to the long wave motion inside Haydarpassa harbor. The fully reflective boundaries inside the ports (such as Haydarpassa port) should be considered as the critical locations under the

extreme wave conditions. Current amplification should be studied more specific and separately since it is more dependent on the shape of basin.

2.2. Harbor Damage

Local topography and the height of the incident tsunami affect the damages in respective coastal areas. Since port areas are vulnerable to tsunamis, damages are inevitable even if there is small level of inundation. The propagation of tsunamis near shore are due to wave transportation, which are wave shoaling, refraction, diffraction, also depending on the topography of submarine can become a bore and/or breaking tsunami. It is noticeable that generally because of deep entrance of the ports, tsunamis act neither like bore nor breaking tsunami. Since tsunami is not like a bore in protected ports, a tsunami wave usually does not overtop the breakwater and the tsunami induced water elevation is lower than the height of breakwater crest. This leads tsunami to enter the port via openings in the breakwaters. Therefore, people have time to run away from the area because the water elevation in the port is relatively slow. Of course in the case of large tsunamis, a huge mass of water will overtop the breakwaters and enter into the port. As a result, there will be an inundation and lack of time to evacuate the region. During a tsunami, seawater will intrude into the land if the height of water level is higher than the ground level of the port. In order to facilitate cargo-handling, the land area of ports are usually flat, therefore, there is venture of flooding while after the inundation occurs. In shallower water depths, tsunami affects more severely. But for the facilities in Japanese ports, no significant damages recorded. However, it is important to consider the damages because of rapid currents due to tsunamis. Generally, main port damages can be summarized as damages from: parting of vessel moorings, manoeuvring movements which are not controlled or transporting unmoored vessels due to tsunami currents, vessels when they are lifted out of water, sediment scouring or deposition due to a tsunami (PIANC, 2009).

According to the PIANC (2014), the Great East Japan Tsunami induced destructive damages in the Iwate, Miyagi and Fukushima ports. Since several tsunamis took place in that area, many simulations and measurements have been used to mitigate the disasters by using past data. Actually, the Great East Japan Tsunami was greater than these previous events and demolished the breakwaters and seawalls and then led to wide region of inundation.

From geotechnical point of view, the possible damage induced by earthquakes and resultant tsunamis, the damages can take place in the ports are summarised as:

- High-response acceleration, vast deformation, liquefaction.
- Tsunami wave force, flow hydraulic force (drag force), buoyancy, and impact of floating objects.

The reasons of damage mechanism have not yet been illuminated. However, numerical simulations of the propagation and inundation of the Great East Japan tsunami showed a decrease in the impact of the tsunami by the offshore breakwater in the Port of Kamaishi (PIANC, 2014). The mechanism of the failures of the tsunami defences was studied using experiments and it was concluded that the overtopping current was the main cause of the failure. Furthermore, the results show that the tsunami defence structures decrease the tsunami severity during overtopping if they are not broken or overturned.

2.3. Harbor Resonance

Problems of harbor resonance can be caused by swell waves and tsunamis as regular waves and also by storm wind waves as irregular waves. Indeed for most of the ports regular waves cause less frequency of occurrence, therefore, most of practical studies should be performed considering incoming irregular short waves. However, resonance problem in harbors are usually studied with regular waves in practice (Girolamo, 1995).

The harbor oscillations are generated in two steps: first, generation of long waves in open seas, second, forcing of the harbor oscillations when the long waves intrude in the basin (Rabinovich, 2008). If the frequency of coming tsunami waves match with the resonance frequencies of the harbor then serious devastation occurs. Large tsunami amplification of Port Alberni in Alaska tsunami 1964 because of resonance is a good example (Murty, 1977; Henry and Murty, 1995). One of the other problems due to tsunami in harbors is oscillations.

In Honda et al., 1908, an observation in 1992 by Omori has been mentioned. In that observation distinguished periods of tsunami waves are found similar to the ones caused by usual long waves in the same basin. Omori explained that part of the sea oscillates such as fluid pendulum with its own frequency and the coming tsunami waves make similar seiches as the ones made by other types of external forces. Many articles reporting similar observations in several different regions of the world ocean affirmed this consequence (Miller, 1972; Van Dorn, 1984; Djumagaliev et al., 1993; Rabinovich, 1997; Rabinovich et al., 2006; Rabinovich and Thomson, 2007).

One of the indispensable natures of harbor oscillations is that even small vertical motions can go along with large horizontal water motions (harbor currents); more resonance take place whenever the period of these motions coincides with the natural period of swing or yaw of a moored ship (Wiegel, 1964; Sawaragi and Kubo, 1982). Strong currents due to the seiches have taken more concern than sea level variations due to seiche in port and harbor functions. It is noticeable that the maximum current velocities take place at the nodal lines. Hence, the nodal lines should be considered unsafe regions comparing to other locations (Rabinovich, 2008).

Strong currents in the harbor induced by 2006 and 2011 tsunamis in Crescent City caused whole damages which were not because of land flooding because there was not any in 2006 tsunami and very small flooding in 2011 tsunami. These events prove the importance of strong tsunami currents and their impacts in ports and harbors (Amanda et al., 2014). Tsunami currents are usually predicted by numerical models, and only few of studies have been validated by real measurements. In tsunami of Hokkaido in 1993, the peak current velocity was estimated 10-18 m/s

(Shimamoto et al., 1995; Tsutsumi et al., 2000). The peak tsunami current speeds of the 2010 Chile and 2011 Japan tsunamis in the coast and entrance to Humboldt Bay shows that currents are focused at the harbor entrance. Thus, any floating or submerged thing near the harbor or port corner has considerable potential to experience strong and rotational currents (Amanda et al., 2014). It is possible to compute the current speed by tsunami deposit analysis. However, this method leads to obtain peak currents not the time history of the flow.

Wave radiation via the semienclosed basins such as harbors, bays and inlets is one of the important factors in decaying energy. Making the harbor entrance narrower, the amplification of arriving wave occurs. Therefore, dams, dikes and other harbor protecting structures could tighten the entrance width, then intensive resonance oscillations take place inside the harbor named, this phenomenon is named harbor paradox (Miles and Munk, 1961). Considerable long waves are generated by enhancing the atmospheric disturbances above the ocean during the resonance action. The resonant effects may noticeably amplify ocean waves entering the coast. Ocean waves cannot generate enough energy to affect open coasts by resonance amplification; they can cause hazardous oscillations when they intrude the harbors as semi-closed basins. Besides, large oscillations inside a harbor can be formed if the external forcing has sufficient energy. Tsunami waves which are generated in open oceans can be serious enough even in absence of additional effects. Therefore, upon measurements tsunami waves generated in 2004 Sumatra earthquake had wave height around 1-2 m, but atmospherically generated tsunami can lead hazardous rates just in the case of some external resonance. This is the main difference of tsunami waves and meteotsunamis (Titov et al., 2005).

Another noticeable fact is that the difference in spectral peaks among several tide gauges records is declarative of effect of local topography. For instance, in the Pacific coast of Vancouver Island, the most significant peaks in the tsunami spectra were for Winter Harbor and Tofino Harbor. Actually, the period of observed tsunami waves are principally relevant with the resonant properties of the local topography rather than characteristics of the source. Hence, different earthquakes generate

similar tsunami spectra in the same region (Honda et al., 1908; Miller, 1972; Rabinovich, 1997). The resonant properties of each area are the same forever; although large seismic sources produce low frequency modes and vice versa (Rabinovich, 2008).

Theoretical solution for the problems of basin oscillations in closed basins is based on solution of Helmholtz equation and different numerical algorithms can be used to solve it. According to Yalciner et al. (2007) there are two procedures to calculate the frequencies of free oscillations: First; using continuous force function to agitate the basin with only one frequency and then repeat the task with other frequencies. Second; using a single force function with a certain frequency and then analysis the spectrum of water surface fluctuations along time. In this thesis, the second method is applied by inputting a single wave with a certain short period. Then time history of water surface fluctuations are stored in gauge locations. Using Fast Fourier Transformation (FFT) technique, frequency spectrum of saved time histories should be determined. The peaks in spectrum curves show the frequency of free oscillations. We investigate the propagation and amplification of long waves using numerical model (NAMI DANCE which solves nonlinear form of shallow water equations and it is applied to several tsunami events worldwide (Zaytsev et al., 2008; Ozer et al., 2008; 2011a; 2011b; Yalciner et al., 2010; 2014). The code computes the sea state according to the user defined time steps, time histories water surface fluctuations and velocities at selected locations (Kian et al., 2014a, b). It is noticeable that the shape or amplitude of the inputted initial impulse does not affect the frequency of free oscillation. The method can compute the periods larger than the period of initial impulse. In order to catch the water surface fluctuations properly for spectrum analysis, the time step must be small and simulation duration must be reasonably long.

The model is tested and verified using enclosed and semi enclosed square basins (Kian et al, 2015a) in chapter 3. When basin is rectangular and enclosed with constant water depth, then the periods of free surface oscillations (T_n) can be calculated according to Eq. 2.2

$$T = \frac{2}{\sqrt{gd}} \left[\left(\frac{n}{L} \right)^2 + \left(\frac{m}{B} \right)^2 \right]^{(-1/2)} \quad n = 0, 1, 2, 3, \dots$$

$$m = 0, 1, 2, 3, \dots \quad (2.2)$$

Where L is the length and B is the width of the basin, d is the water depth, and n, m are integer numbers represent each mode (Raichlen, 1966). If one of the boundaries is open (in semi-enclosed basins) the period is calculated according to Eq. 2.3.

$$T = \frac{1}{n} \frac{4L}{\sqrt{gd}} \quad n = 0, 1, 2, 3, \dots \quad (2.3)$$

Eq. 2.3 shows that the longer the basin length (L) or the shallower the basin depth (d), the longer the oscillation period. According to Korrgen (1995) the wavelength of (n = 1) mode is twice the length of the basin and the wavelength of other modes equal to one half, one third, one fourth and so on, of the wavelength of the fundamental mode (Figure 2.1). Maximum currents take place at the nodal lines, but the minimum currents take place at the antinodes. Water motions at the oscillation nodes are horizontal, and at the antinodes they are vertical (Rabinovich, 2008).

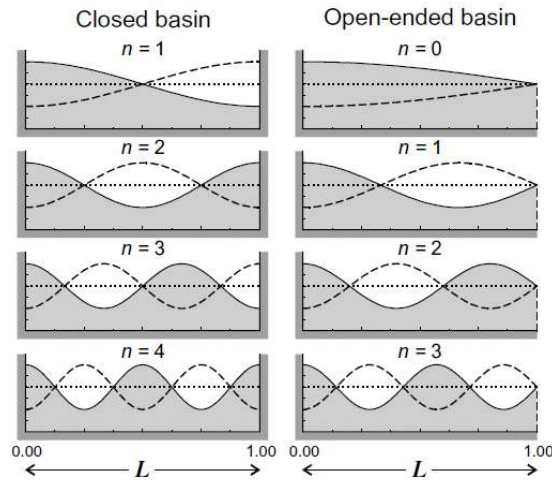


Figure. 2.1 Surface profiles for the first four seiche modes in closed and open-ended rectangular basins of uniform depth. (Source: Rabinovich, A. B., Seiches and harbor oscillations, 2008)

Wilson (1972) showed that it is possible to find analytical solutions for many basins with several simple geometry and non-uniform bathymetries (Table 2.1 and Table 2.2). These results are also applicable as a proper estimation for irregular shapes of harbors and lakes. Table 2.1 represents a summary for the modes of free oscillations in closed basins of simple geometric shape and constant width and Table 2.2 shows the modes of free oscillations in semi-closed basins of simple geometric shape. Finally, Table 2.3 represents mode of free oscillations in rectangular and circular geometric shape basins with uniform depth (Rabinovich, 2008).

Table 2.1. Modes of free oscillations in closed basins with simple geometric shape and constant width (in Rabinovich, 2008 from Wilson, 1972).

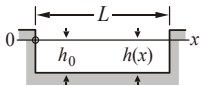
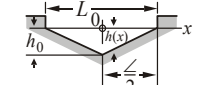
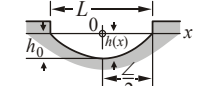
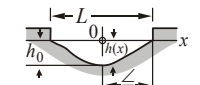
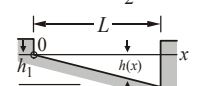
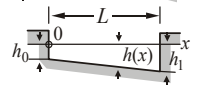
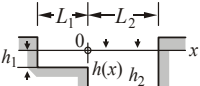
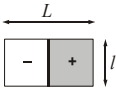
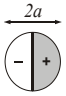

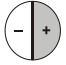

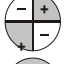
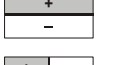
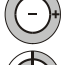

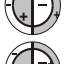




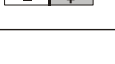

Basin type		Profile equation	Periods of free oscillation					
Description	Dimensions		Fundamental T_1	Mode ratios T_n/T_1 , values for n				
				1	2	3	4	
Rectangular		$h(x) = h_0$	$2L/(gh_0)^{1/2}$	1.000	0.500	0.333	0.250	
Triangular (isosceles)		$h(x) = h_0(1 - 2x/L)$	$1.305 [2L/(gh_0)^{1/2}]$	1.000	0.628	0.436	0.343	
Parabolic		$h(x) = h_0(1 - 4x^2/L^2)$	$1.110 [2L/(gh_0)^{1/2}]$	1.000	0.577	0.408	0.316	
Quartic		$h(x) = h_0(1 - 4x^2/L^2)^2$	$1.242 [2L/(gh_0)^{1/2}]$	1.000	0.686	0.500	0.388	
Triangular (right-angled)		$h(x) = h_1 x/L$	$1.640 [2L/(gh_1)^{1/2}]$	1.000	0.546	0.377	0.288	
Trapezoidal		$h(x) = h_0 + mx$ $m = (h_1 - h_0)/L$		1.000	0.546	0.377	0.288	
Coupled, rectangular		$h(x) = h_1(x < 0)$ $h(x) = h_2(x > 0)$	$L_1/L_2 = 1/2$	$4 L_2/(gh_2)^{1/2}$	1.000	0.500	0.250	0.125
		$h_1/h_2 = 1/4$	$L_1/L_2 = 1/3$	$3.13 L_2/(gh_2)^{1/2}$	1.000	0.559	0.344	0.217
			$L_1/L_2 = 1/4$	$2.73 L_2/(gh_2)^{1/2}$	1.000	0.579	0.367	0.252
			$L_1/L_2 = 1/8$	$2.31 L_2/(gh_2)^{1/2}$	1.000	0.525	0.371	0.279

Table 2.2. Modes of free oscillations in semi-closed basins with simple geometric shape (in Rabinovich, 2008, modified from Wilson, 1972).

Basin type		Profile equation	Fundamental T_0	Periods of free oscillation			
Description	Dimensions			Mode ratios T_s/T_1 [$n = (s + 1)/2$]			
				$n = 0$	1	2	3
Rectangular	Rectangular	$h(x) = h_1$	$2.000 [2L/(gh_1)]^{1/2}$	1.000	0.333	0.200	0.143
Rectangular	Triangular	$h(x) = h_1 x/L$	$2.618 [2L/(gh_1)]^{1/2}$	1.000	0.435	0.278	0.203
Rectangular	Semiparabolic	$h(x) = h_1(1 - x^2/L^2)$	$2.220 [2L/(gh_1)]^{1/2}$	1.000	0.409	0.259	0.189
Triangular	Rectangular	$b(x) = b_1 x/L$ $h(x) = h_1$	$1.308 [2L/(gh_1)]^{1/2}$	1.000	0.435	0.278	0.230
Triangular	Triangular	$b(x) = b_1 x/L$ $h(x) = h_1 x/L$	$1.653 [2L/(gh_1)]^{1/2}$	1.000	0.541	0.374	0.283
Semielliptic	Semiparaboloidal	$b_1/L = 2$ $= 4/3$ $= 1$ $= 2/3$	$2.220 [2L/(gh_1)]^{1/2}$	1.000	0.707 0.554 0.447 0.317	0.578 0.493 0.468 0.455	0.378 0.323 0.264 0.185
Semicircular	Semiparaboloidal	$h(x) = h_1(1 - r^2/L^2)$	$2.220 [2L/(gh_1)]^{1/2}$	1.000	0.707	0.578	0.500

Table 2.3. Mode of free oscillations in rectangular and circular geometric shape basins with uniform depth (Rabinovich, 2008)

Rectangular basin ($l = 0.5L$)				Circular basin						
Mode numbers		Mode forms	Relative period	Mode numbers		Mode forms	Circular nodal lines		Normalized frequency	Relative period
m	n		T_{mn}/T_{10}	s	m		r_1	r_2	$\omega a/c$	T_{sm}/T_{10}
1	0		1.000	1	0		-	-	1.841	1.000
2	0		0.500	2	0		-	-	3.054	0.603
0	1		0.500	0	1		0.628	-	3.832	0.480
1	1		0.447	1	1		0.719	-	5.331	0.345
2	1		0.354	2	1		0.766	-	6.706	0.275
0	2		0.250	0	2		0.343	0.787	7.016	0.262
1	2		0.243	1	2		0.449	0.820	8.536	0.216

The main concern in the port operations and ships in harbors are because of the seiche induced huge currents than only the seiche variations of sea level. Since the maximum horizontal current velocities take place in the nodal points, the regions close to the nodes are unsafe. Sorensen and Thompson (2002) calculated the maximum velocities V_{\max} as Eq. 2.4.

$$V_{\max} = A_n \sqrt{\frac{g}{H}} \quad (2.4)$$

where A_n is the amplitude of the sea level oscillation for the nth mode.

The mechanism of resonance phenomenon can be described by differential equation in Eq.2.5 to understand the amplification (Ippen, 1966).

$$M\ddot{x} + C\dot{x} + Kx = F_0 \cos(\omega_f t) \quad (2.5)$$

where M = mass of the oscillating body

C = a linear damping coefficient

K = a spring constant

w_f = a circular forcing frequency

In case of steady-state solution:

$$x = X \cos(w_f t - \phi)$$

Where ϕ = a phase angle between the input and the output functions, X, as the maximum displacement and the phase angle ϕ can be presented nondimensionally as

$$\frac{X}{X_{st}} = \frac{1}{\{[1 - (w_f/w_n)^2]^2 + (2\zeta w_f/w_n)^2\}^{1/2}} \quad (2.6)$$

$$\tan \phi = \frac{2\zeta w_f/w_n}{1 - (w_f/w_n)^2} \quad (2.7)$$

Where $X_{st} = F_0/K$

$$w_n = (K/M)^{1/2}$$

$$\zeta = C/2Mw_n$$

X_{st} is the amplification of the forcing function in the approximately undamped natural frequency of the system. The friction is negligible. Resonance frequency diverges from the frequency w_n while the damping factor ζ increases. If the frequencies are much greater than the resonant frequency the maximum displacement of the mass approaches zero. In the case of zero damping, Eq. (2.7) leads to infinite resonance amplitude. Therefore, the linear approach used would become unrealistic. Number of coordinates required to describe the system of motion, represents the freedom degree of a system. In elastic body cases, there are infinite coordinates for the particles movement; hence, there are infinite modes of oscillations with natural frequencies.

2.3.1. Free Oscillations in Closed Basins

In closed basin with rectangular shape of width b , length a , and depth h , periods of the free oscillation could be calculated a function of its dimensions:

The governing Laplace equation throughout the fluid (Eq.2.8.) and boundary conditions in Eq. 2.9 to Eq.2.12:

$$\nabla^2 \phi = 0 \quad \text{where} \quad \nabla^2 = \frac{\partial^2}{\partial x^2} + \frac{\partial^2}{\partial y^2} + \frac{\partial^2}{\partial z^2} \quad (2.8)$$

$$\eta = \frac{1}{g} \frac{\partial \phi}{\partial t} \quad \text{at} \quad z=0 \quad (2.9)$$

$$w = -\frac{\partial \phi}{\partial t} = 0 \quad \text{at} \quad z=-h \quad (2.10)$$

$$u = -\frac{\partial \phi}{\partial x} = 0 \quad \text{at} \quad x=0, a \quad \text{for} \quad 0 \leq y \leq b \quad (2.11)$$

$$v = -\frac{\partial \phi}{\partial y} = 0 \quad \text{at} \quad y=0, b \quad \text{for} \quad 0 \leq x \leq a \quad (2.12)$$

The solution is according to Eq. 2.13

$$\phi = X(x) + Y(y) + Z(z)T(t) \quad (2.13)$$

Substituting Eq.(2.13) into Eq.(2.8);

$$Z'' - k^2 Z = 0 \quad (2.14)$$

$$X'' - \epsilon^2 X = 0 \quad (2.15)$$

$$Y'' - (k^2 - \epsilon^2) Y = 0 \quad (2.16)$$

where k^2 , ϵ^2 are constants. k is wave number and it is constant.

$$\sigma^2 = gk \tanh kh \quad (2.17)$$

Eqs. 2.14 to 2.16 have the following solution:

$$Z = A e^{kz} + B e^{-kz} \quad (2.18)$$

$$X = C \cos \epsilon x + D \sin \epsilon x \quad (2.19)$$

$$Y = E \cos(\sqrt{k^2 - \epsilon^2} y) + F \sin(\sqrt{k^2 - \epsilon^2} y) \quad (2.20)$$

The solution is assumed to be periodic in time, so the time variation of the velocity;

$$T(t) = G \sin \sigma t \quad (2.21)$$

Substituting the boundary conditions [Eqs. (2.10, 2.11, 2.12)] to the velocity potential achieved by substituting Eqs. (2.18, 2.19, 2.20) into Eq. (2.13), the following expression results:

$$\phi = \frac{Hg}{2\sigma} \frac{\cosh k(h+z)}{\cosh kh} \cos \frac{n\pi x}{a} \cos \frac{m\pi y}{b} \sin \sigma t \quad (2.22)$$

where $\frac{H}{2}$ = maximum amplitude of standing wave system

m, n= integers (0, 1, 2, 3,...)

Due to the shallow water condition Eq. (2.22) becomes to:

$$\phi = \frac{Hg}{2\sigma} \cos \frac{n\pi x}{a} \cos \frac{m\pi y}{b} \sin \sigma t \quad (2.23)$$

Substituting Eq.(2.23) into the surface boundary condition, Eq.(2.9) leads to achieve the variation of amplitude within the basin in Eq.(2.24):

$$\eta = \frac{H}{2} \cos \frac{n\pi x}{a} \cos \frac{m\pi y}{b} \cos \sigma t \quad (2.24)$$

Equating the storage change with flow change in the two directions in the control volume:

$$h \left(\frac{\partial u}{\partial x} + \frac{\partial v}{\partial y} \right) + \frac{\partial \eta}{\partial t} = 0 \quad (2.25)$$

Substituting Eqs. (2.23) and (2.24), i.e., $u = -\frac{\partial \phi}{\partial x}$ and $v = -\frac{\partial \phi}{\partial y}$, into Eq.(2.25), one obtains

$$h \frac{Hg}{2\sigma} \left[\left(\frac{n\pi}{a} \right)^2 + \left(\frac{m\pi}{b} \right)^2 \right] - \frac{H}{2} \sigma = 0$$

which reduces to

$$T = \frac{2}{\sqrt{gh}} \left[\left(\frac{n}{a} \right)^2 + \left(\frac{m}{b} \right)^2 \right]^{-1/2} \quad (2.26)$$

Due to the importance of the longitudinal oscillations in long and narrow basins Eq. (2.26) becomes to Merian's formula in Eq. (2.27):

$$T = \frac{2a}{n\sqrt{gh}} \quad (2.27)$$

When the water level rises and falls uniformly in the basin, it is called pumping mode which occurs in $n=0$. Number of nodes in the x direction is presented by n, and m refers to the number of nodes in the y direction.

The maximum and minimum oscillations would occur at $x=0$ and $x=a$.

Proudman (1953) applied the Eq. (2.27) in some lakes as examples.

- Loch Earn lake in Scotland: $a=6.22\text{mi}$, $h=200\text{ft}$.

For $n=1$,

$$T = \frac{2(32800)}{[(322)(200)]^{1/2}} = 810\text{sec} = 13.5\text{min}$$

The observed period is 14.5 min.

- Lake George, New South Wales: $a=18.66\text{mi}$, $h=18\text{ft}$.

The period calculated is 129min, observed period was 131min.

In these two examples for the basins which their shape is approximately rectangular, the measured oscillation period is close to the calculated value of oscillation period.

Although Haydarpaşa harbor is not a rectangular basin, but this method is also applied to Haydarpaşa harbor and it ends with the results in similar pattern. The mean length and the mean depth of the Haydarpaşa harbor can be calculated as:

$a=1.25\text{mi}$, $h=65\text{ft}$.

For $n=1$,

$$T = \frac{2(6600)}{[(322)(65)]^{1/2}} = 288\text{sec} = 45\text{min}$$

The numerical model used in chapter 6 shows $T=1100$ sec for the first mode and 200sec for the second mode. But this method in Eq. (2.26) shows 280sec for the first mode and 140 sec for the second mode. The differences are due to the basin shape which cannot be exactly approximated as a rectangular basin.

2.4. Sedimentation

Sediment transport in the near shore regions is critical under not only extreme but also common marine events. Ground material under the tsunami motion move and scour/erosion/deposition patterns are observed in the region. According to numerous studies, the initiation of the motion of the ground material is related to the physical characteristics of the grain material and the strength of the flow.

Tsunamis carry vast amount of materials and cause morphological erosion and/or deposition on coastal utilities and harbors. In addition tsunamis cause functional failure in the ports (Takahashi et al., 2000) due to depth change and damage. One of the most important factors on morphological changes at coastal plains is the return flows of invaded sea water. The morphology of river mouths is vulnerable subject to direct impact by tsunamis. An example is the river mouth of Pakarange Cape which was exposed to morphological changes because of strong return flows during 2004 Indian Ocean tsunami (Feldens et al., 2009). Keshtpour (2014) studied about beach erosion to the Indian River and carried out numerical simulations for sediment transport downdrift of tidal inlets in 2015.

Generally, the studies available in literature can be divided into two categories. One of them is related to observations after tsunami surveys. In these studies, authors give general description of damages and morphological changes induced by the tsunami events. Other category is related to the equations to model the morphological

changes. Morphological changes cause return flow and river beds increase this effect, therefore, river mouths need special care (Pamuk, 2014).

In recent century, tsunami induced sediment transport has and related model has been investigated vastly. Takahashi et al. (2000) provided a model to simulate erosion, deposition and sediment motions. This model used to model 1960 Chilean Tsunami in Kesennuma Bay. Diagram of provided model is in Figure 2.2. ρ_s is density of sediment particles, C is concentration at boundary of both layers, \bar{C}_B is mean concentration of bed load layer, \bar{C}_S is mean concentration of suspended load layer, q_B is bed load rate, M is flow flux, λ is porosity, h_S and h_B are depth of suspended load layer and bed load layer, respectively, and Z_B is bed level. Due to the balance between rising and settling load, an exchange load is satisfied.

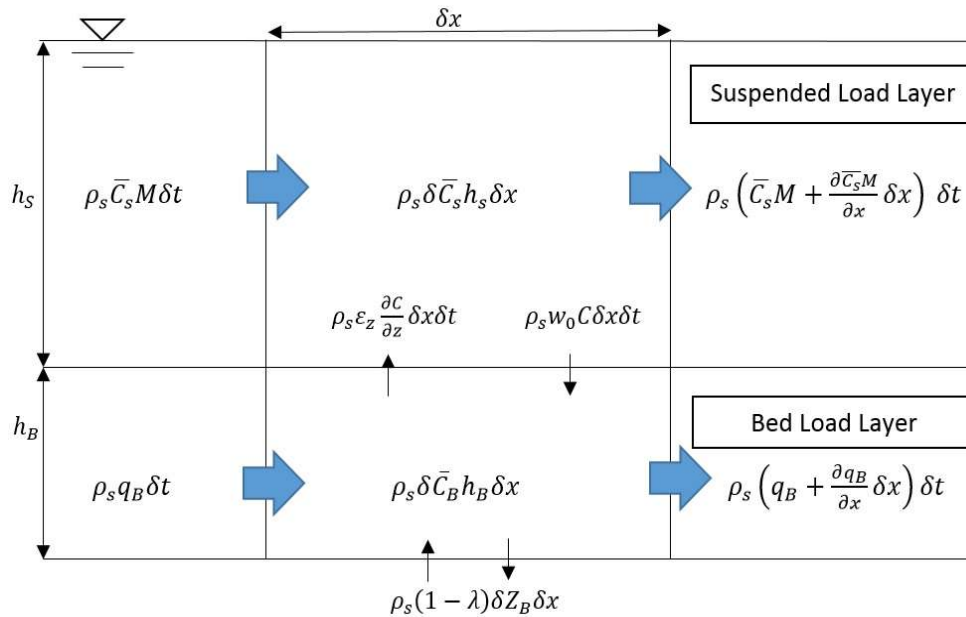


Figure 2.2. Diagram of provided model by Takahashi et al. (2000)

The governing equations (Eq.2.28, Eq.2.29) are determined according to diagram Fig (2.2). h is water depth and w_{ex} is the exchange load.

$$\frac{\partial Z_B}{\partial t} + \frac{1}{1-\lambda} \left(\frac{\partial q_B}{\partial x} + w_{ex} \right) = 0 \quad (2.28)$$

$$\frac{\partial \bar{C}_s M}{\partial x} - w_{ex} + \frac{\partial \bar{C}_s h}{\partial t} = 0 \quad (2.29)$$

According to hydraulic experiment results:

$$\phi_B = 21 \tau_*^{3/2} \quad (2.30)$$

$$\psi_{rise} = 0.012 \tau_*^2 \quad (2.31)$$

where ϕ_B is non-dimensional bed load transport rate, τ_* is Shields parameter and ψ_{rise} is non-dimensional rise rate.

Yoshii et al. (2010) also studied about the modeling of tsunami induced morphological changes. They developed Takahashi et al. (2000) studies to consider the sand grain size. They proposed the pick-up rate as in Eq. (2.32);

$$\frac{P}{\sqrt{sgd} \left(\frac{sgd^3}{v^2} \right)^{0.2}} = 0.15 \left\{ \left(\frac{w_s}{\sqrt{sgd}} \right)^{0.8} (\tau_* - \tau_{*cr}) \right\}^2 \quad (2.32)$$

where P is the pick-up rate, v is the kinematic viscosity, g is gravitational acceleration, s is density of sand inside water, d is grain size and w_s is settling velocity of sand. In case grain size is assumed equal to 0.2 mm Eq.(2.32) be decreased to Eq. (2.33)

$$\frac{P}{\sqrt{sgd}} = 0.015 (\tau_* - \tau_{*cr}) \quad (2.33)$$

The coefficient in Eq.(2.33) is 0.015, but it is equal to 0.012 in Eq. (2.31). Yoshii et al. (2010) formula in Eq.(2.32) is applicable to produce pick-up rates results more accurate than Takahashi et al. (2000).

“Inverse” and “forward” problems have been paid attention due to their importance (Pritchard and Dickinson, 2008). Inverse problem is reconstructing hydrodynamics of a tsunami from the deposits and the forward problem is to predict the sediment transport of a possible future tsunami from the simulation. According to the authors experience, critical Shields parameter is very small than Shields parameter for

tsunami case. Hence, Pamuk (2014) assumed the critical Shields parameter equal to zero.

Sakakiyama et al. (2011) using laboratory experiments investigated the topography change under tsunami attack inside harbors. They concluded that, deposition occurs if there is vortexes in the center of harbors. According to their experiments, Rouse number is more reliable than Shields number as it is close to the site measurements.

Tanaka et al. (2012) investigated the morphology changes due to 2011 Great East Japan Earthquake and Tsunami in Miyagi Prefecture region in Japan. Pamuk, (2014) studied about the tsunami induced morphological changes using aerial photographs taken before and after the hazard. The existing condition in Natori River is similar to the study area of Belek in Pamuk, (2014). There is a lagoon behind a sandy beach. Therefore, similar logic covers the problem and results could be compared. In Natori River, tsunami height reached around 14 m and caused flooding and destruction. There was severe erosion and breaching. The eroded materials were deposited in land and sea by incident wave and return flow respectively. Shoreline changed and huge erosion took place in the river bed.

Similar studies exist for 2004 Indian Ocean Tsunami. Feldens et al. (2009) significantly studied about offshore effects of the morphological changes in Pakarang Cape, Thailand. Strong return flows caused huge morphological changes in river mouths. There was even boulder transport due to tsunami effects.

In the PIANC report (The World Association for Waterborne Transport Infrastructure) mentioned that; scours occur at tips of breakwaters where currents are concentrated and eddies are generated. Hence, scours are generally generated due to the concentration of flows and eddy around structures.

Li et al. (2012) have investigated the tsunami induced coastal changes in Painan, West Sumatra, Indonesia. The study concentrates on sediment movement and morphological changes. High sediment transport and severe scour took placed in the

area. It is noticeable that the average speed of wave front value is calculated around 2 m/sec and flow velocities approached about 5 m/sec. In these velocity values severe erosions and scouring are inevitable which in tsunami cases take less than 1hr to happen.

Li et al. (2012) studied the morphological changes in Lhok Nga, west Banda Aceh, during 2004 Indian Ocean Tsunami. They observed that topography plays a significant role on the characteristics and spatial distribution of tsunami deposits. Also, availability of sand and sediment supply is an important factor in thickness of tsunami deposits.

Sugawara et al. (2014a) have summarized the available numerical models for tsunami induced sediment transport which are categorized to the sediment transport generally into bed load, suspended load and exchange load. They also have listed the necessary issues develop the tsunami sediment models (Sugawara et al., 2014b) ; (1) the applicability of sediment pick-up rate formulations, (2) Manning's roughness and bottom friction coefficients, (3) change of flow characteristics with the intrusion of sediment into flow, (4) turbulence effects, (5) 3D sediment transport formulations for complex topographies, (6) usage of mixed grain-sizes, (7) lateral variation of flow, (8) pore water pressure gradient and exfiltration/infiltration of water.

Hjulström-Sundborg diagram (Figure 2.3) is also one of the methods to assess the sediment transport (Weiss, 2004). This diagram is applied to see if a river will erode, transport or deposit the bed material or not using thresholds.

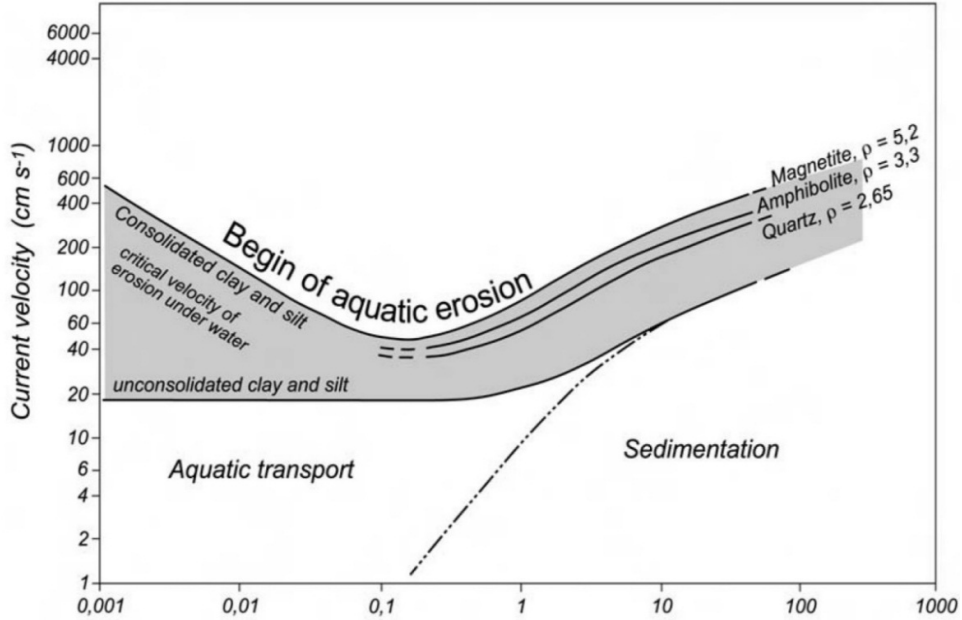


Figure 2.3. An example of the Hjulström-Sundborg Diagram (Weiss 2004)

Another method has been presented by Yeh and Li (2008) for tsunami scour and sedimentation. Shear stress can be represented by a dimensionless number, which is the Shields parameter. It is the ratio of shear stress to buoyant sediment weight. Shields parameter can be calculated as

$$\tau_* = \frac{\tau_0}{\rho g d(s-1)} = \frac{f u^2}{8 g d(s-1)} \quad (2.34)$$

where τ_0 is bed shear stress, ρ is density of water, f is the Darcy friction factor and u is the flow velocity. Darcy friction factor f is in the range of $f=0,006 \sim 0,039$. Yeh and Li (2008) have assumed the f as 0.01 for the tsunami condition.

Pamuk (2014) studied the sediment movement via categorizing the movement modes; bed load rate, suspended load rate and exchange load rate.

2.4.1. Rouse Number

Yeh and Li (2008) have proposed a dimensionless number, which is Rouse number, to classify the modes of sediment transport. Pamuk, (2014), also applied Rouse number in order to assess the morphological changes due to tsunami hazard. Rouse number is the ratio of particle settling velocity to shear velocity. It can be calculated as

$$R_0 = \frac{w_s}{\beta \kappa u_*} \quad (2.35)$$

where u_* is shear velocity β is the ratio of sediment diffusion to momentum diffusion coefficients which is approximately equal to 1. The von Karman constant is κ and equal to 0.4. Settling velocity w_s can be calculated as:

$$w_s = \frac{8v}{d} \left(\sqrt{1 + \frac{(s-1)gd^3}{72v^2}} - 1 \right) \quad (2.36)$$

Where u_* is the shear velocity and can be written according to Eq. (2.37)

$$u_* = u \sqrt{\frac{f}{8}} \quad (2.37)$$

It is also possible to write R_0 as Eq.2.38;

$$R_0 = \frac{S_p}{u} \quad (2.38)$$

where S_p is sediment property matrix and equal to;

$$S_p = \frac{\frac{8v}{d} \left(\sqrt{1 + \frac{(s-1)gd^3}{72v^2}} - 1 \right)}{\beta \kappa \sqrt{\frac{f}{8}}} \quad (2.39)$$

Some constants required for settling velocity and shear velocity calculations. These constants are kinematic viscosity and sea water density, gravitational acceleration and sediment density (Table 2.4).

Table 2.4. Typical constants

v , Kinematic Viscosity	$1.0 \times 10^{-6} \text{ m}^2/\text{s}$
g , Gravitational Acceleration	9.81 m/s^2
ρ , Density of Water	1025 kg/m^3
ρ_s , Density of Sediment Particles	2650 kg/m^3

Modes of sediment transport can be determined according to the Rouse number values. Sediment transport modes are in the form of bed load, suspended load and wash load (Table 2.5). Rouse number value that is greater than 2.5 leads to little or no suspension of sediment mode. However, a value less than 0.8 leads to wash load which is fully supported by the flow. Hence, whenever Rouse number increases chance of sediment transport in suspension mode decreases. Furthermore, sediment transport can increase as Rouse number decreases.

Table 2.5. Modes of transport according to the Rouse Number (Yeh, 2008)

Mode of Transport	Rouse Number
Initiation of Motion (Deposition)	$R_0 > 7$
Bed Load	$2.5 < R_0 < 7.5$
Suspended Load: (50% Suspended)	$1.2 < R_0 < 2.5$
Suspended Load: (100% Suspended)	$0.8 < R_0 < 1.2$
Wash Load	$R_0 < 0.8$

Soulsby (1997) computed the change of settling velocity vs. grain diameter when the grain density is 2650 kg/m^3 and water temperature is $20 \text{ }^\circ\text{C}$ (Figure 2.4).

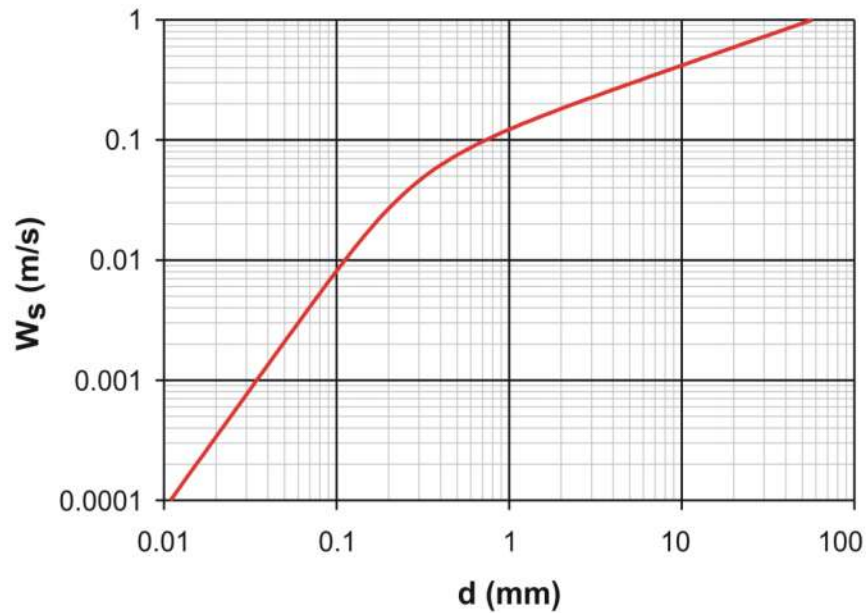


Figure 2.4. Settling Velocity Vs. Diameter- Settling velocity W_s of a sand grain (diameter d , density 2650 kg/m^3) in water at 20°C , computed with the formula of Soulsby (1997)

Figure 2.5 represents the change of sediment property matrix vs. grain diameter. It is clear that the larger Rouse number, the value of sediment property matrix increases. Large Rouse number value indicates slower sediment motion and less severe erosion or deposition. On the other hand, lower Rouse numbers lead to more severe erosion in the topography.

Settling velocity is the highest velocity obtained by an object as it falls through air. It occurs once the sum of the buoyancy and drag force (F_d) equals the downward force of gravity (F_g) acting on the object. The object has zero acceleration due to the net force acting on the object is zero

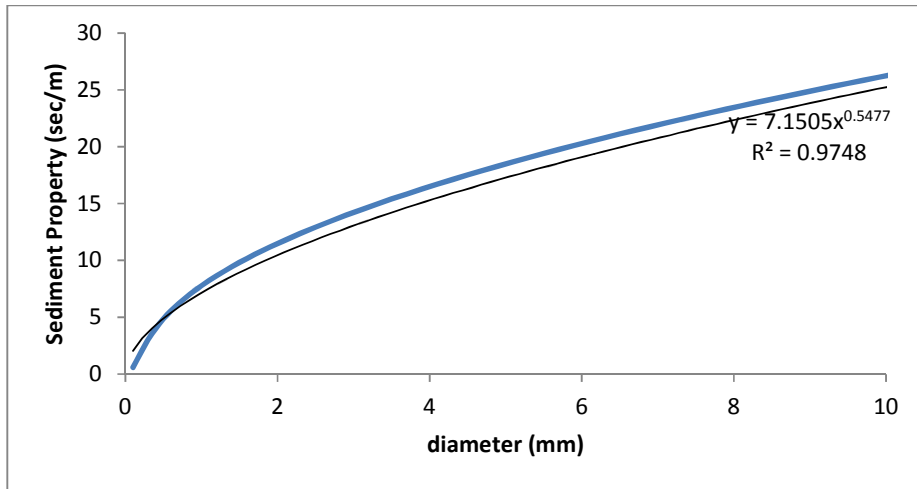


Figure 2.5. Sediment Property vs. Diameter

Settling velocity should be determined in order to obtain the Rouse number. Therefore, settling velocity, grain size distribution of sediment should be determined. Ergin et al. (2007) have studied and determined the grain size distribution of sediment in Southern Turkey (Table 2.6).

Table 2.6. Distribution of grain size in Belek (Ergin et al., 2007)

Beach Name	Belek
Pebble (> 4 mm)	1.3
Granule (4.0-2.0 mm)	0.4
Very Coarse Sand (2.0-1.0 mm)	0.4
Coarse Sand (1.0-0.5 mm)	5.8
Medium Sand (0.5-0.25 mm)	70.7
Fine Sand (0.25-0.125 mm)	20.6
Very Fine Sand (0.125-0.0625 mm)	0.8
Silt + Clay (<0.0625 mm)	0.1
Mean Grain Size (ϕ)	1.67
Mean Grain Size (mm)	0.31

Pamuk (2014), assumed uniform medium sand assumed throughout the whole study domain. He applied 0.31 mm of mean grain size for the entire domain (Eqs 3.11). But actually, the study area should be examined entirely for soil characteristics. Hence, in this study at each grid point the settling velocity has been computed accurately and for the forests and roads regions, instead of using 0.31 mm grain size, different grain sizes has been assigned according to the Table 2.6. Pamuk (2014) applied a friction matrix by assigning values for each grid point but in this study the constant value of 0.015 is used for the entire domain.

Pamuk (2014) obtained the settling velocity according to Yeh and Li (2008) as Eq.(2.40) for the entire domain;

$$w_s = \frac{8v}{d} \left(\sqrt{1 + \frac{(s-1)gd^3}{72v^2}} - 1 \right) = 0.0446 \text{ m/s} \quad (2.40)$$

Then he calculated the Rouse number at each grid point according to the Eq.(2.41).

$$R_0 = \frac{w_s}{\beta \kappa u_*} = \frac{0.043036}{1 * 0.4 * u_* \sqrt{\frac{0.01}{8}}} = \frac{315.09}{u} \quad (2.41)$$

According to the literature review, it is obvious that tsunami flow can cause significant morphological changes in the coastal zones (i.e. sediment transport, erosion, deposition, breaching, scour, etc.). Tsunami effect on the morphological changes is still a developing field of study. Transport due to tsunamis has been investigated mostly since 2000s. In order to method verifications, it is very important to gather bathymetry and topography data before and after the hazard. Tsunami induced sedimentation studies have not been verified with real time field measurement during tsunamis; therefore, the experimental studies are generally according to the laboratory data or analogy of rivers (Li et al., 2011).

As mentioned before, numerical models are vastly applied to study the morphology changes and sedimentations. There are still more investigations are necessary to improve numerical models in flow-bed-structure interactions (Sumer, 2014). The

interactions between sea bed and structures are; sediment transport, scour and erosion processes, coastal hydrodynamics, liquefaction, shear failure and failure of structures.

CHAPTER 3

METHODOLOGY

Generally tsunamis in shallow water zone lead to sea water level rise and fall, strong currents, forces (drag, impact, uplift, etc.), drawdown, scour, and morphological changes (erosion, deposition), debris and debris flow, dynamic water pressure, resonant oscillations and seiches (Yalciner et al., 2014). The aim of this chapter is to present the numerical modeling tool (NAMI DANCE) used in simulations to compute the spatial and temporal changes of main tsunami parameters and their adverse effects on harbor performance. This is identified by analyzing the critical tsunami parameters (water elevation, flow depth, current speed, and momentum fluxes) in the port. On this purpose, some of simulations of Yalciner and Pelinovsky (2007) in rectangular basins are re-modeled in order to verify the numerical model NAMI DANCE in enclosed and semi-enclosed basins. Computed results are plotted with different initial parameters and they are compared and discussed. In the applications, L-Type basins (Kakinuma et al., 2009), Belek region in Antalya province and Haydarpasa port in Istanbul are selected as case studies. Tsunami motions are investigated by focusing on the effect of tsunami parameters on specific points of the harbor or coastal area in the following chapters. The morphological changes and the amplifications are also investigated in the case studies.

3.1. Numerical Model (NAMI DANCE)

Impulsive disturbances at the sea bed or along coastlines can expose tsunamis. In the beginning, the governing equations for tsunamis are according to the linear long wave theory. There are many numerical models used to simulate tsunami propagations, among them COMCOT (Liu et al, 1994; 1998), TUNAMI-N2 (Imamura, 1996) and MOST (Titov and Synolakis, 1998) are mostly used which are two dimensional and solve Non-Linear Shallow Water Equations (NSWE) with finite difference method (Synolakis and Bernard, 2006).

NAMI DANCE, tsunami numerical modeling, is based on the solution of nonlinear form of the long wave equations with respect to related initial and boundary conditions (NAMI DANCE, 2010). It is in C++ language and staggered leap frog scheme numerical solution procedure and prepared as a user-friendly code for tsunami simulation and visualization. It is possible to do simulations in single or nested domains with Cartesian or spherical coordinates and choose the desired equation (linear or non-linear) to solve. The source can be added to the model as an initial static wave or dynamic source with time history of water surface fluctuation. In general, due to the smaller computing duration, the explicit numerical solution of Nonlinear Shallow Water (NSW) is preferred to use instead of implicit methods. Also the errors in results are acceptable. NAMI DANCE has been developed in collaboration with Ocean Engineering Research Center, Middle East Technical University, Turkey and Institute of Applied Physics, Russian Academy of Science, and Special Research Bureau for Automation of Marine Researches, Far Eastern Branch of Russian Academy of Sciences, Russia by Profs. Zaytsev, Chernov, Yalciner, Pelinovsky and Kurkin using the identical computational procedures of TUNAMI N2. These codes are verified in Benchmark problems and applied for several tsunami simulations (Yalciner et. al. 1995, 2002, 2007, 2010; Zahibo et. al. 2003 a,b; Ozer, 2012, Kian et al., 2015 a,b; Velioglu et al., 2015).

The governing equations of NAMI DANCE are the nonlinear form of shallow water equations and hence, the vertical motion of water particles does not have any role in

the hydrostatic pressure. Further information the numerical model is available in Appendix A, NAMI DANCE manual (NAMI DANCE, 2010) and Ozer (2012).

3.2. Fast Fourier Transform Technique (FFT)

Time history of water surface elevation via modeling the long wave propagation with NAMI DANCE is applied to achieve the resonance periods inside the basins. This is performed by applying a Fast Fourier Technique (FFT) on the time history of water surface elevations in selected gauge points in the modeling domain. Hence, the energy spectrum curves are obtained and the resonance periods are determined by the maximum points of the energy spectrum curves as the results of FFT analysis.

Fast Fourier transform (FFT) is an algorithm that computes the discrete Fourier transform (DFT) of a sequence, or its inverse. Fourier analysis is applied convert a signal from its original domain which is usually time or space, to a frequency domain and vice versa. Fast Fourier transforms are mostly applied in engineering and mathematics problems. The basic and original ideas were popularized in 1965, but some algorithms had been derived since 1805 (Heideman et al. 1984). Strang (1994) described the FFT as "the most important numerical algorithm of our lifetime" and it was published in Top 10 Algorithms of 1900s by the IEEE journal Computing in Science & Engineering (Dongarra, 2000).

3.3. Verification of the Model

In order to verify the method and ensure that the method clearly computes the periods of resonance oscillations properly, it is applied to the regular shaped flatbed basins. Some of the simulations used in Yalciner et al (2007) are selected to re-model and compare the results. The dimensions of the selected regular shaped basins are: the square shaped basin with constant depth of 100m, and length (shore to shore distance) of 5013m, second case with the depth of 500m and third case with the depth of 1000m in Table 3.1 to Table 3.3 respectively. The second case is simulated for both closed

flat basin (Table 3.2) and semi-enclosed flat basin (Table 3.4). Input waves used in the models are dynamic initial impulse with sinusoidal shaped single wave parallel to one of the sides with 1m amplitude. The Gaussian shaped (Kian et al., 2014a) wave with 10s period is also used as an initial impulse. The grid size is selected as 20m in simulations and also time step is selected as 0.005s which must be sufficiently small to obtain high resolution spectral curve. The length of the record should also be sufficiently long to catch the long period waves. The time histories of the water surface fluctuations at all numerical gauge points are saved. FFT technique is applied to obtain energy spectrum of the time series at each numerical gauge. The peaks of energy spectrum curves finally indicate the periods of free oscillations. Those obtained from numerical study (NAMI DANCE) are compared with the theoretical values as used in Yalciner et al., (2007). The results are summarized in Table 3.1 to Table 3.4.

The comparison of the results for square shaped flat (5013m wide and 100m deep) basin and (5013m wide and 500m deep) and (5013m wide and 1000m deep) basins are presented in Table 3.1, Table 3.2 and Table 3.3, respectively. The initial impulses are time dependent sinusoidal shaped waves having 10s period with the crest line parallel to horizontal or vertical boundaries of the basin.

The comparison of the results for square shaped semi enclosed flat (5013m wide and 500m deep) basin is presented in Table 3.4. The Table shows the results given in Yalciner et al., (2007) where the time dependent 10s period circular shaped sinusoidal motion in vertical direction is inputted at the center of the domain for comparison of the results of this study. In present study the initial wave input is in the form of Gaussian shape with 100m diameter uplift of initially static water surface. It is seen from the Table that the theoretical and numerical results are in fairly well agreement. It can be concluded that the method calculate the periods of free oscillations in the basins in the accuracy of less than 6%. The method can also be applied to calculate the periods of free oscillations in irregular shaped basins (Kian et al., 2015a).

Figure 3.1 shows the crest line wave propagation in regular closed square shaped-flat bottom with 100m depth which the shore to shore distance is $L=5013\text{m}$. The crest of

the initial impulse is parallel to one of the sides in 2sec, t=4sec, 6sec, 10sec, 24sec and 60sec. Figure 3.2 represents the circular wave in regular closed square shaped with flat bottom and 500m depth which shore to shore distance is L=5013m. Wave propagation is shown in t=0se, 2sec, 30sec and t=52sec.

Table 3.1. Periods of free oscillations in regular shaped closed square 5013m shore to shore distance basin, flat bottom, d=100. The crest of the initial impulse is parallel to one of the basin sides.

$\phi d=100$ m	T(s)		
<i>Mode no.</i>	<i>Theoretical</i>	<i>Yalciner et al (2007)</i>	<i>NAMI DANCE</i>
1	320.13	312.08	324.25
2	160.06	157.92	163.84
3	106.71	106.56	109.22
4	80.03	78.49	79.01
5	64.03	63.32	65.54
6	53.35	53.07	54.26
7	45.73	45.63	46.81
8	40.02	39.60	40.96
9	35.57	35.33	35.92
10	32.01	31.89	32.77
11	29.10	28.81	28.03
12	26.68	26.48	27.31
13	24.63	23.45	24.74
14	22.87	22.80	23.41

Table 3.1. continued

15	21.34	21.31	20.48
16	20.01	19.89	20.66
17	18.83	18.75	18.20
18	17.78	17.74	17.30
19	16.85	16.83	16.38
20	16.01	16.00	16.22
21	15.24	15.26	14.89
22	14.55	14.52	14.25
23	13.92	13.96	13.65
24	13.34	13.33	13.11
25	12.81	12.71	12.79
26	12.31	12.33	12.14
27	11.86	11.88	11.80
28	11.43	11.47	11.30
29	11.04	11.08	11.10
30	10.67	10.68	10.57
31	10.33	10.28	10.24
32	10.00	10.30	10.08

Table 3.2. Periods of free oscillations in regular shaped closed square 5013m shore to shore distance in the basin, flat bottom, d=500m. The crest of the initial impulse is parallel to one of the basin sides.

d=500 m	T(s)		
<i>Mode no.</i>	<i>Theoretical</i>	<i>Yalciner et al (2007)</i>	<i>NAMI DANCE</i>
1	143.16	140.94	146.84
2	71.58	70.09	72.14
3	47.72	46.98	54.61
4	35.79	35.33	40.96
5	28.63	28.31	27.31
6	23.86	23.62	23.41
7	20.45	20.26	20.48
8	17.9	17.83	18.2
9	15.91	15.85	15.6
10	14.32	14.26	14.25
11	13.01	12.94	13.11
12	11.93	11.88	11.7
13	11.01	10.97	10.92
14	10.23	10.18	10.24

Table 3.3. Periods of free oscillations in regular shaped closed square 5013m shore to shore distance basin, flat bottom, d=1000m. The crest of the initial impulse is parallel to one of the basin sides.

d=1000m	T(s)		
Mode no.	Theoretical	Yalciner et al (2007)	NAMI DANCE
1	101.23	100.05	106.22
2	50.62	49.84	54.61
3	33.74	33.52	32.77
4	25.31	25.06	23.41
5	20.25	20.26	20.48
6	16.87	16.83	16.38
7	14.46	14.39	14.25
8	12.65	12.62	12.6
9	11.25	11.19	11.3
10	10.12	10.09	10.05

Table 3.4. Periods of free oscillations in regular shaped semi-enclosed square 5013m shore to shore distance basin, flat bottom (d = 500m). The impuited wave is time dependent 10s period circular shaped sinusoidal motion in vertical direction at the center of the domain (yalciner et al., 2007) (second column); the initial wave input is in the form of initially static gaussian shape uplift of water surface with 100m diameter (third column).

d=500 m	T(s)		
Mode no.	Theoretical	Yalciner et al (2007)	NAMI DANCE
1	285.45	293.44	301.21
2	143.16	145.64	153.84
3	95.15	102.12	105.92
4	71.58	72.55	65.53

Table 3.4. continued

5	57.09	57.99	46.81
6	35.79	36.48	36.41
7	31.72	32.39	32.77
8	28.63	29.13	29.79
9	25.95	25.51,24.36	25.21
10	23.86	22.68,23	23.44
11	21.96	21.39	21.84
12	20.45	20.85	20.48
13	19.03	20.00,18.5	19.27
14	17.9	18.22,17.9	18.2
15	16.79	17.76,17.02	17.25
16	15.91	16.08,15.57	15.6
17	15.02	15.37,15.14	14.89
18	14.32	14.77,14.60,14.42	14.25
19	13.59	14.26,14.05	14.25
20	13.01	13.74,13.51,13.33	13.11
21	12.41	13.08,12.81,12.68	12.14
22	11.93	12.36,12.17,11.91	11.7
23	11.42	11.77,11.60,11.44	11.3
24	11.01	11.25,11.10,10.98	10.92
25	10.57	10.86,10.71,10.6	10.57
26	10.23	10.49,10.38,10.25	10.24

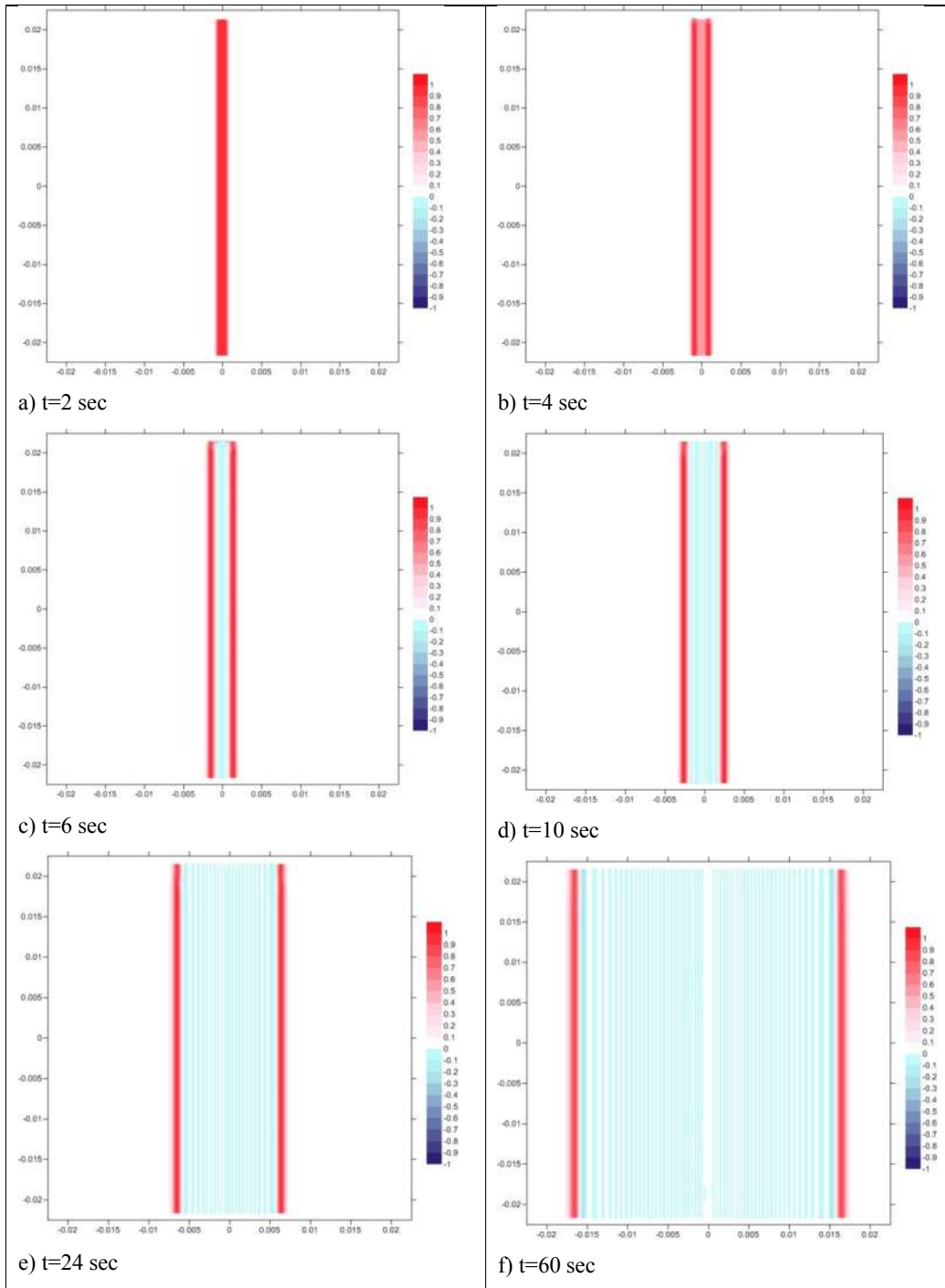


Figure. 3.1. Regular closed square shaped-flat bottom basin with ($d=100\text{m}$)-shore to shore distance ($L=5013\text{m}$). The crest of the initial impulse is parallel to one of the sides. Wave propagation in a) $t=2\text{sec}$, b) $t=4\text{sec}$, c) $t=6\text{sec}$, d) $t=10\text{sec}$, e) $t=24\text{sec}$ and f) $t=60\text{sec}$.

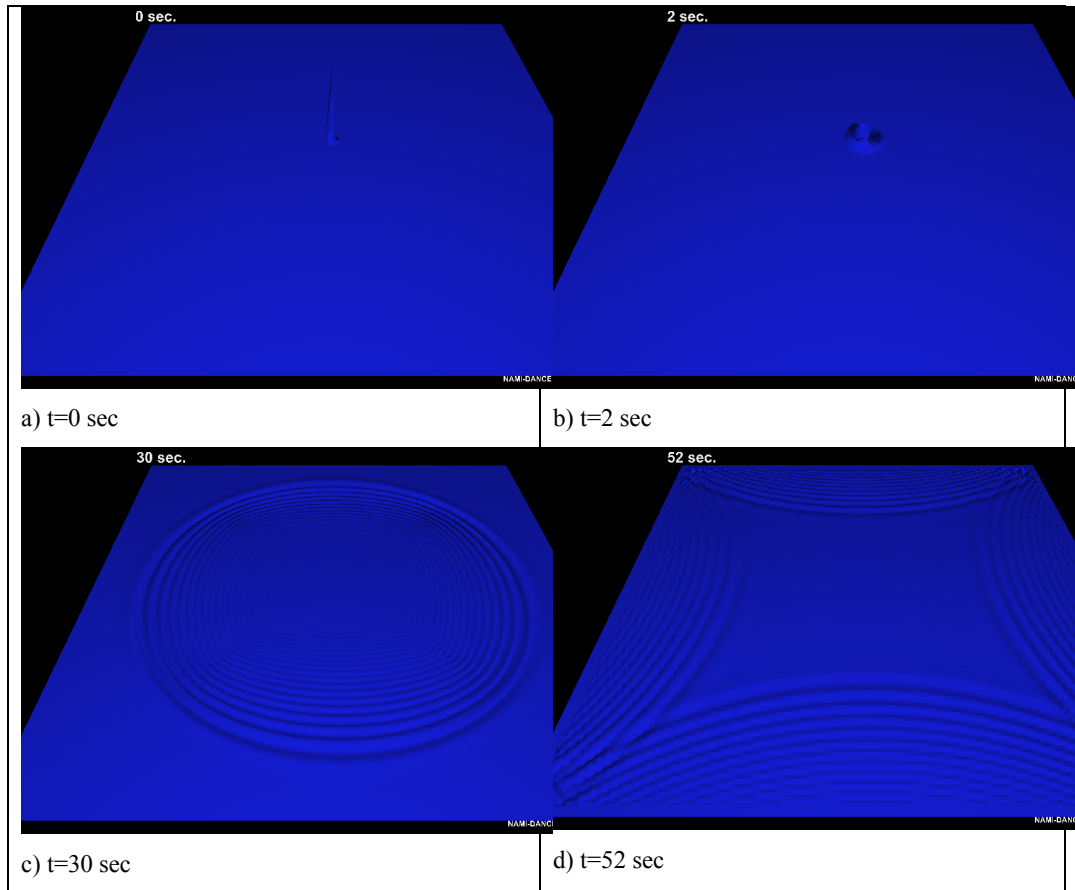


Figure. 3.2. Regular closed square shaped-flat bottom ($d=500\text{m}$)-shore to shore distance ($L=5013\text{m}$). The crest of the initial impulse is circular at the center of the basin. Wave propagation in a) $t=0\text{sec}$, b) $t=2\text{sec}$, c) $t=30\text{sec}$, d) $t=52\text{sec}$.

CHAPTER 4

NUMERICAL TESTS FOR SEDIMENTATION AND AMPLIFICATION IN L TYPE BASINS

Ocean waves cannot generate enough energy to affect open coasts by resonance amplification. But they can cause hazardous oscillations when they enter the enclosed or semi-enclosed basins and harbors. Wave radiation via the semi-enclosed basins is an important factor in decaying energy. On the other hand, making the harbor entrance narrower, the amplification of arriving wave occurs. Therefore, dams, dikes, and other harbor protecting structures could tighten the entrance width, and then intensive resonance oscillations take place inside the harbor, this phenomenon is harbor paradox. Hence, both harbor resonance period and harbour damage parameters could be related by harbor structures design which determines the harbour geometry. In chapter 3 the rectangular shaped basins are investigated by following the method given in Yalciner and Pelinovsky (2007). The resonance periods in different type and sizes of wave input are obtained. While applying the method given in Yalciner and Pelinovsky (2007), the focusing and amplification of the wave, the consequent sediment movement are also investigated and the results are given in the following sections:

4.1. Simulation

The Numerical model, NAMI DANCE, is used to study oscillations and amplification of waves and currents, also sediment motions in a harbor of L shape with a flat bathymetry. Kakinuma et al. (2009) simulated the several regular shaped basins to determine the first and second modes of free oscillations. In this study some of the tests for L type basin are performed, then verification of the models by comparing the results has been satisfied for wave amplification of first two modes. Then several simulations were performed to investigate the current amplification and sediment movement in L-type basins. Figure 4.1 shows the bathymetry used in numerical model tests.

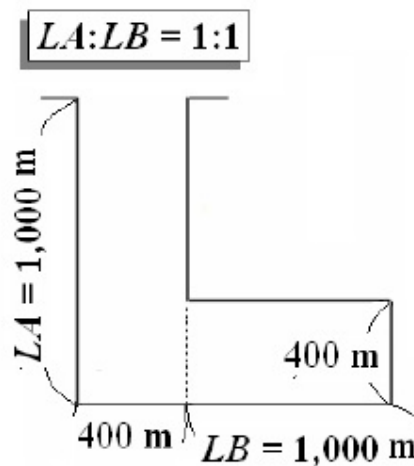


Figure. 4.1. L-type harbor used in simulations. LA is the vertical dimension and LB is the horizontal dimension of the L shaped basin.

In half of the simulations LA is used as 1000m and LB is used as 1000 m and in another half LB is used as 800m (placing the input source at 200m from the border). The bending side is used as 400m in all simulations. The bathymetry is flat and the water depth is 20 m. The input wave is in the form of several sinusoidal waves with 1m and 2m amplitudes with several periods (16 sec, 46 sec, 90 sec, 146 sec and 328) among those 328 sec, 146 sec, 90 sec are the second and fourth and the seventh modes of free oscillations in the basin respectively.

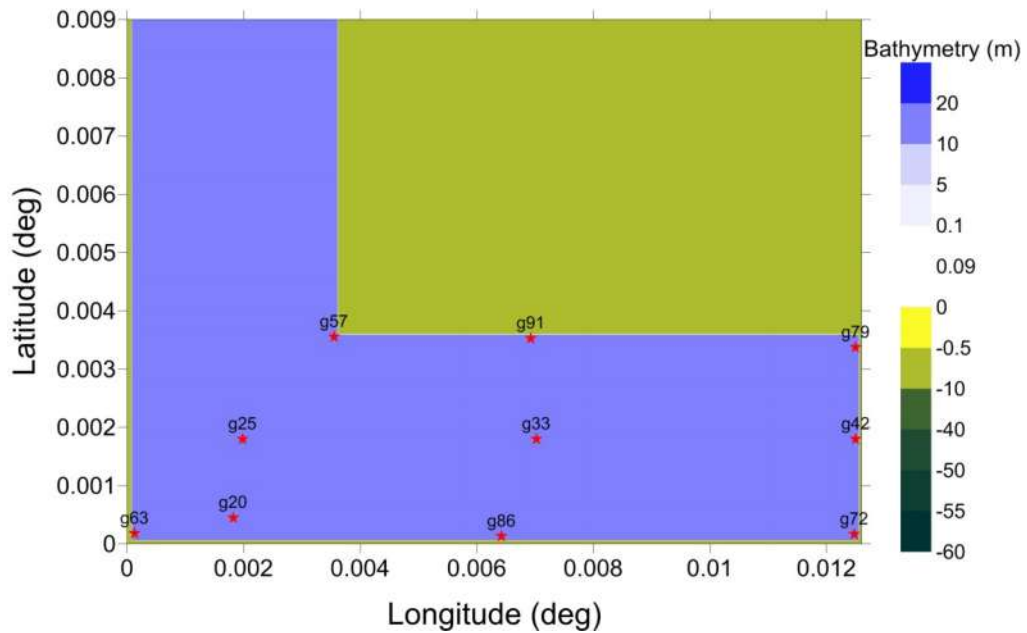
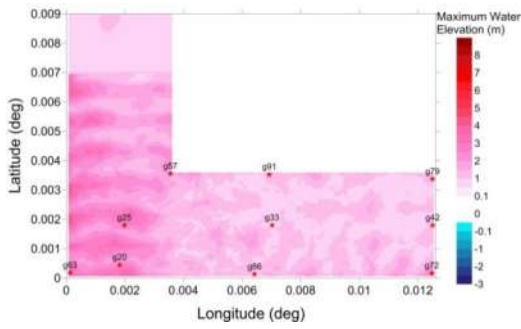


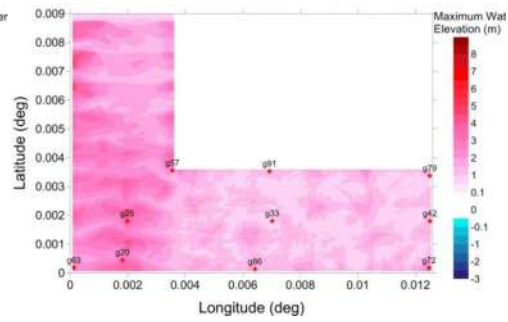
Figure. 4.2. The bathymetry of L-type basin used in simulations with 10 selected gauge points (red stars).

4.2. Results of Numerical Tests and Comparisons

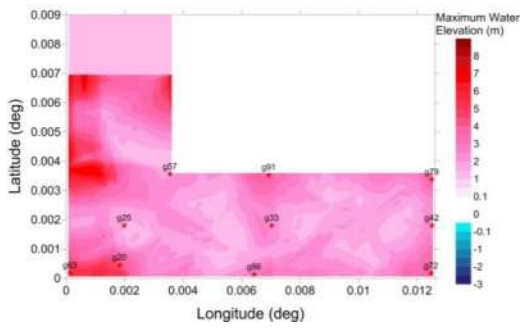
It is important to compute and evaluate the effects of long wave parameters in shallow zone. The spatial distribution of maximum water elevation, maximum current velocity and the minimum Rouse Number computed at each grid in the domain during the simulations. Figure 4.3 shows the maximum water surface elevation for sinusoidal line crest long wave with 1m wave amplitude and $LA/LB=0.8$ in the left column and $LA/LB=1$ in the right column. Figure 4.4 and Figure 4.5 show the maximum current velocity and minimum Rouse Number computed during the same simulations of 40 minute simulation time.



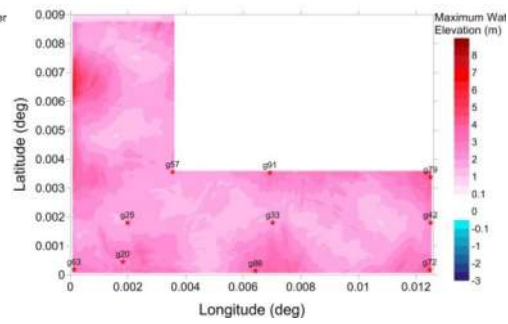
a) T=16 sec



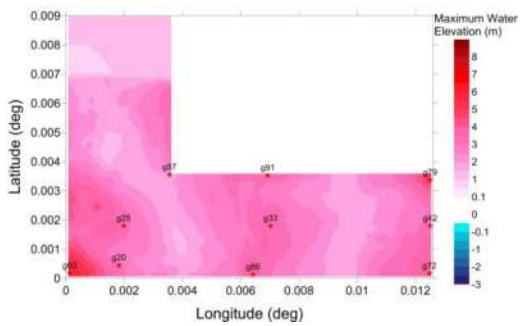
b) T=16 sec



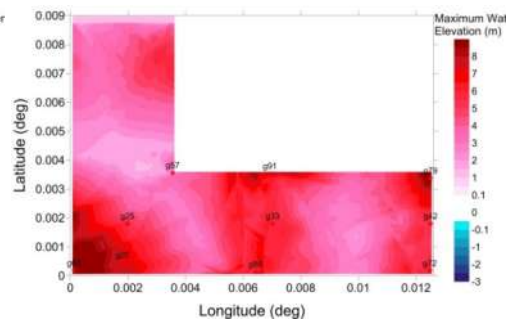
c) T=46 sec



d) T=46 sec

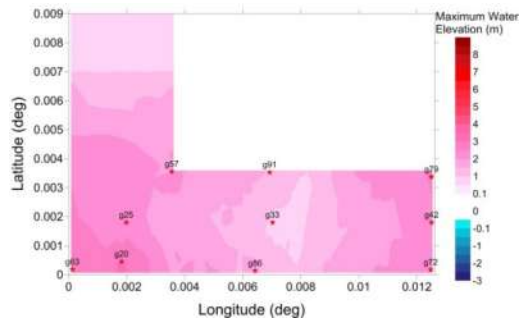


e) T=90 sec

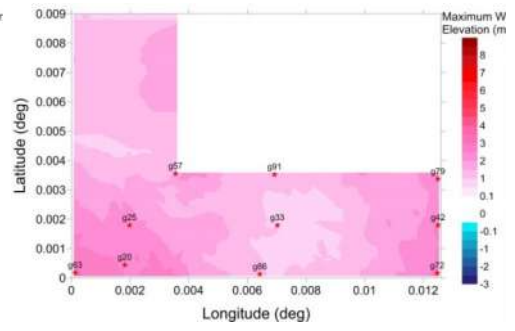


f) T=90 sec

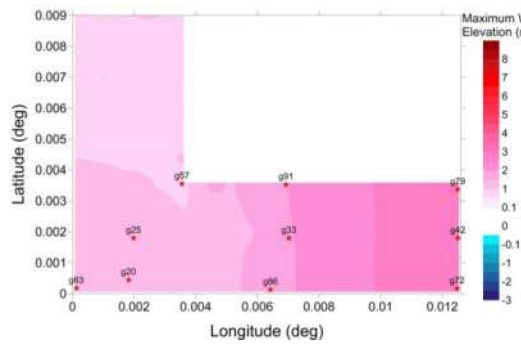
Figure. 4.3. The spatial distribution of maximum water surface elevation (m) computed by the simulation of sinusoidal line crest long wave with 1m wave amplitude with $T=16s$, $T=46s$, $T=90s$, $T=146s$, $T=328s$ for $LA/LB=0.8$ in the left column and $LA/LB=1$ in the right column from a to j respectively.



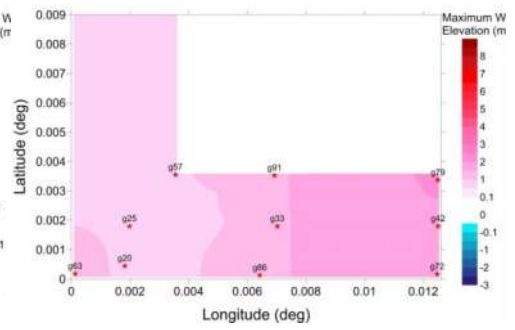
g) T=146 sec



h) T=146 sec

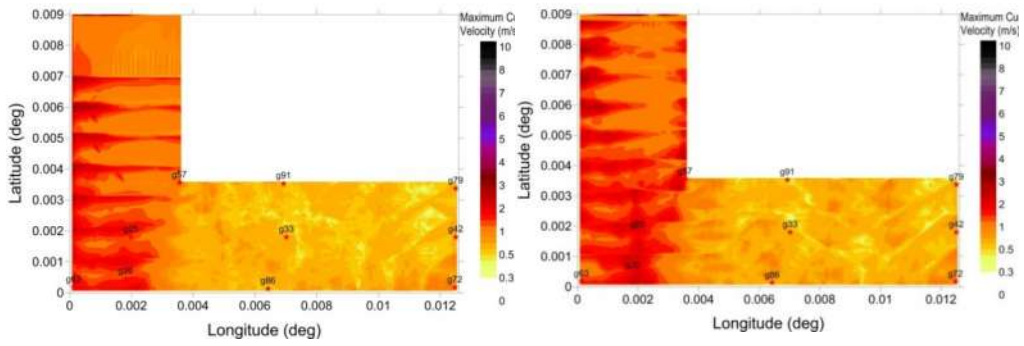


i) T=328 sec



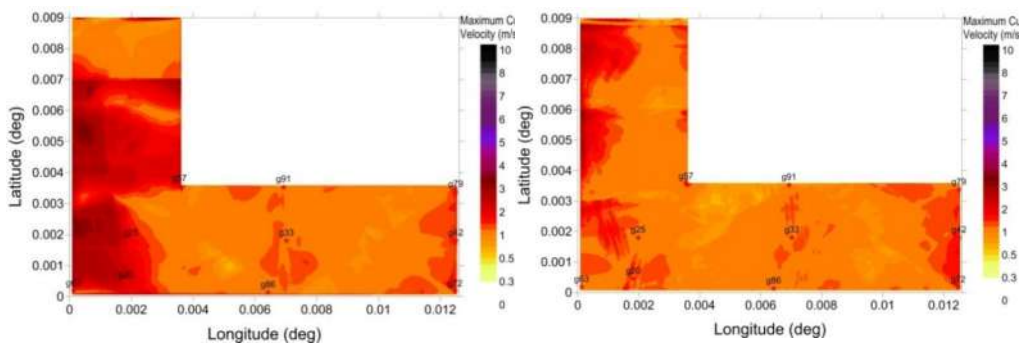
j) T=328 sec

Figure. 4.3.Continued



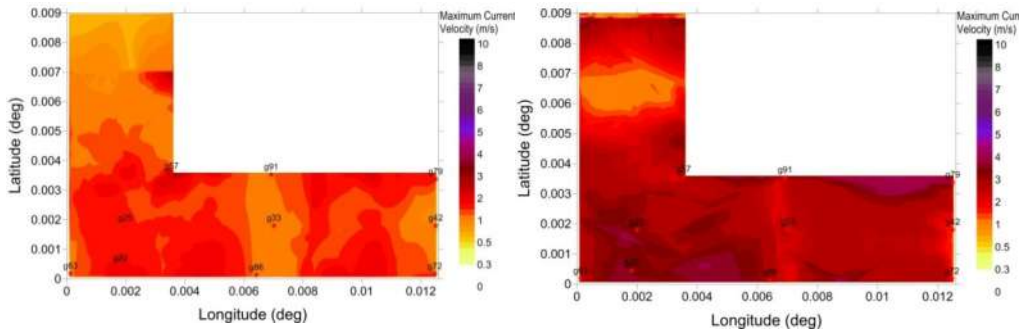
a) T=16 sec

b) T=16 sec



c) T=46 sec

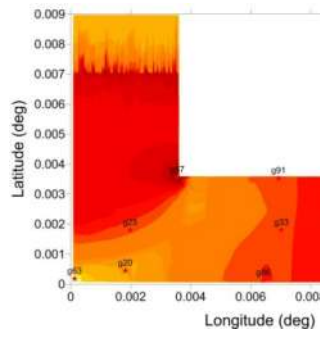
d) T=46 sec



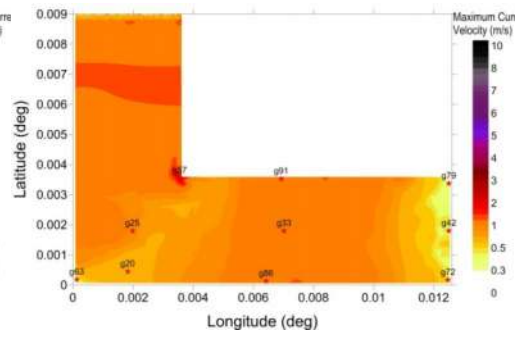
e) T=90 sec

f) T=90 sec

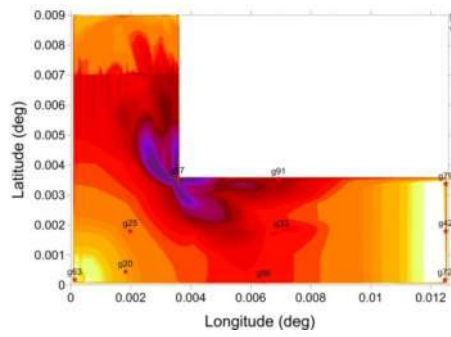
Figure. 4.4. The spatial distribution of maximum current velocity (m/s) computed by the simulation of sinusoidal line crest long wave with 1m wave amplitude with T=16s, T=46s, T=90s, T=146s, T=328s for LA/LB=0.8 in the left column and LA/LB=1 in the right column from a to j respectively.



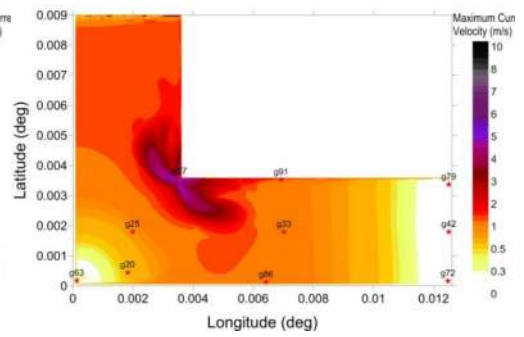
g) T=146 sec



h) T=146 sec

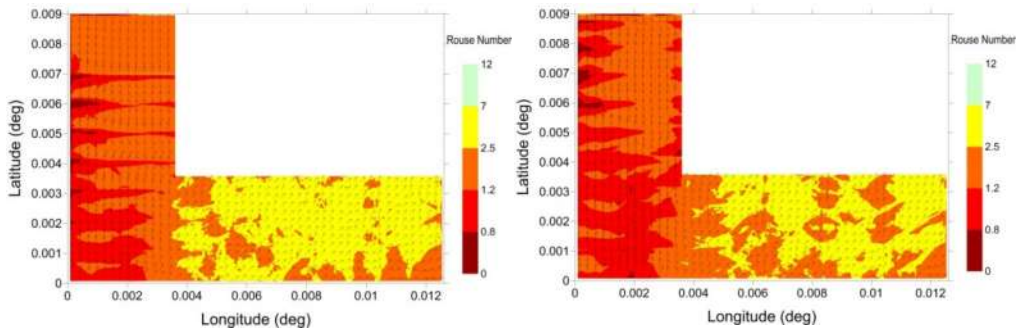


i) T=328 sec



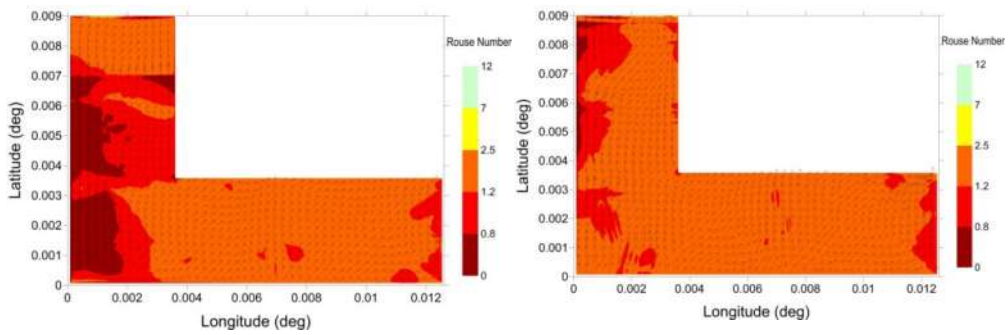
j) T=328 sec

Figure. 4.4. Continued



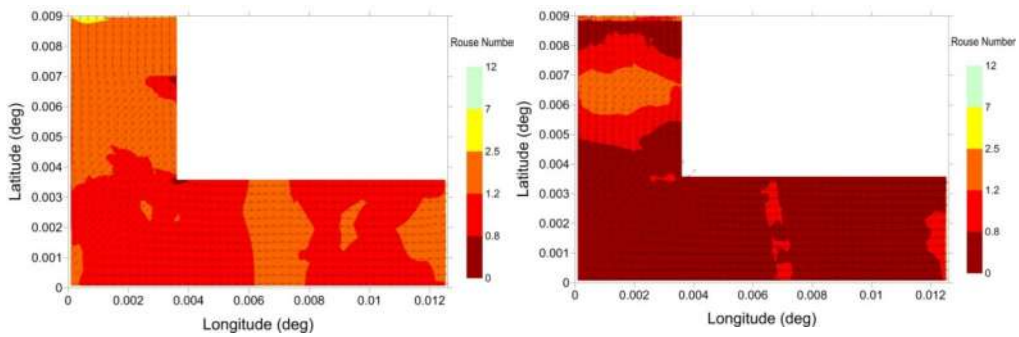
a) T=16 sec

b) T=16 sec



c) T=46 sec

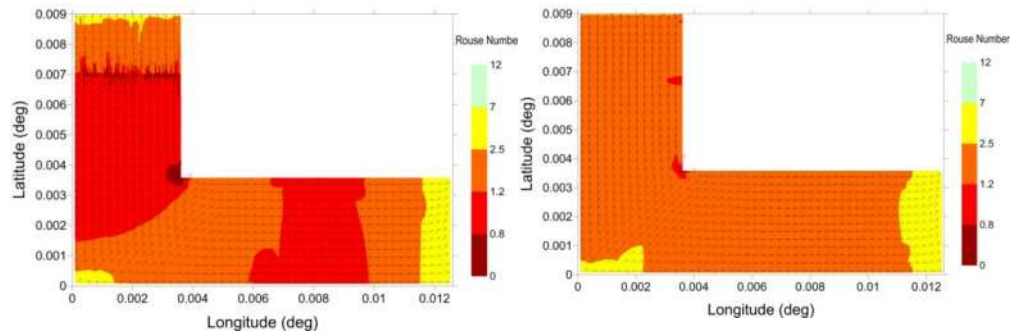
d) T=46 sec



e) T=90 sec

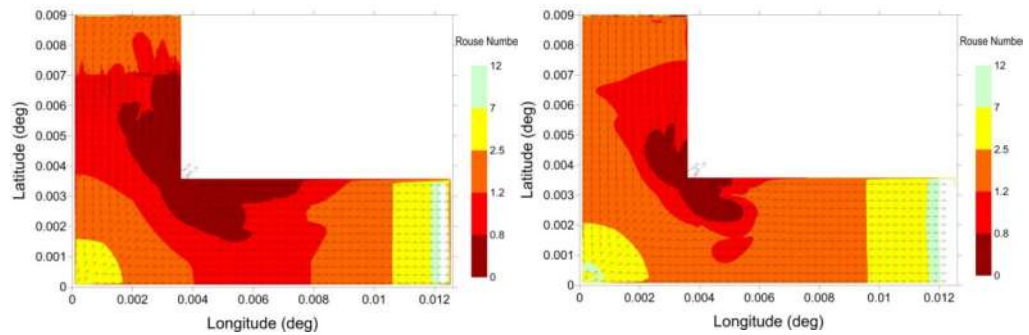
f) T=90 sec

Figure. 4.5. The spatial distribution of minimum Rouse Number computed by the simulation of sinusoidal line crest long wave with 1m wave amplitude with $T=16s$, $T=46s$, $T=90s$, $T=146s$, $T=328s$ for $LA/LB=0.8$ in the left column and $LA/LB=1$ in the right column from a to j respectively. The maximum velocity vectors are also shown on each case.



g) T=146 sec

h) T=146 sec



i) T=328 sec

j) T=328 sec

Figure. 4.5. Continued.

It is obvious from Figure 4.3 that in a same L-type basin, in shorter wave periods the vertical side of the basin, where in input source wave is beginning to propagate, is more exposed to the wave and current amplifications, but in larger wave periods the maximum values of water surface elevation and current velocity are occurred in the horizontal side of the L, after bending. The 90sec (seventh mode of resonance) is a very critical wave period in these simulations, and approximately there are wave and current amplifications in entire basin.

Comparing the results for $LA/LB=0.8$ and $LA/LB=1$ show that except for 90sec wave period, in other wave periods, when $LA/LB=0.8$ the end side of basin which g42, g72 and g79 are placed on it are affected more and expose to the larger

amplifications. Also in other parts of the basin the amplified regions last longer and in a wide range compared to the area affected in $LA/LB=1$ condition.

All of the former figures in this section are simulation results for L-type basin with close end boundary. As for a comparison with open ended boundary of the same basin, one more simulation has been performed using an open ended boundary of the same basin. Figure 4.6 shows the comparison result of spatial distribution of maximum water elevation and maximum current velocity and minimum Rouse number for L-type with open end and close ended boundary of the same shape of L type basin using sinusoidal line crest long wave input with 1m amplitude and the period of 328sec for $LA/LB=1$. Comparisons show that the critical points in the corners in the closed boundary are critical points in the open boundaries too. The only difference is their magnitude and effective radius. In closed boundaries the magnitude of the maximum values are larger.

Figure. 4.7 represents the spatial distribution of maximum water elevation for L-type with open and close boundary in g57, g63, g33 and g42 during 40min simulation of sinusoidal line crest long wave with 1m wave amplitude with T328s for $LA/LB=1$. Similarly Figure 4.8 shows the spatial distribution of maximum current velocity in the mentioned gauge points. The comparisons show that there is not sensible difference for the water surface elevation when the basin is open end except the small phase difference, means the open end basin waves propagate faster. But maximum current velocity in the interior corner point (g57) is larger when the end of basin is closed. In the exterior corner (g63) both of boundary conditions lead to no velocity condition. In addition, the numerical gauge g42 at the end of the basin, the maximum current velocity is obtained as zero when the boundary is closed. But in open boundary condition the maximum current velocity changes according to the input wave period which is used as sinusoidal in this application. In all other gauges the maximum current velocities are found close to each other.

Figure 4.9 to Figure 4.18 represent the time history of the water surface elevation and current velocity between 20min and 30min of a 40 minute simulation in 10 selected gauge points g20, g25, g33, g42, g57, g63, g72, g79, g86 and g91 respectively,

which are shown in Figure 4.2. Therefore, we can summarize the results gauge by gauge according to the explanations below;

In g20 (Figure4.9), in bending side of the L shape, right after bending not in the corner, when $LA/LB=1$, the wave amplitude and current velocity both amplifies in 90sec wave period. When $LA/LB=0.8$, the wave amplifies at 46sec and 146sec and the current amplifies at 46sec and 90sec.

In g25 (Figure 4.10), in the middle of bending part of the L shape, if we join the two corner points of bending part in the basin and plot a cross section, g25 is in the center of the cross section. When $LA/LB=1$, the wave amplitude and current velocity both amplifies in 90sec wave period. When $LA/LB=0.8$, there is no amplification in wave and current.

In g33 (Figure4.11), in the center of the horizontal part of the L shape, when $LA/LB=1$, the wave amplitude and current velocity both amplifies in 90sec wave period. When $LA/LB=0.8$, the current amplifies at 146sec and 328sec but the wave amplitude does not amplify.

In g42 (Figure4.12), in the center of end side of the basin, when $LA/LB=1$, the wave amplitude and current velocity both amplifies in 90sec wave period. The current also amplifies at 46sec wave period. When $LA/LB=0.8$, the wave amplifies at 328sec the current amplifies at 46sec. The similar simulation is performed by Kakinuma et al (2009) to investigate the wave amplification in the first and second mode of oscillations which was approximately 4 (the ratio of the amplified wave to the original wave amplitude in the basin entrance. The wave amplification ratio in this gauge point fits well with result of the mentioned study.

In g57 (Figure4.13), the interior corner point in the bending region of the L shape, in both cases when LA/LB is equal to 1 and 0.8, the current velocity amplifies at 90sec, 146sec and 328 sec, but the water surface elevation does not amplify because of the location of this numerical gauge point.

In g63 (Figure4.14), the exterior corner point in the bending region of the L shape, when $LA/LB=1$, wave amplitude amplifies at 90sec when $LA/LB=0.8$, the wave amplitude amplifies at 90sec and 46sec, but the current velocity does not amplify because of the location of this numerical gauge point.

In g72 (Figure4.15), in the corner point of end side in the basin, when $LA/LB=1$, the wave amplitude amplifies at 90sec wave period and the current velocity amplifies at 46sec and 90 sec wave period. In case $LA/LB=0.8$, the wave amplifies at 46sec and the current amplifies at 46sec and 90sec.

In g79 (Figure4.16), in the corner point of end side in the basin, in both cases when LA/LB is equal to 1 and 0.8, the wave and current amplify at 46sec and 90sec wave periods.

In g86 (Figure4.17), in the horizontal exterior side of the L shape, in the middle point, when $LA/LB=1$, the wave amplitude and current velocity both amplifies in 90sec wave period. When $LA/LB=0.8$, the wave amplifies at 90sec and 146sec and the current amplifies at 146sec and 328sec.

In g91 (Figure4.18), in the horizontal interior side of the L shape, in the middle point, when $LA/LB=1$, the wave amplitude and current velocity both amplifies in 90sec wave period. When $LA/LB=0.8$, the wave amplifies at 90sec and 46sec and the current amplifies at 146sec and 328sec.

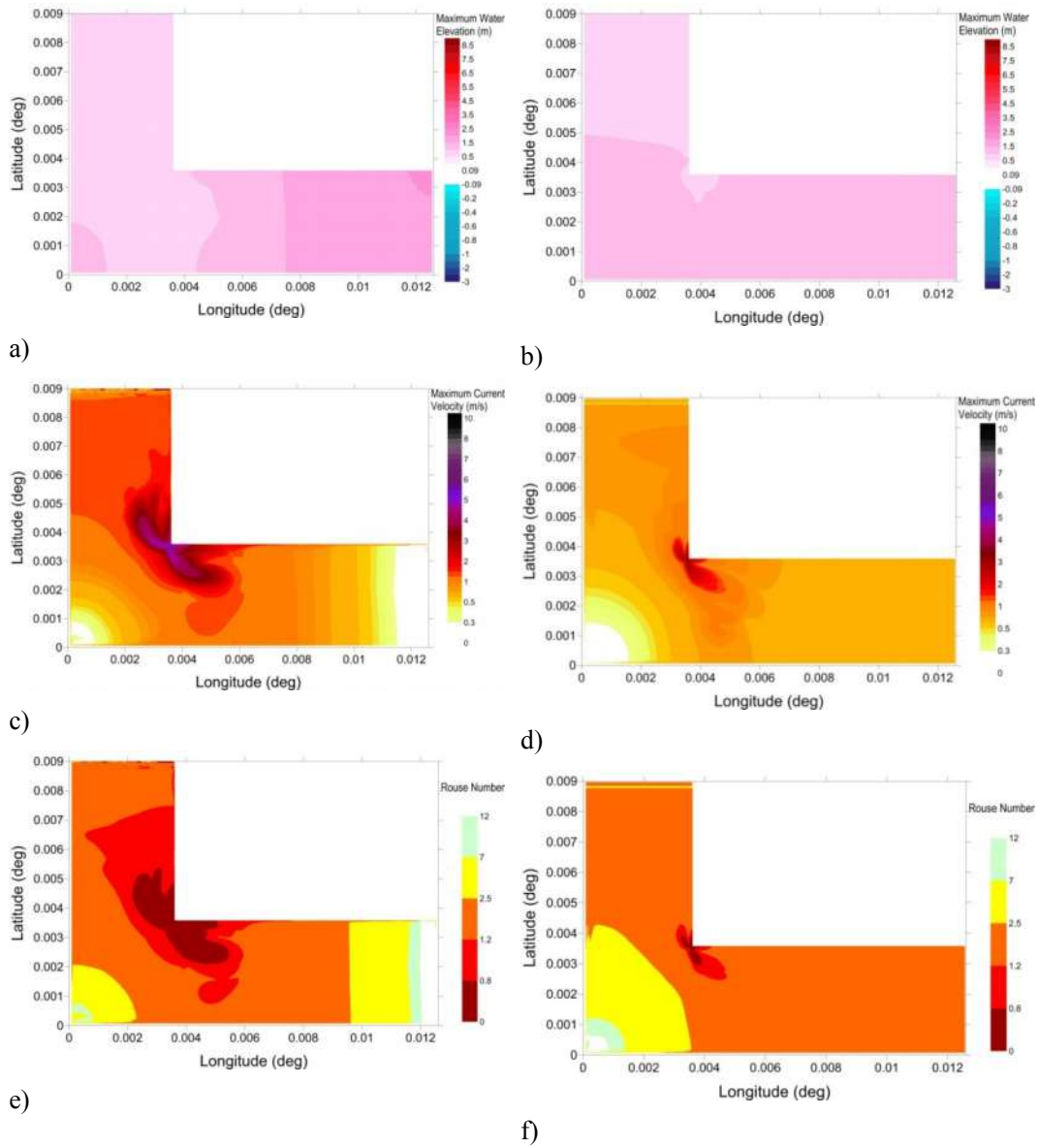
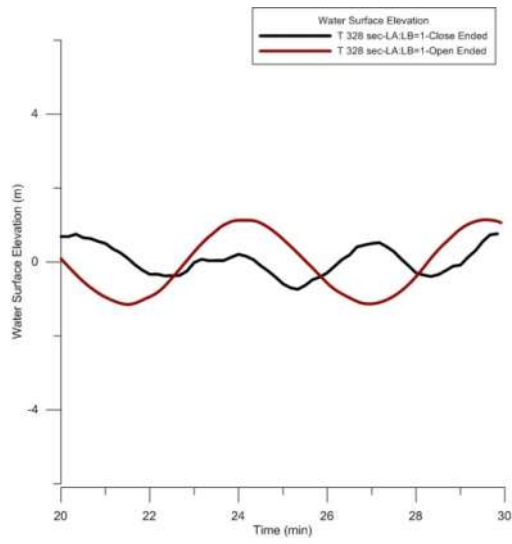
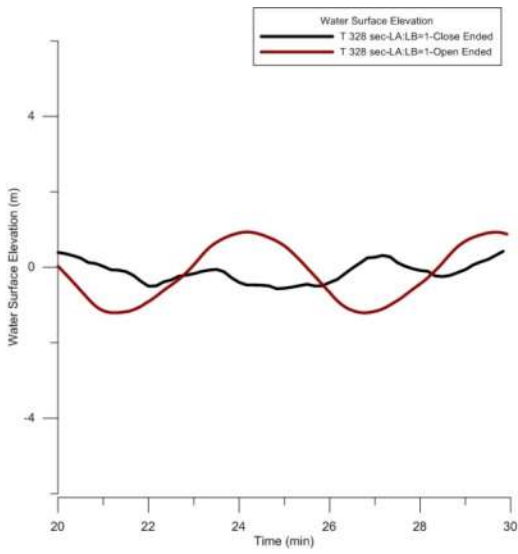
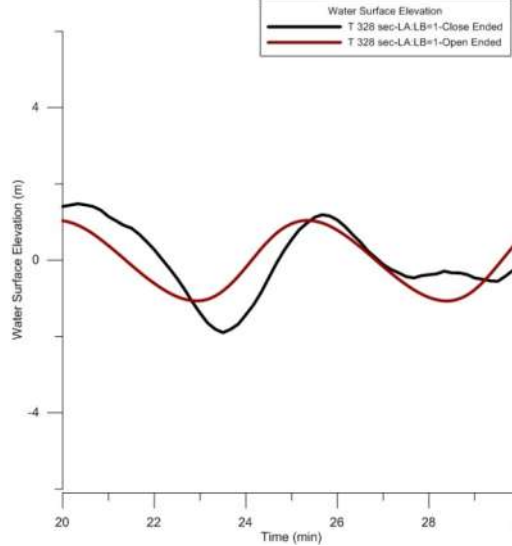
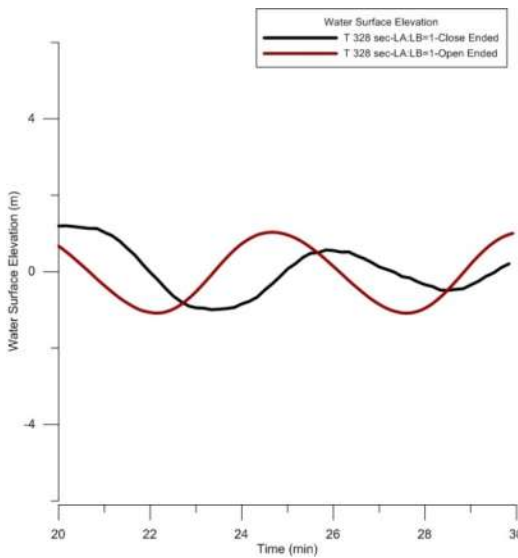


Figure 4.6. The spatial distribution of maximum water elevation for L-type a) with close end boundary, b) with open end boundary, maximum current velocity c) with close end boundary, d) with open end boundary, minimum Rouse Number e) with close end boundary, f) with open end boundary computed by the simulation of sinusoidal line crest long wave with 1m wave amplitude with T328s for LA/LB=1.



a)

b)



c)

d)

Figure. 4.7. The spatial distribution of maximum water elevation for L-type with open (red line) and close (black line) boundary in a) g57, b) g63, c) g33 and d) g42 during 40min simulation of sinusoidal line crest long wave with 1m wave amplitude with T328s for LA/LB=1.

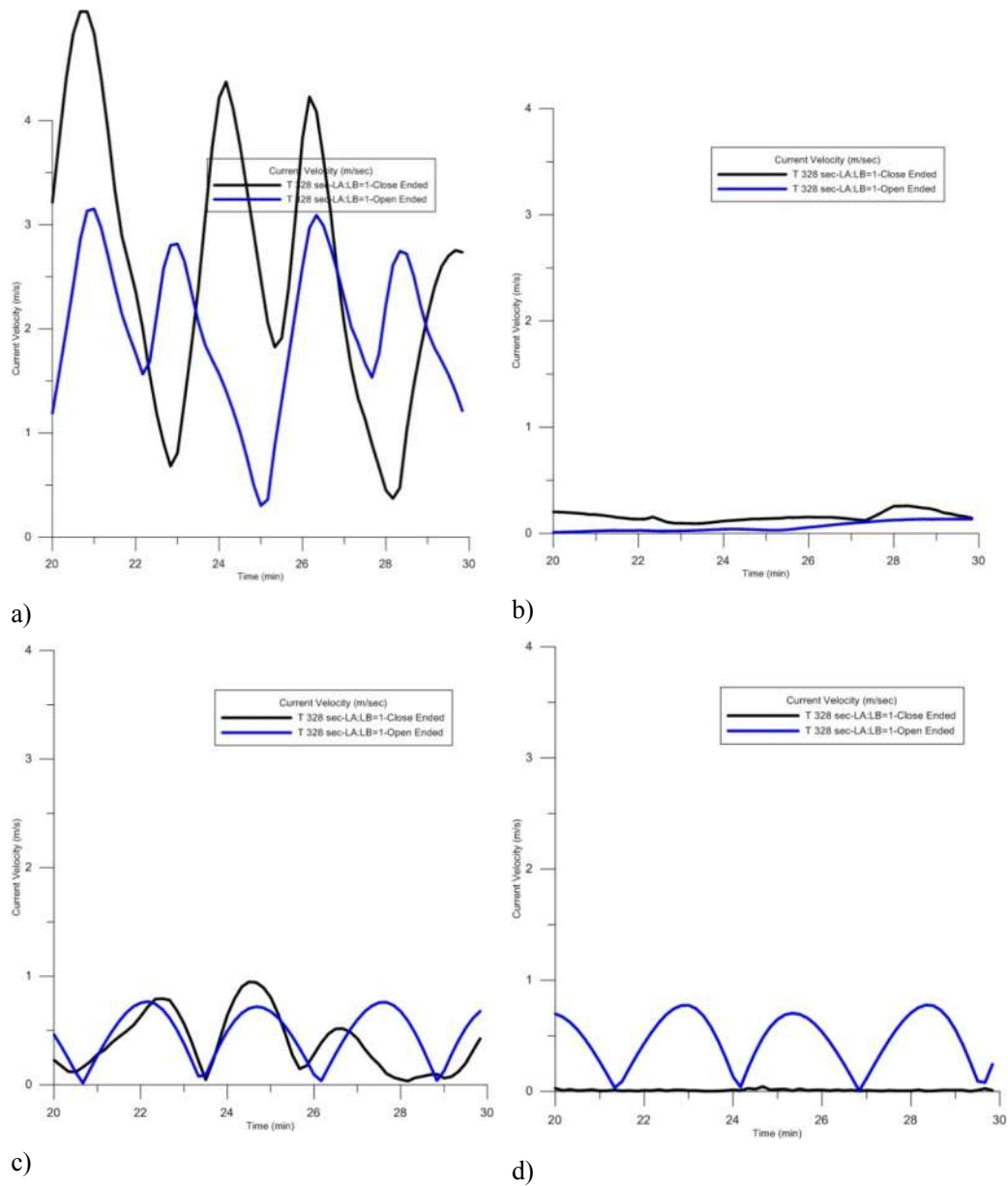


Figure. 4.8. The spatial distribution of maximum current velocity for L-type with open (red line) and close (black line) boundary in a) g57, b) g63, c) g33 and d) g42 during 40min simulation of sinusoidal line crest long wave with 1m wave amplitude with T328s for LA/LB=1.

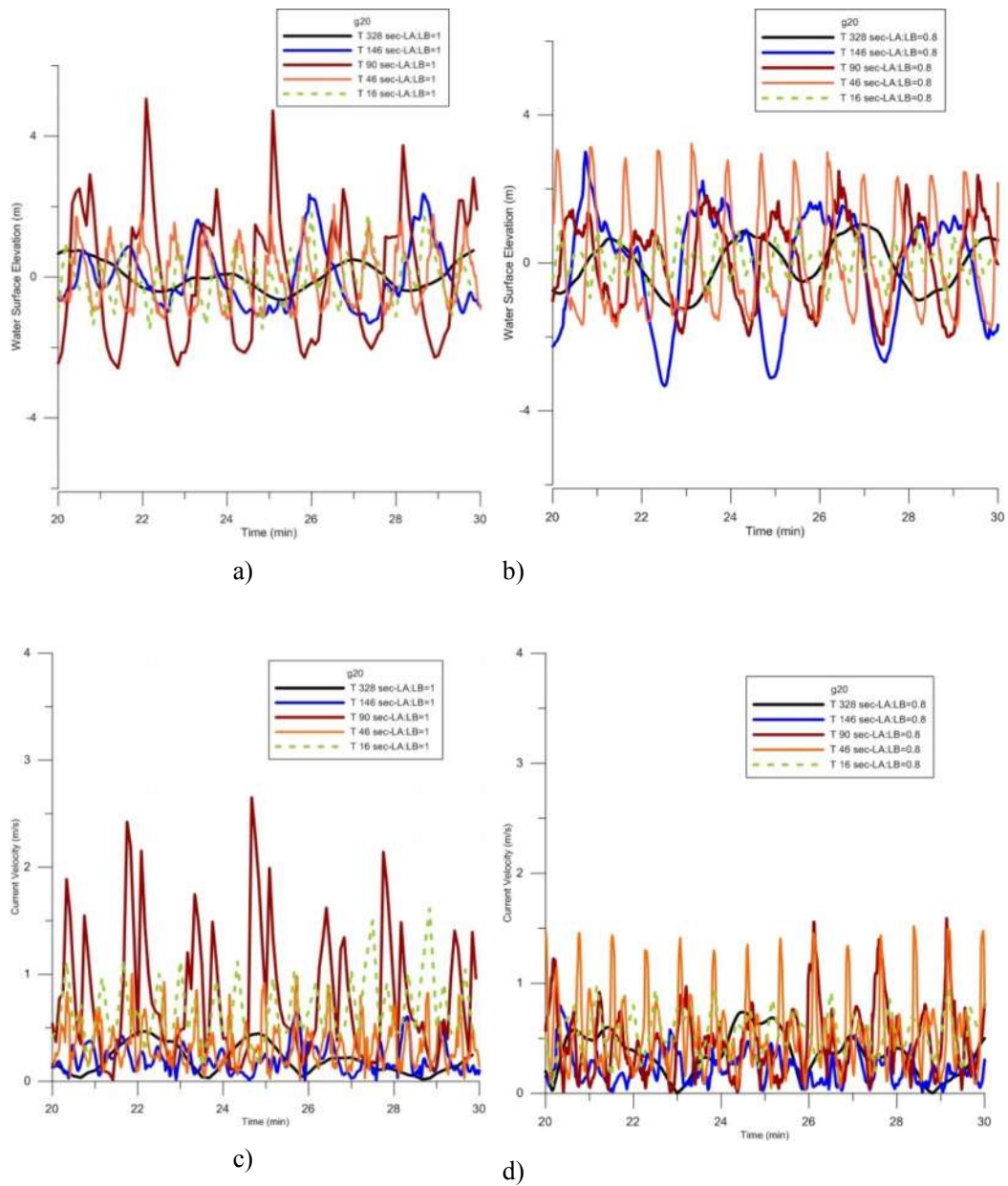


Figure 4.9. Time history of water surface elevation a) when LA/LB=1, b) when LA/LB=0.8, time history of current velocity c) when LA/LB = 1 d) when LA/LB=0.8 in gauge 20.

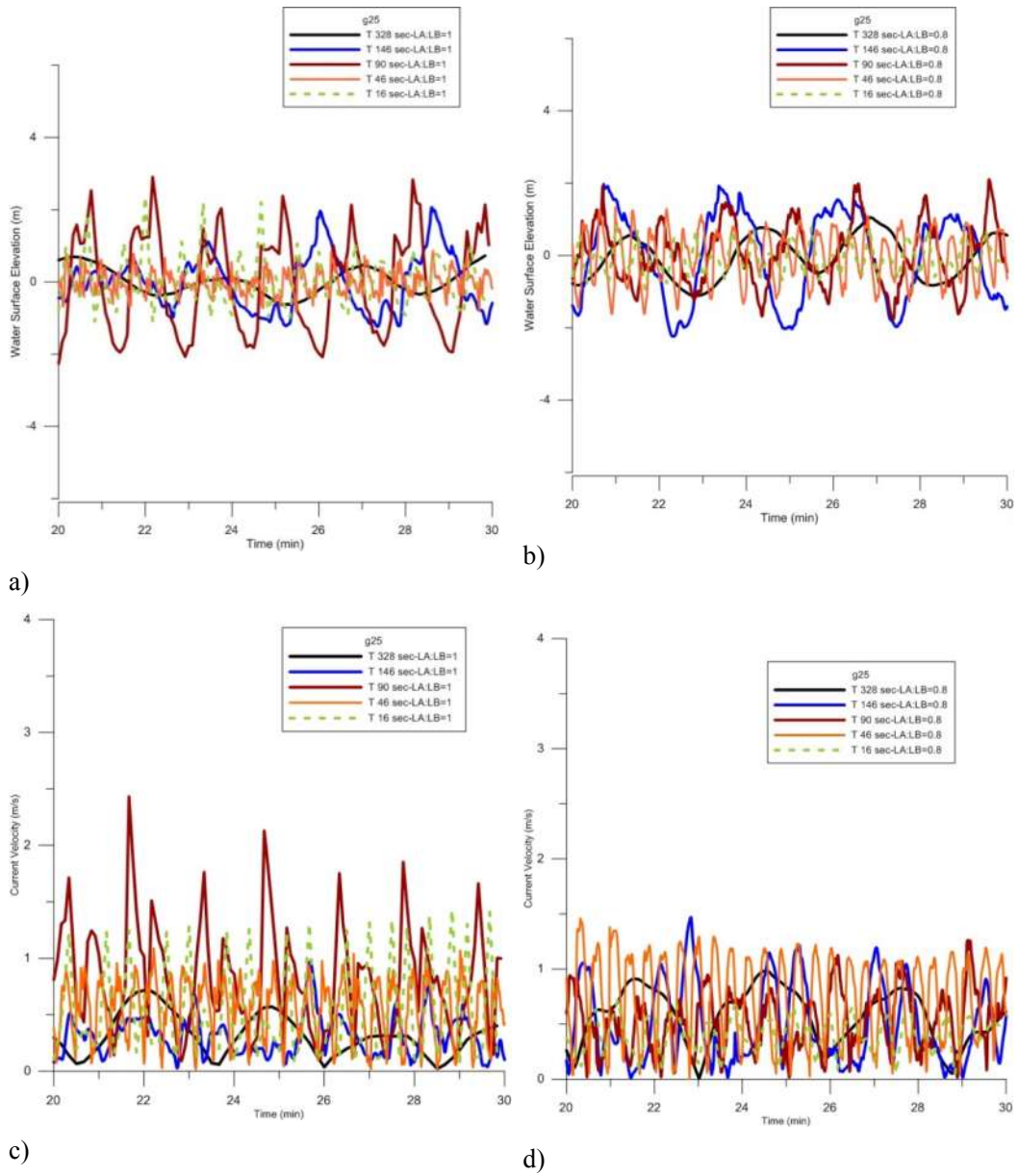
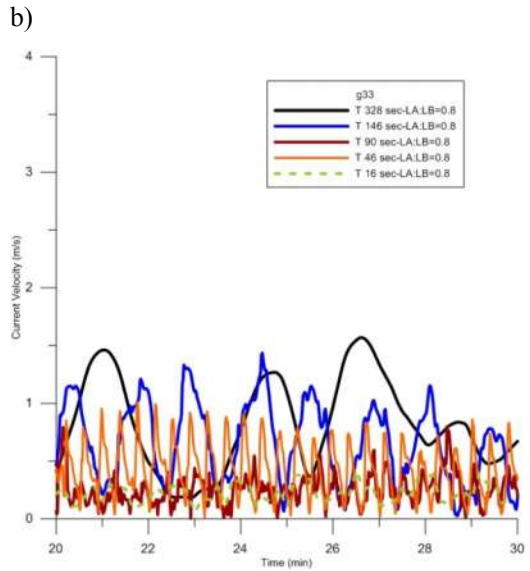
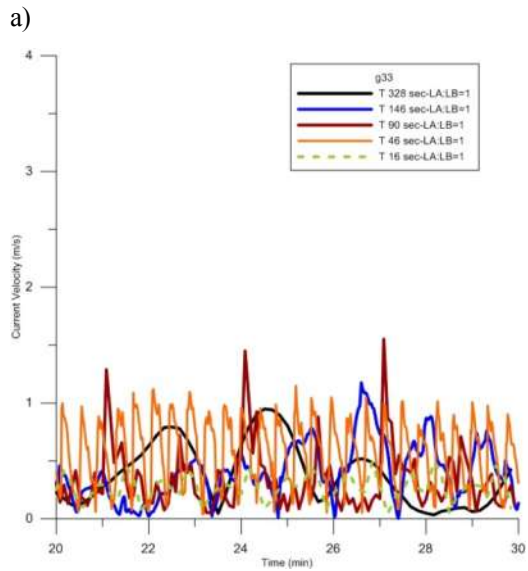
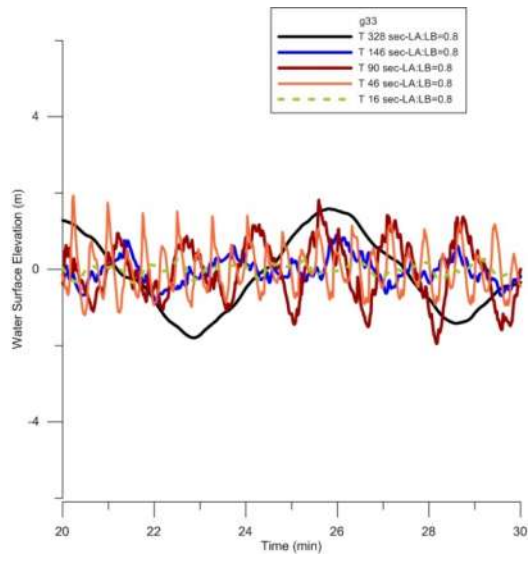
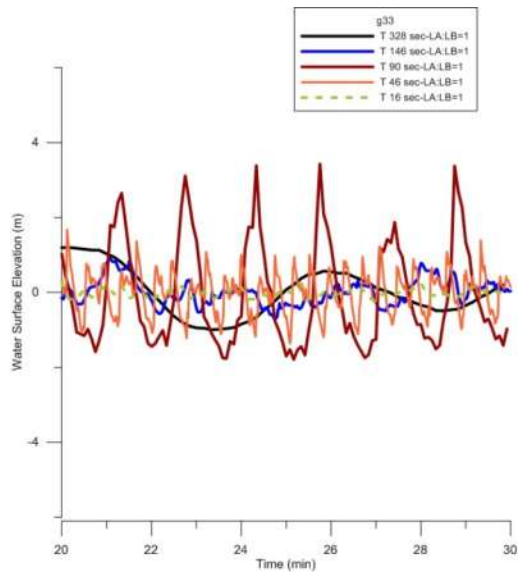


Figure. 4.10. Time history of water surface elevation a) when LA/LB=1, b) when LA/LB=0.8, time history of current velocity c) when LA/LB=1, d) when LA/LB=0.8 in gauge 25.



c) d)

Figure 4.11. Time history of water surface elevation a) when $LA/LB=1$, b) when $LA/LB=0.8$, time history of current velocity c) when $LA/LB=1$, d) when $LA/LB=0.8$ in gauge 33.

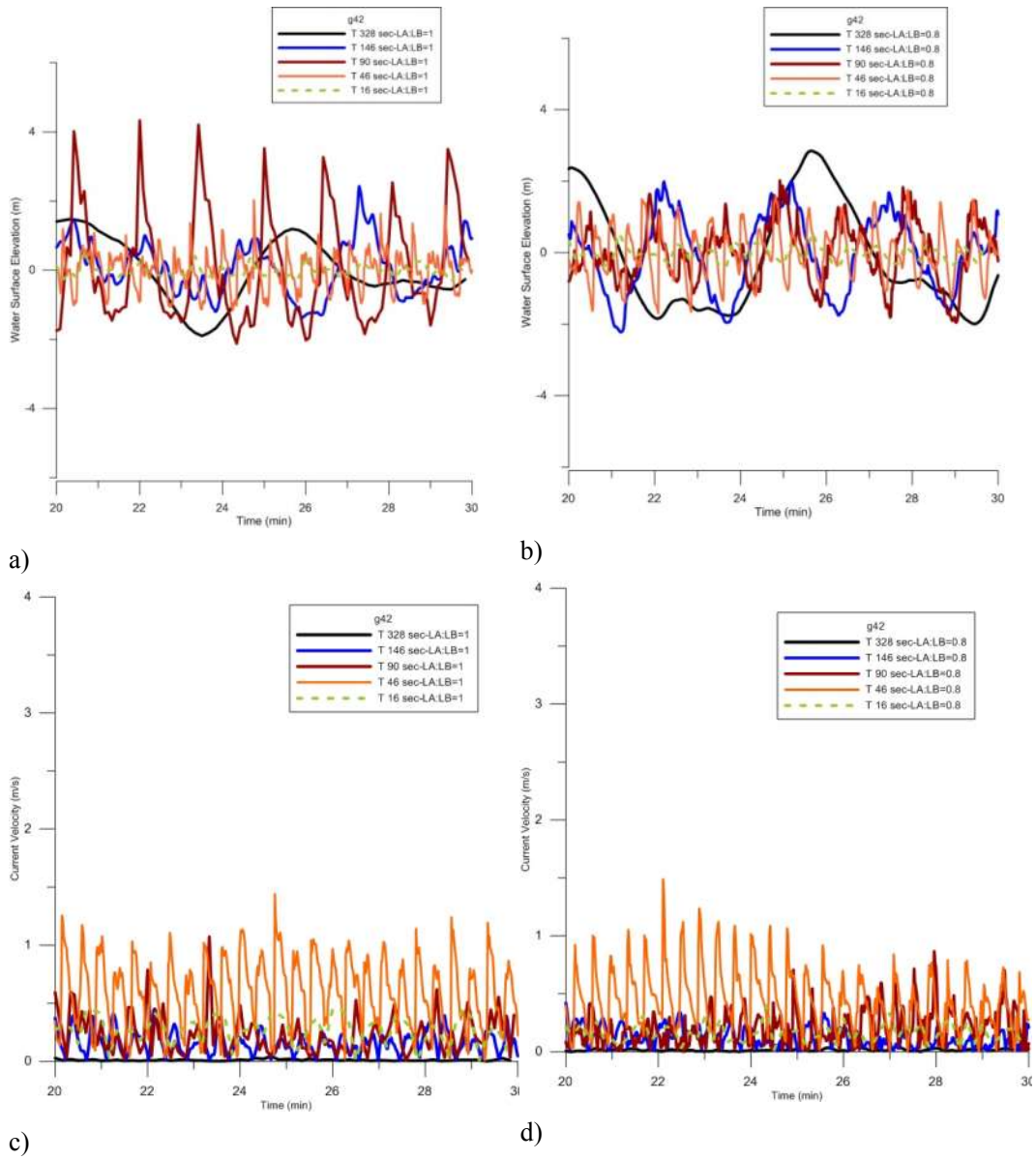


Figure. 4.12. Time history of water surface elevation a) when LA/LB=1, b) when LA/LB=0.8, time history of current velocity c) when LA/LB=1, d) when LA/LB=0.8 in gauge 42.

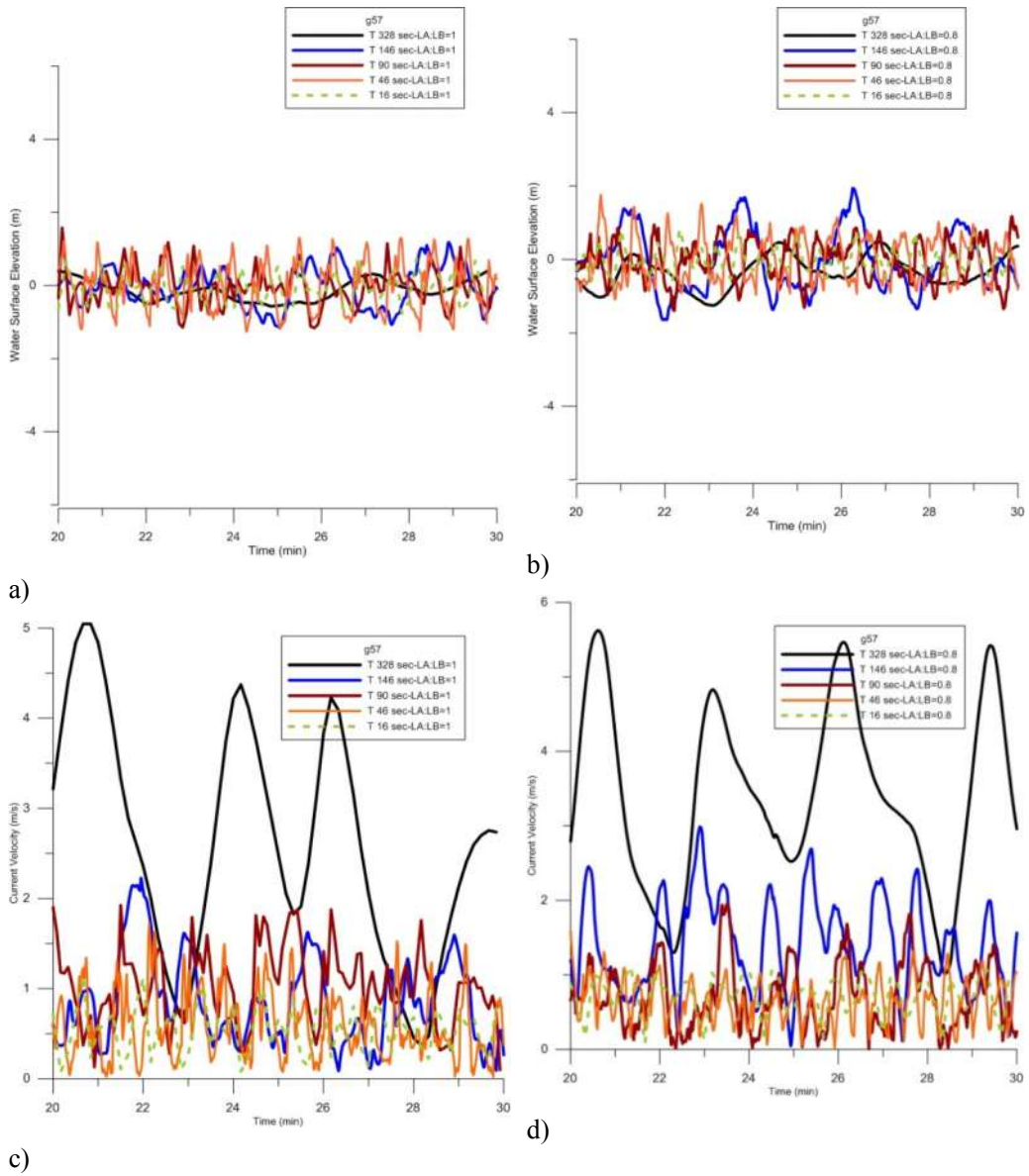


Figure 4.13. Time history of water surface elevation a) when LA/LB=1, b) when LA/LB=0.8, time history of current velocity c) when LA/LB=1, d) when LA/LB=0.8 in gauge 57.

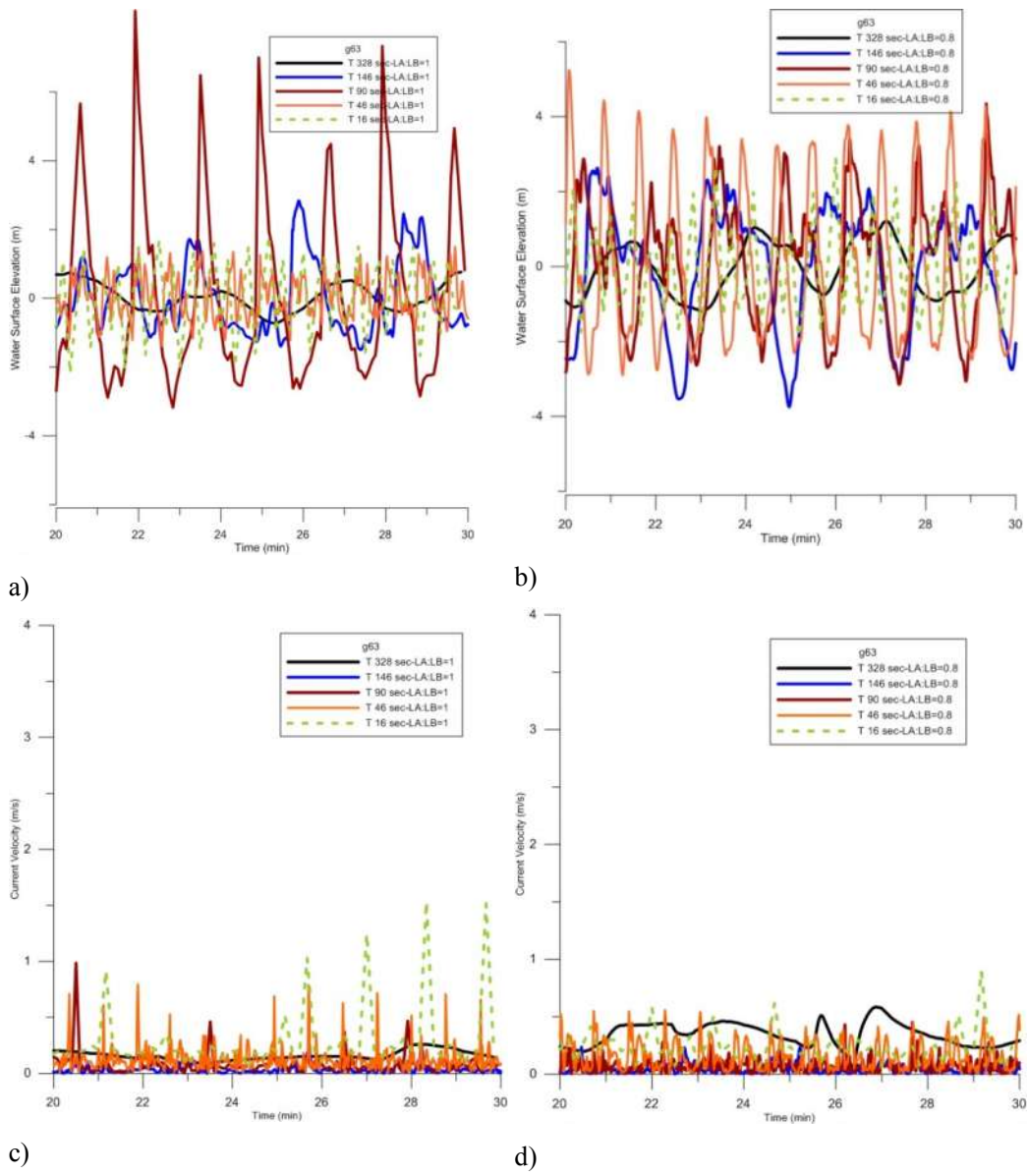
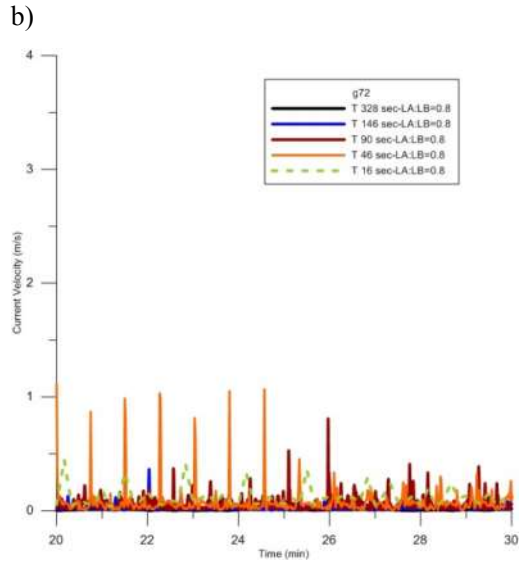
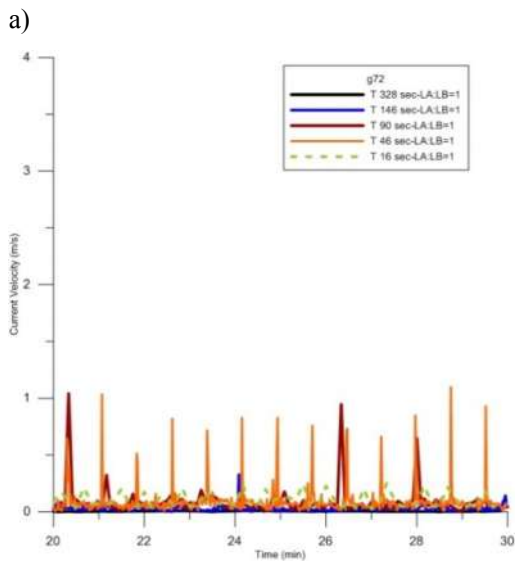
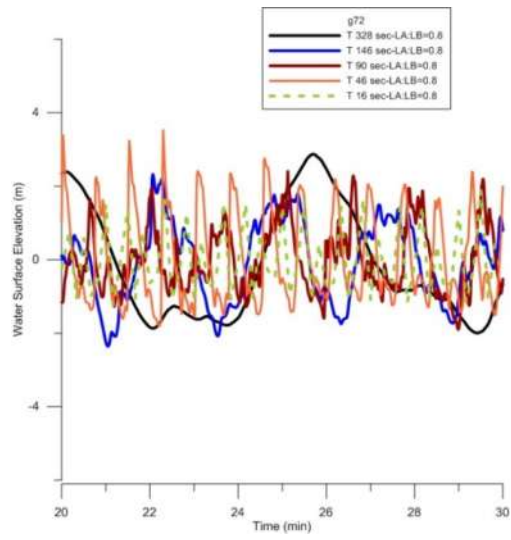
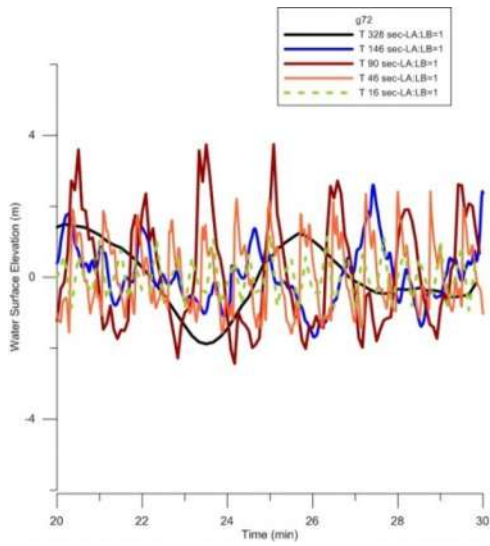


Figure 4.14. Time history of water surface elevation a) when LA/LB=1, b) when LA/LB=0.8, time history of current velocity c) when LA/LB is equal to 1 d) when LA/LB=0.8 in gauge 63.



a) b)
c) d)
Figure 4.15. Time history of water surface elevation a) when $LA/LB=1$, b) when $LA/LB=0.8$, time history of current velocity c) when $LA/LB=1$, d) when $LA/LB=0.8$ in gauge 72.

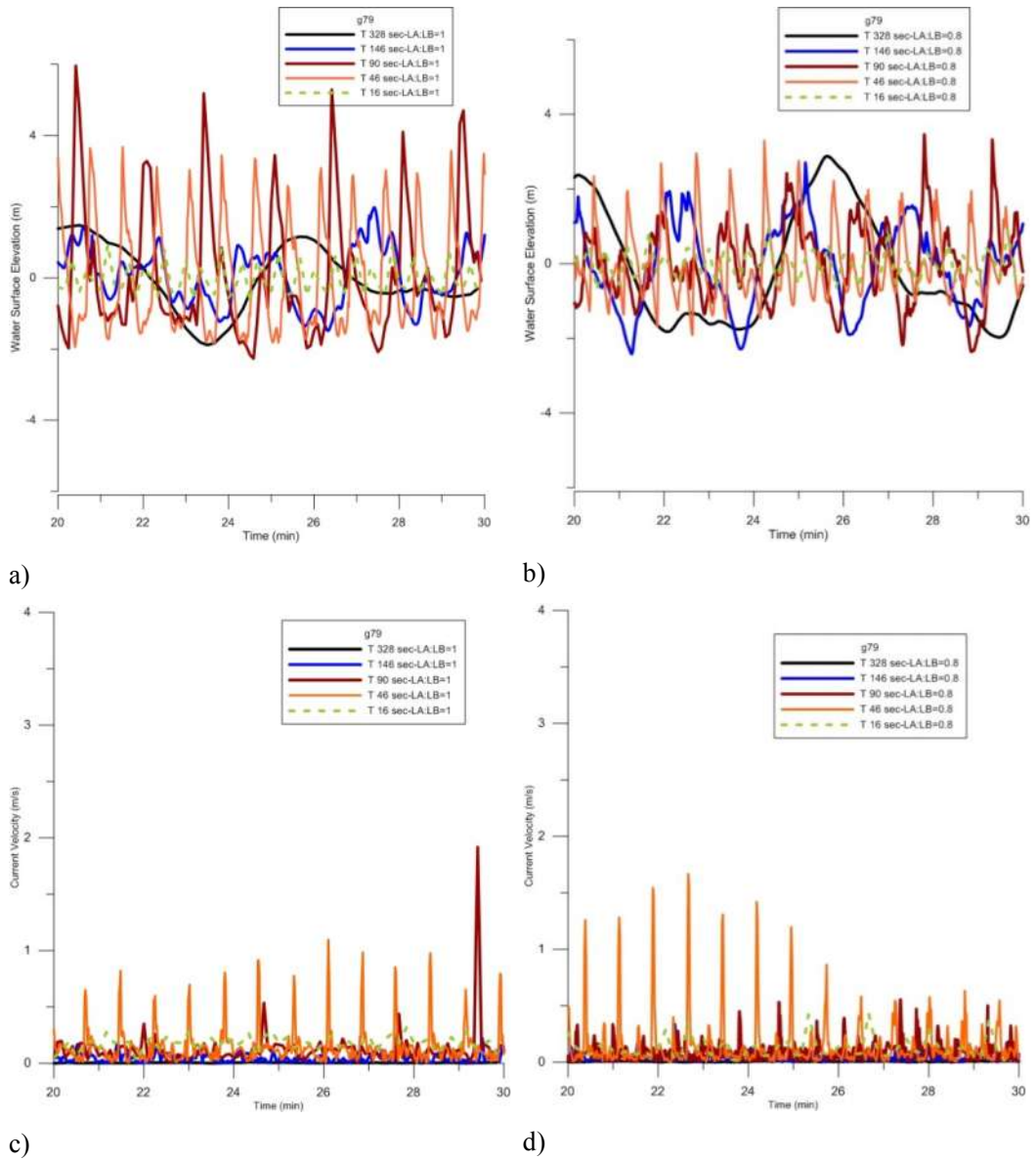
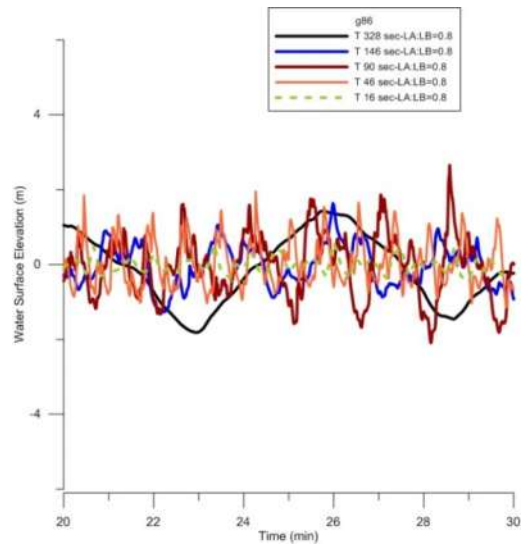
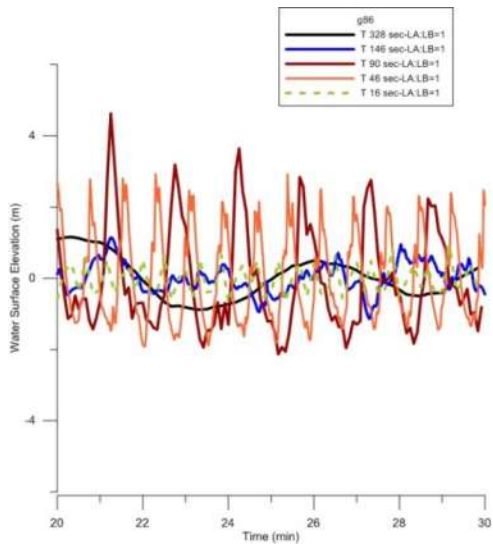
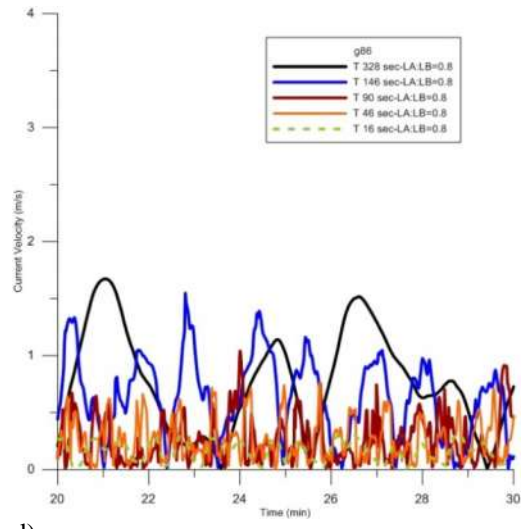
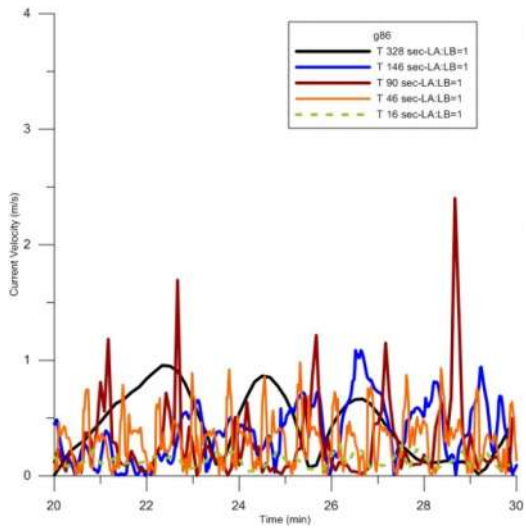


Figure. 4.16. Time history of water surface elevation a) when LA/LB=1, b) when LA/LB=0.8, time history of current velocity c) when LA/LB=1, d) when LA/LB=0.8 in gauge 79.



a)

b)



c)

d)

Figure. 4.17. Time history of water surface elevation a) when LA/LB=1, b) when LA/LB=0.8, time history of current velocity c) when LA/LB=1, d) when LA/LB=0.8 in gauge 86.

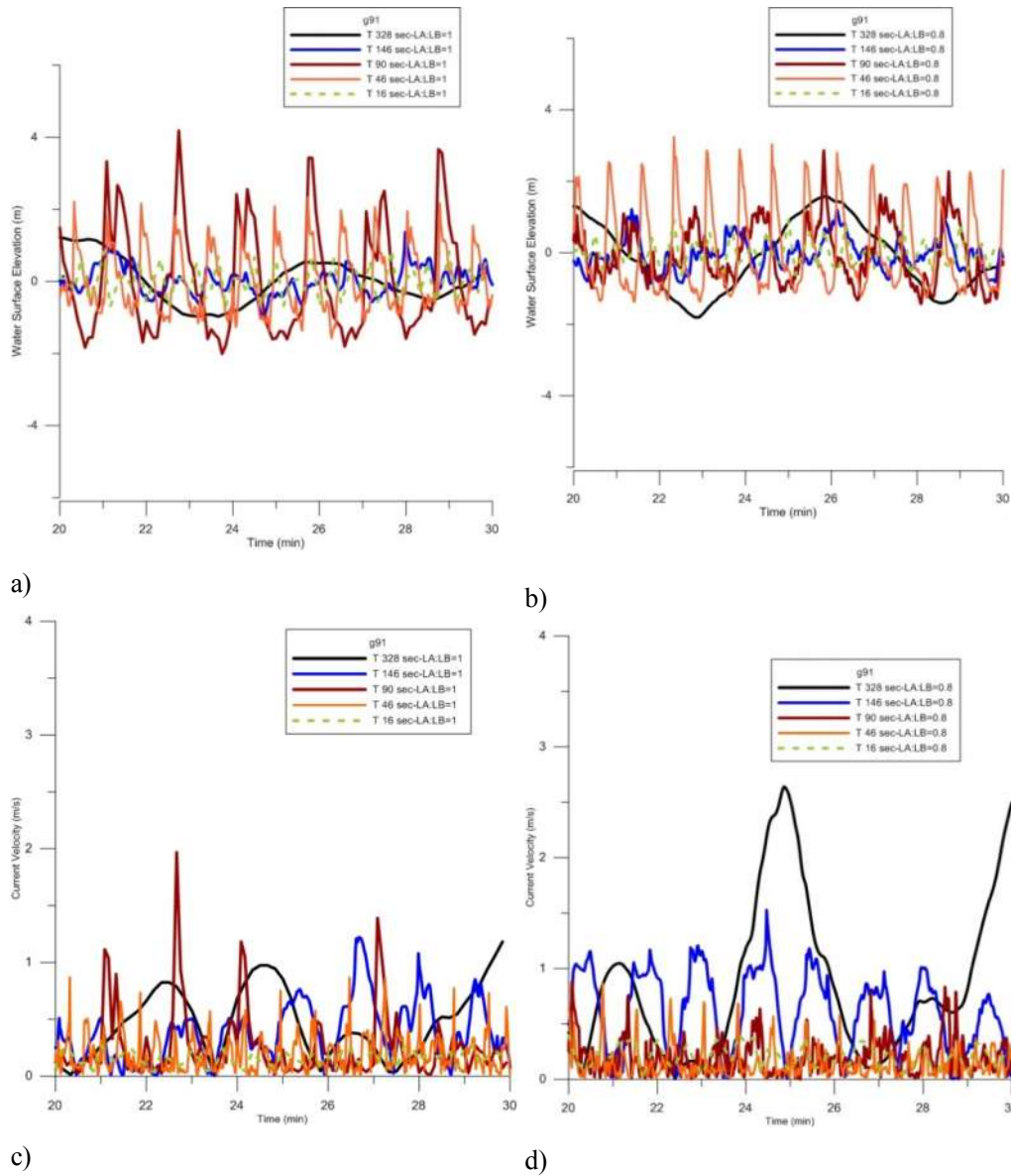


Figure. 4.18. Time history of water surface elevation a) when LA/LB=1, b) when LA/LB=0.8, time history of current velocity c) when LA/LB=1, d) when LA/LB=0.8 in gauge 91.

Table 4.1 to Table 4.5 summarizes the result of maximum water surface elevation, maximum current velocity and minimum Rouse Number at selected gauge points in 16sec wave period to 328sec respectively. The maximum water surface elevation (8.22m) take place when input wave period is 46sec. The maximum current velocity

(7.57m/s) occurs when the wave period is 328sec (second mode of oscillations) and the minimum Rouse Number value (0.24) occur also when the wave period is 328sec as it is expected because the minimum Rouse Number is logical to occur when the current velocity is maximum.

The results in Table 4.1 to Table 4.5 show that the maximum water surface elevation occur mostly in g63 and maximum current velocity takes place in g63 and g57. G63 and g57 are both in bending corners of L shape basin. Therefore we can conclude that the dimensions of the L-type basin do not affect the critical regions of maximum water surface elevation and maximum current velocity and the bending corners are the region. The minimum Rouse Number can also occur in the bending corner of the L-shape basin. Upon the current velocity and its pattern the sediment movement in g63 could be in bed load form if the current is vortex and its value is small (i.e. when the wave period is 146sec and 328sec). But even if the current velocity is vortex, the sediment motion is in wash load form if the current velocity is large enough. The same fact is seen also in Haydarpasa Harbor (Chapter 6).

Table 4.1. *Maximum water surface elevation, maximum current velocity and minimum Rouse Number in g20, g25, g33, g42, g57, g63, g72, g79, g86 and g91 in L-type basin in 16sec wave period in columns 4, 5, 6 respectively. Sinusoidal line crest 1m wave amplitude is from the basin entrance (L/LB=1). X coordinate of the gauge point (second column), Y coordinate of the gauge point (third column). The simulation duration is 40min.*

T 16 sec	Max. Eta (m)		4.8		
	Max. Current (m/S)		4.66		
	Min. Rouse Number		0.39		
Gauge No	X-coord (deg)	Y-coord (deg)	Max eta (m)	Max. Current (m/s)	Min. Rouse Number
g20	0.0018	0.0005	2.3	1.3	1.5
g25	0.0020	0.0018	1.1	1.2	1.6
g33	0.0070	0.0018	0.8	0.8	2.8
g42	0.0125	0.0018	1.2	0.6	3.5
g57	0.0036	0.0036	1.5	1.5	1.3
g63	0.0001	0.0002	3.2	2	1
g72	0.0125	0.0002	2.4	1.7	2.9
g79	0.0125	0.0034	3.1	1.6	3.3
g86	0.0064	0.0001	3	1.7	3
g91	0.0069	0.0035	3.1	1.6	3.4

Table 4.2. *Maximum water surface elevation, maximum current velocity and minimum Rouse Number* in g20, g25, g33, g42, g57, g63, g72, g79, g86 and g91 in L-type basin in 46sec wave period in columns 4, 5, 6 respectively. Sinusoidal line crest 1m wave amplitude is from the basin entrance (L/A/LB=1). X coordinate of the gauge point (second column), Y coordinate of the gauge point (third column). The simulation duration is 40min.

T 46 sec	Max. Eta (m)		8.22		
	Max. Current (m/S)		4.53		
	Min. Rouse Number		0.4		
Gauge No	X-coord (deg)	Y-coord (deg)	Max eta (m)	Max. Current (m/s)	Min. Rouse Number
g20	0.0018	0.0005	4.5	2.3	0.8
g25	0.0020	0.0018	1.8	2	1
g33	0.0070	0.0018	2.4	1.4	1.3
g42	0.0125	0.0018	2.7	1.6	1.1
g57	0.0036	0.0036	1.9	2.3	0.8
g63	0.0001	0.0002	5	2.4	0.8
g72	0.0125	0.0002	4.1	1.7	1
g79	0.0125	0.0034	3.8	1.8	1
g86	0.0064	0.0001	3	1	1.9
g91	0.0069	0.0035	4	1.3	1.5

Table 4.3. *Maximum water surface elevation, maximum current velocity and minimum Rouse Number* in g20, g25, g33, g42, g57, g63, g72, g79, g86 and g91 in L-type basin in 90sec wave period in columns 4, 5, 6 respectively. Sinusoidal line crest 1m wave amplitude is from the basin entrance (LA/LB=1). X coordinate of the gauge point (second column), Y coordinate of the gauge point (third column). The simulation duration is 40min.

T 90 sec	Max. Eta (m)		Y-coord (deg)	Max eta (m)	Max. Current (m/s)	Min. Rouse Number
	Max. Current (m/S)	6				
	Min. Rouse Number	0.34				
Gauge No	X-coord (deg)					
g20	0.0018	0.0005	0.0005	3.1	2	1
g25	0.0020	0.0018	0.0018	3.4	1.7	1
g33	0.0070	0.0018	0.0018	3.3	1.4	1.4
g42	0.0125	0.0018	0.0018	3.3	1	2
g57	0.0036	0.0036	0.0036	1.6	3.5	0.5
g63	0.0001	0.0002	0.0002	6	1.2	1.5
g72	0.0125	0.0002	0.0002	4	1.6	1
g79	0.0125	0.0034	0.0034	5	1.5	1
g86	0.0064	0.0001	0.0001	4	1.3	1.5
g91	0.0069	0.0035	0.0035	3.2	1.4	1.5

Table 4.4. *Maximum water surface elevation, maximum current velocity and minimum Rouse Number* in g20, g25, g33, g42, g57, g63, g72, g79, g86 and g91 in L-type basin in 146sec wave period in columns 4, 5, 6 respectively. Sinusoidal line crest 1m wave amplitude is from the basin entrance (L/LB=1). X coordinate of the gauge point (second column), Y coordinate of the gauge point (third column). The simulation duration is 40min.

T 146 sec	Max. Eta (m)		Y-coord (deg)	Max eta (m)	Max. Current (m/s)	Min. Rouse Number
	Max. Current (m/S)	3.19				
	Min. Rouse Number	4.82				
Gauge No	X-coord (deg)	0.37	Max eta (m)	Max. Current (m/s)	Min. Rouse Number	
g20	0.0018	0.0005	3	0.9	2.1	
g25	0.0020	0.0018	2.1	1.5	1.2	
g33	0.0070	0.0018	1	1.6	1	
g42	0.0125	0.0018	2.2	0.6	3.5	
g57	0.0036	0.0036	2	3.5	0.5	
g63	0.0001	0.0002	2.9	0.3	7	
g72	0.0125	0.0002	2.6	0.5	5	
g79	0.0125	0.0034	2.9	0.5	5	
g86	0.0064	0.0001	1.8	1.6	1	
g91	0.0069	0.0035	1.7	1.6	1	

Table 4.5. Maximum water surface elevation, maximum current velocity and minimum Rouse Number in g20, g25, g33, g42, g57, g63, g72, g79, g86 and g91 in L-type basin in 328sec wave period in columns 4, 5, 6 respectively. Sinusoidal line crest 1m wave amplitude is from the basin entrance (L/A/LB=1). X coordinate of the gauge point (second column), Y coordinate of the gauge point (third column), Y coordinate of the gauge point (third column). The simulation duration is 40min.

T 328 sec	Max. Eta (m)		2.88		
	Max. Current (m/s)		7.57		
	Min. Rouse No.		0.24		
Gauge No	X-coord (deg)	Y-coord (deg)	Max eta (m)	Max. Current (m/s)	Min. Rouse Number
g20	0.0018	0.0005	1.5	0.9	2.2
g25	0.0020	0.0018	1.4	1.2	1.5
g33	0.0070	0.0018	2	1.9	1
g42	0.0125	0.0018	3	0.8	2
g57	0.0036	0.0036	1	7	0.1
g63	0.0001	0.0002	1.8	0.9	2
g72	0.0125	0.0002	3	0.4	6.3
g79	0.0125	0.0034	3	0.9	2
g86	0.0064	0.0001	1.9	1.8	1
g91	0.0069	0.0035	2	2.9	0.5

4.3. Discussions of the Results

The effect of long waves on the wave and current amplification is studied in this chapter. The model is selected similar to the L-type model Kakinuma et al. studied in 2009. They have studied the wave amplification during the first and second mode of oscillations in the end side of the basin (g42). In order to verify the model used in this study L-Type basin with $LA/LB=0.8$ and $LA/LB=1$ in g42 is re-modeled and the wave amplifications in 46sec and 146sec wave period are compared with Kakinuma et al. (2009). After verifying the model, the behavior of L-type basin is studied for wave and current amplification and the sediment motion as a morphological change pattern are investigated via 10 selected gauge points. The results shown in Figures 4.3 to 4.15 and the Tables 4.1 to 4.5 can be summarized as below:

The corner points on the sides of the basin are always the critical points. G63 in the exterior corner of the L-shape is where the water surface elevation amplifies extremely, but there is no current amplification. G57 in the interior corner of the L-shape is where the current velocity amplifies extremely, but there is no wave amplification. The pattern of sediment motion in these mentioned two corner points depend on both current pattern and amount. In vortex currents, if the current is large the sediment move in wash load form but if the current is small enough sediment motion are in bed load mode and therefore, erosion is expected in these regions.

In all other points, wave and current amplify simultaneously if the wave period meets the resonance period in related basin. Therefore, in g20, g25, g33, g42, g72, g79, g86 and g91 both wave and current amplifications are predictable. However, it is noticeable that in interior side of L shape basin, the amplification is higher than the exterior side of it.

Large periods affect the end parts of the basin more than the smaller wave periods. This phenomenon is more sensible in wave amplification and not in the current amplifications. The effect of the L-type basin's side dimensions is negligible. The amplification factor especially for the current is a little larger in vertical part of the

basin (before bending) when its dimension is smaller, like what occurs in in the case $LA/LB=0.8$.

CHAPTER 5

SEDIMENTATION BY TSUNAMI, CASE STUDY IN ANTALYA

The sediment motion under tsunami can be observed by monitoring the spatial and temporal changes of Rouse number. Therefore Rouse number is selected a parameter to investigate the sediment movement morphological changes and sediment transport modes at coastal areas if it is exposed by tsunami(s). The modes of sediment transport can be categorized to bed load, suspended load, wash load and no motion (Yeh et al., 2008). Since, maximum current does not occur at the same time for the entire domain the instantaneous Rouse numbers should be computed during the simulations.

Antalya region in Mediterranean Sea at south of Turkey is selected as a case study area for investigation of the spatial and temporal distributions of Rouse Number. Pamuk (2014) computed spatial distribution of instantaneous values of Rouse number at each time step through the fine grid simulation of tsunami inundation using the numerical tool NAMI DANCE (NAMI DANCE Manual, 2010). Tanaka et al. (2012) studied about the morphological changes in Natori River and compared the results with the field survey by Mori et al. (2012) after 2011 Great East Japan Tsunami. Due to the huge incident tsunami wave, vast erosions occurred in Sendai plain. Also the river beds eroded since they are located close to the river entrance. Another interesting findings of their studies are the path of flow return flow which followed not only the existing river beds but also along the the river beds at old times.

According to the similarity between Sendai plain Nattori region and Antalya Belek region, in this thesis, Antalya Belek region is selected as a case study area. Therefore the simulation domain is selected at East of Antalya city at Belek beach. One of the important tsunami sources is used in simulations. The time histories of water level at the border of the study domain are computed in simulations. The computed time histories of water level are inputted to the fine grid simulation of tsunami inundation and during the simulation the Rouse Number is computed (Kian et al., 2015c).

In the Eastern Mediterranean, Aegean Sea, Marmara and Black Sea, there have been more than 130 tsunami events which are presented in detail by Altinok et al. (2011). The source used for this study is considered according to Pamuk (2014). The parameters used for the source are summarized in Table 5.1. This source can generate an earthquake with a magnitude of $M=8.5$. The selected scenario for this region can be considered one of the worst case scenarios in Antalya area. In Figure 5.1, location and initial sea state of selected tsunami source is plotted.

Table 5.1. Fault parameters of tsunami source (Pamuk, 2014)

Epicenter	32.0 E 34.75 N
Length of Fault (km)	230
Strike Angle ($^{\circ}$ W)	290
Width of Fault (km)	158
Focal Depth (km)	35
Dip Angle (degrees)	30
Slip Angle (degrees)	70
F displacement (m)	4.35
Height of Initial Wave (m)	1.941
Max. Positive amp. (m)	1.886
Min. Negative amp. (m)	-0.055

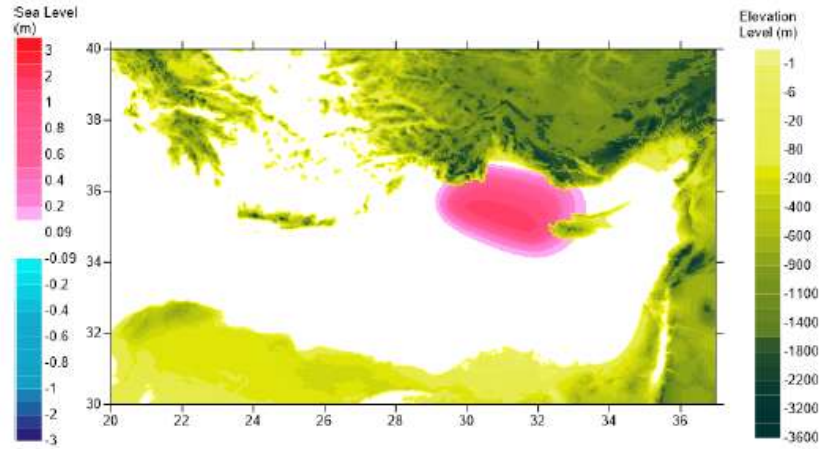


Figure 5.1. Tsunami source used in simulations and bathymetry of the area (Pamuk, 2014).



Figure 5.2. The Study Domain

The bathymetry and topography used in this study is taken from Pamuk (2014). The bathymetry and topography data is extracted from GEBCO (General Bathymetric Chart for the Oceans) and ASTER satellite image. Those are in 926m and 30m resolution respectively. The bathymetry data is enhanced by using the digitized from Navigational Charts. The land data is also enhanced by digitizing the buildings and rivers from satellite image.

In the simulations the maximum current velocity and the maximum flow depth are computed in each grid and then the results are plotted in Figure 5.3 and Figure 5.4 respectively. It can be noted here that the Rouse number values are dependent inversely with the current velocity and flow depth.

The minimum Rouse numbers in each grid during the simulation is computed and the results are presented in Figure 5.5 in the study area. The Figure shows that breaching occurred in the area between the forest and sand spit near the shore. Another is the similarity of the erosion and breaching in Sendai plain Nanakitagawa and Natorigawa rivers mouths by the 2011 Great East Japan Earthquake and Tsunami (Tanaka et al. 2012). Also, trees have been cut off and washed away by the tsunami flow. These notes verify that the numerical results are in fairly well agreement with the observations. Therefore, breaching and erosion can be expected in the low land areas, rivers and their connections to oceans.

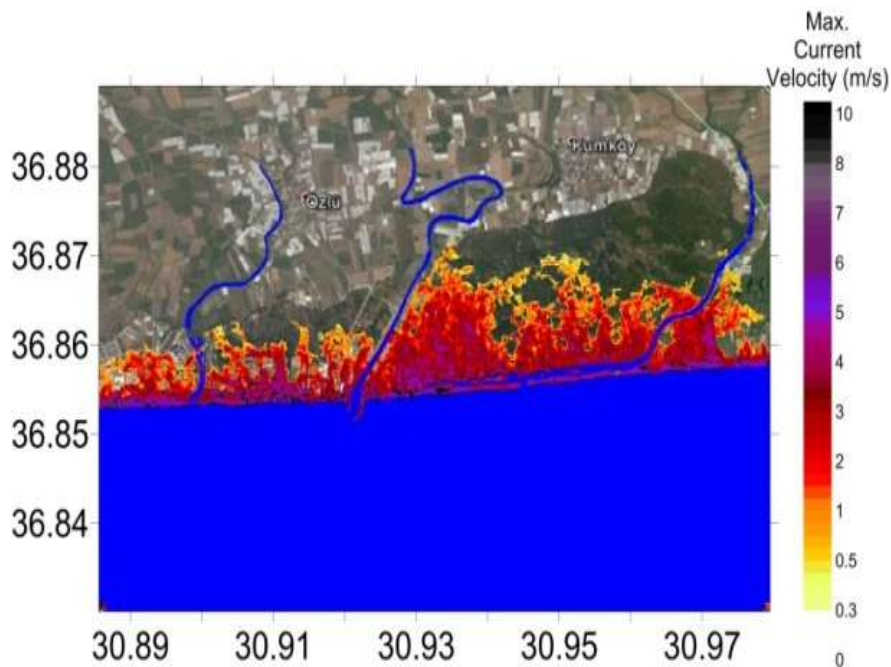


Figure 5.3. Distribution of the maximum current velocity during the 90 min simulation

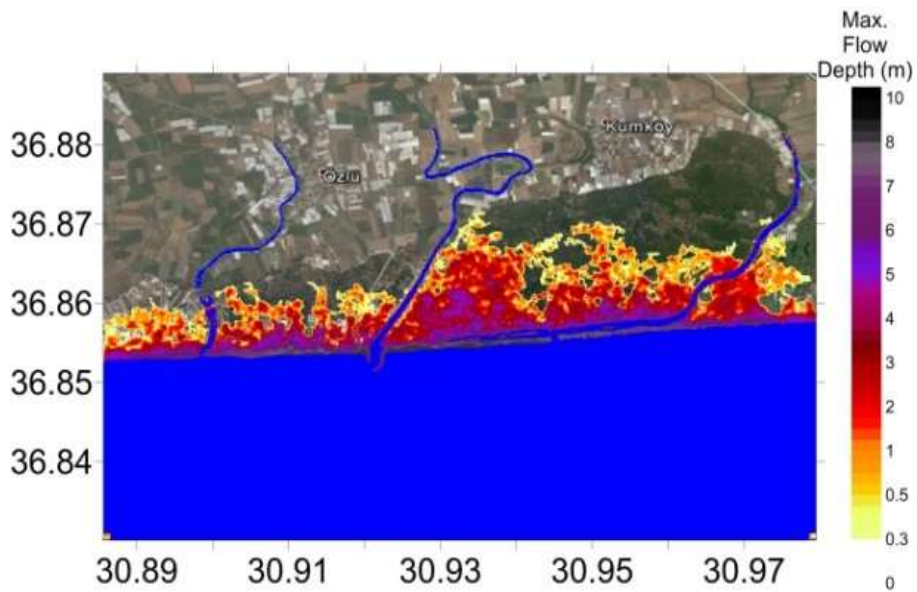


Figure 5.4. Distribution of maximum flow depth during the 90 min simulation

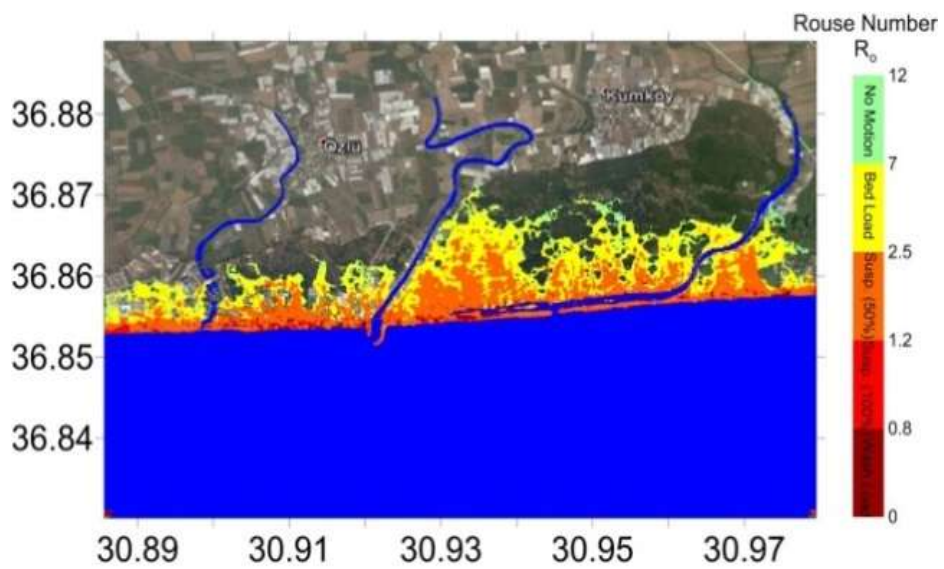


Figure 5.5. Minimum Rouse Numbers in each grid during the simulation

In order to see the sediment transport movements, instantaneous Rouse numbers can be more important rather than minimum Rouse numbers. Since, maximum current

does not occur at the same time in the entire domain. Therefore, some of the instantaneous Rouse numbers are presented in the followings.

First wave that inundates in land comes after 55 minutes later. Figure 5.6. shows the instantaneous Rouse numbers at 55th minute. By looking at this figure, tsunami flow can carry sediments as suspended and wash load in the right and left side of the map. However, in the lagoon and residential area, sediments are transported as bed load or little suspension.

Figure 5.7. shows the instantaneous Rouse numbers at 70th minute. Here, stronger waves attack to the shore and creates more significant sediment transport. In the residential area, due to the channeling effect, wash load is observed which can lead to significant scour around buildings and erosion when the ground material is erodible.

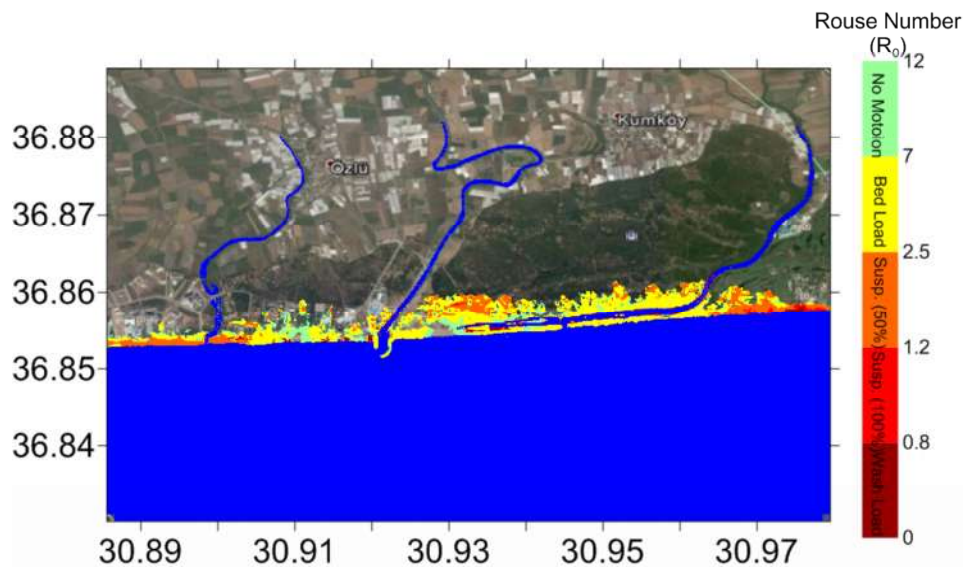


Figure 5.6. Instantaneous Rouse Numbers for 55th minute

Figure 5.8. shows the instantaneous Rouse numbers at 80th minute of the tsunami simulation. At this instant, backflow occurs. Strong backflow causes significant suspension in the lagoon area.

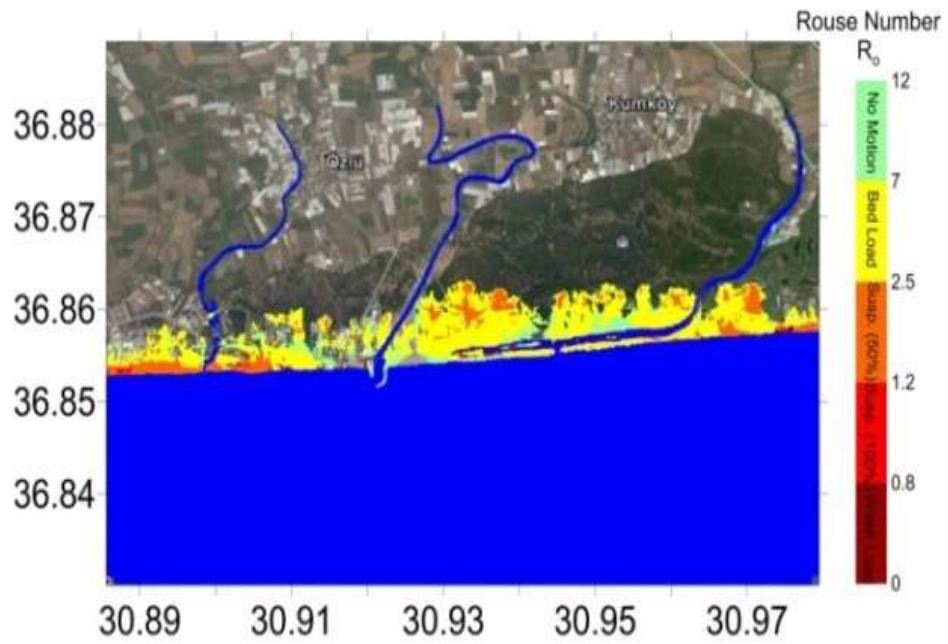


Figure 5.7. Instantaneous Rouse Numbers for 70th minute

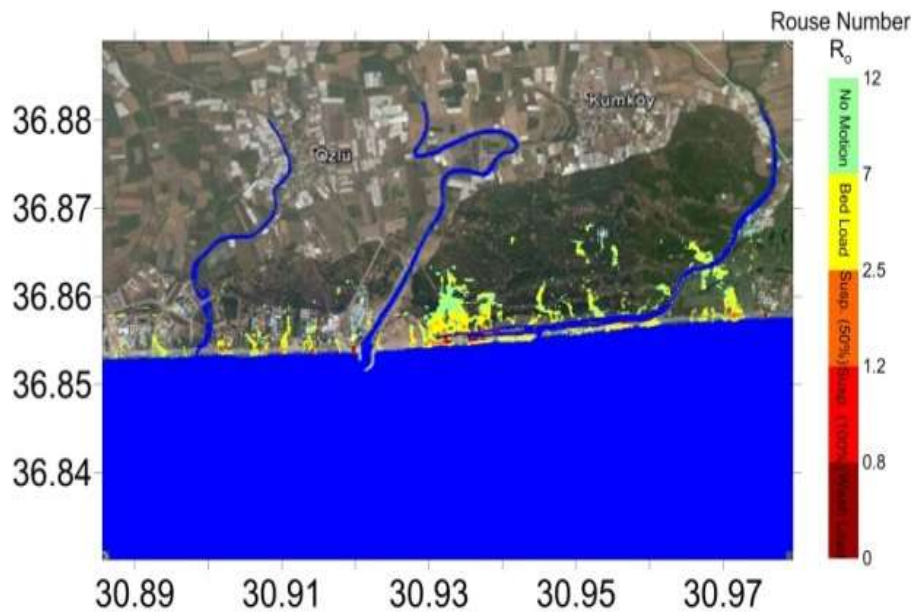


Figure 5.8. Instantaneous Rouse Numbers for 80th minute

At the same time the stronger currents are observed in the residential area. Probably, the eroded sand is moved to inland by advancing (incoming) wave or to the sea by

the strong return flow. Because of these movements the changes in the shoreline position can also be expected.

The temporal variations of water level, flow depth and Rouse number. At selected 12 (A, B, C, D, E, F, G, H, I, J, K and L) numerical gauge locations are plotted and discussed. Hence the time histories of water surface elevation (m), current velocity (m/s) and flow depth (m) and Rouse number are plotted in Figure 5.9 to Figure 5.20 respectively for 90 minutes of simulation.

Figure 5.9 (a-d) shows the bathymetry and selected gauge point, the time history of water surface elevation, flow depth, current velocity and the Rouse Number in Gauge A. The current velocity in this gauge point which is tangent to the shoreline is increasing during the time, therefore, the Rouse number is decreasing. Hence the sediment motion is mostly in the form of suspended load, but it is approaching to the wash load form after 60mins. As we expect, the pattern of the flow depth and the current velocity graphs are similar.

The current velocity and therefore, the flow depth in Gauge B (Figure 5.10), near the shoreline, are not large enough to cause higher rate of sediment motion during the simulation. Hence the Rouse number is changing in the range of 2.5 to 7 and the sedimentation is mostly in the form of bed load. However, very shortly between 65min and 75min the sediment moves the form of suspended load because the current accelerates very temporarily in that range.

In Gauge C (Figure 5.11) which is tangent to the shoreline similar to the Gauge A, the flow depth and current velocity are increasing during the simulation time, hence, the Rouse number is decreasing permanently. After 40mins the sediment motion is in the form of wash load in this gauge which means that erosion take place in this point after 40mins. The condition in Gauge C is similar to Gauge A, the only difference is that the Gauge C is closer to the river mouth and the morphology changes are more sever in comparison to the Gauge A.

In Gauge D (Figure 5.12) which its position is similar to Gauge B, the flow depth and current velocity are small and lead to accretion of sediments in that region. Hence the Rouse number is changing in the range of 2.5 to 7 and the sedimentation is mostly in the form of bed load. However, very shortly between 64min and 72min the sediment moves the form of suspended load because the current accelerates very temporarily in that range.

In the mouth of the river, Gauge E (Figure 5.13), the current velocity and flow depth are both increasing during time, as a result, Rouse number is decreasing simultaneously to become smaller than 0.8 after 25mins simulation. It means that the sediment movement after 25min in the river mouth is wash load.

The condition in Gauge F (Figure 5.14), tangent to the shoreline and near the river mouth is similar to condition in Gauge E. But the sedimentation pattern is mostly in suspended load form. In Gauge E after 40min the sediment move like wash loads but in Gauge F, the sedimentation after 40mins is suspended load.

Figure 5.15 represents the increasing manner of flow depth and current velocity and decreasing manner of Rouse number in Gauge G during the simulation. In this gauge point, in the first 20 minutes of simulation the sediments motion are in bed load form, in the second 20 minutes, the pattern of sediment motion is in suspended load form, and after 40 minutes, sediment move very fast in the form of wash load. Hence we can conclude that the sediment motion in this point tend to be in wash load form after 40mins.

The sediment motion in the Gauge H (Figure 5.16) is mostly suspended load in the time range of 25-90 minutes. In the first 25mins the sediments move like bed loads. Although the current velocity is increasing during the time but due to the distance of this point from the shoreline, the sediment does not move in wash load form.

Figure 5.17 shows the increasing manner of flow depth and current velocity and decreasing manner of Rouse number in Gauge I (in the river mouth) during the simulation. In this gauge point, in the first 25 minutes of simulation the sediments motion are in bed load form, between 25 and 60 minutes, the pattern of sediment motion is in suspended load form, and after 60 minutes, sediment move very fast in the form of wash load. Hence we can conclude that the sediment motion in this point tend to be in wash load form after 60mins.

Gauge J (Figure 5.18) has a similar location to the Gauge A and Gauge C which are lying on the shoreline. Increasing current velocity leads to a stable mode of sediment motion after 40mins which is in wash load form. In the first 20mins sediment move in bed load form then between 20 and 40mins the sediment movement pattern changes to the suspended load form.

Gauge K and Gauge L in Figure 5.19 and Figure 5.20 respectively; show that far from the shoreline and the river mouth with small current velocity and flow depth, Rouse number would be larger. Therefore, in these two points the Rouse number in greater than 0.8 and the sediment motion is mostly in bed load form.

Locations of gauges are presented in Figure 5.9 to Figure 5.20. Gauge G is in front of the residential area. Gauge H is between buildings and Gauge L is in the forest area. These gauges are located in land at the ground elevation 6.17m at Gauge H, 3.4m at Gauge G and 4.2m at Gauge L. The discharge fluxes are observed as different at both residential area (Gauge G and H) and non-residential area (Gauge L). In the Gauge H (between the buildings), channel effect may be expected. However, buildings are distributed randomly in the region. Therefore, no channel effect is observed in Gauge H. Gauge G gives higher discharge flux difference for constant roughness model up to 80 percent.

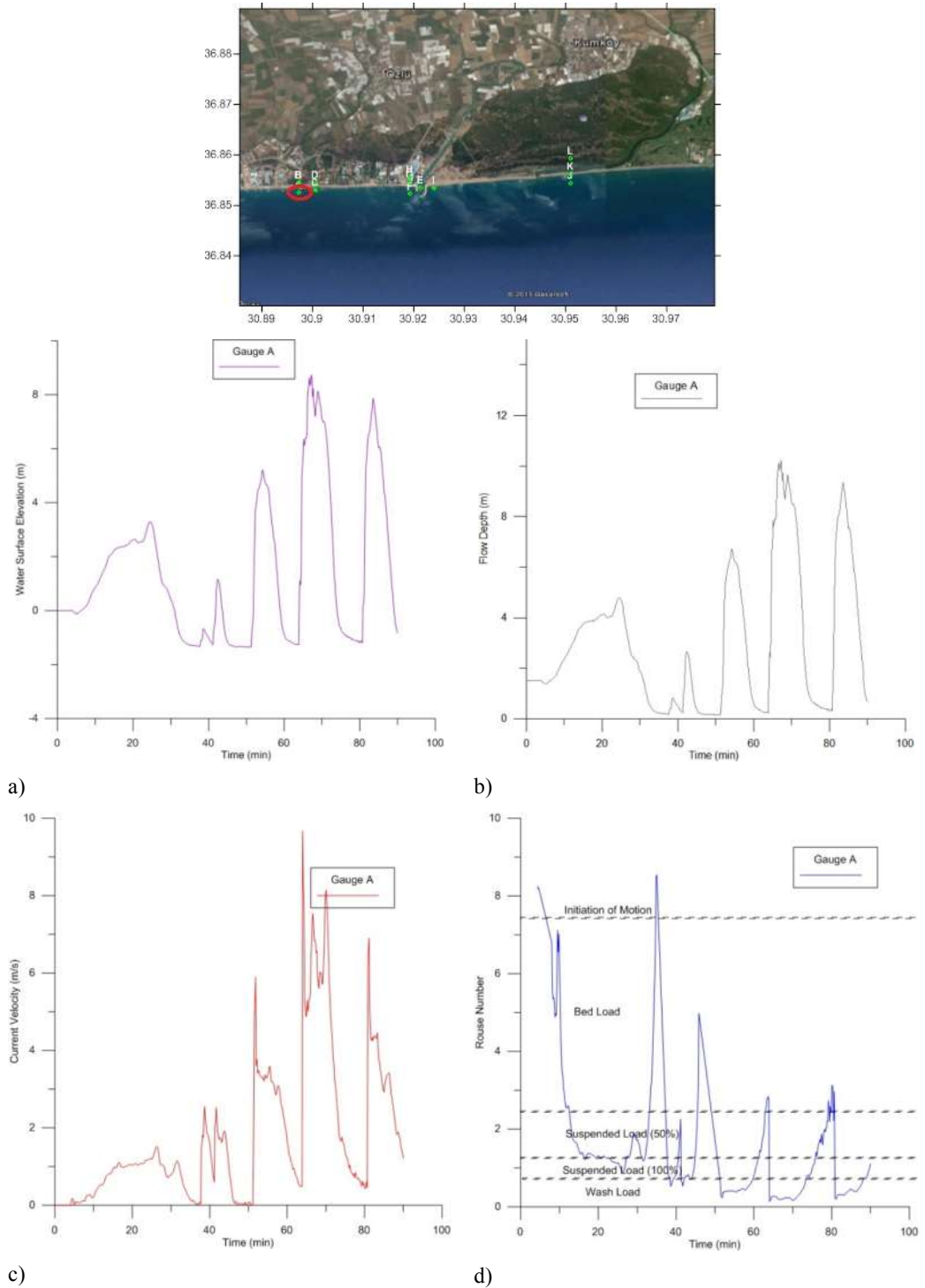


Figure 5.9. The bathymetry and the gauge points used in the simulations in Belek region in Antalya, a) time history of water surface elevation, b) time history of low depth, c) time history of current velocity d) time history of Rouse number during 90min simulation in Gauge A.

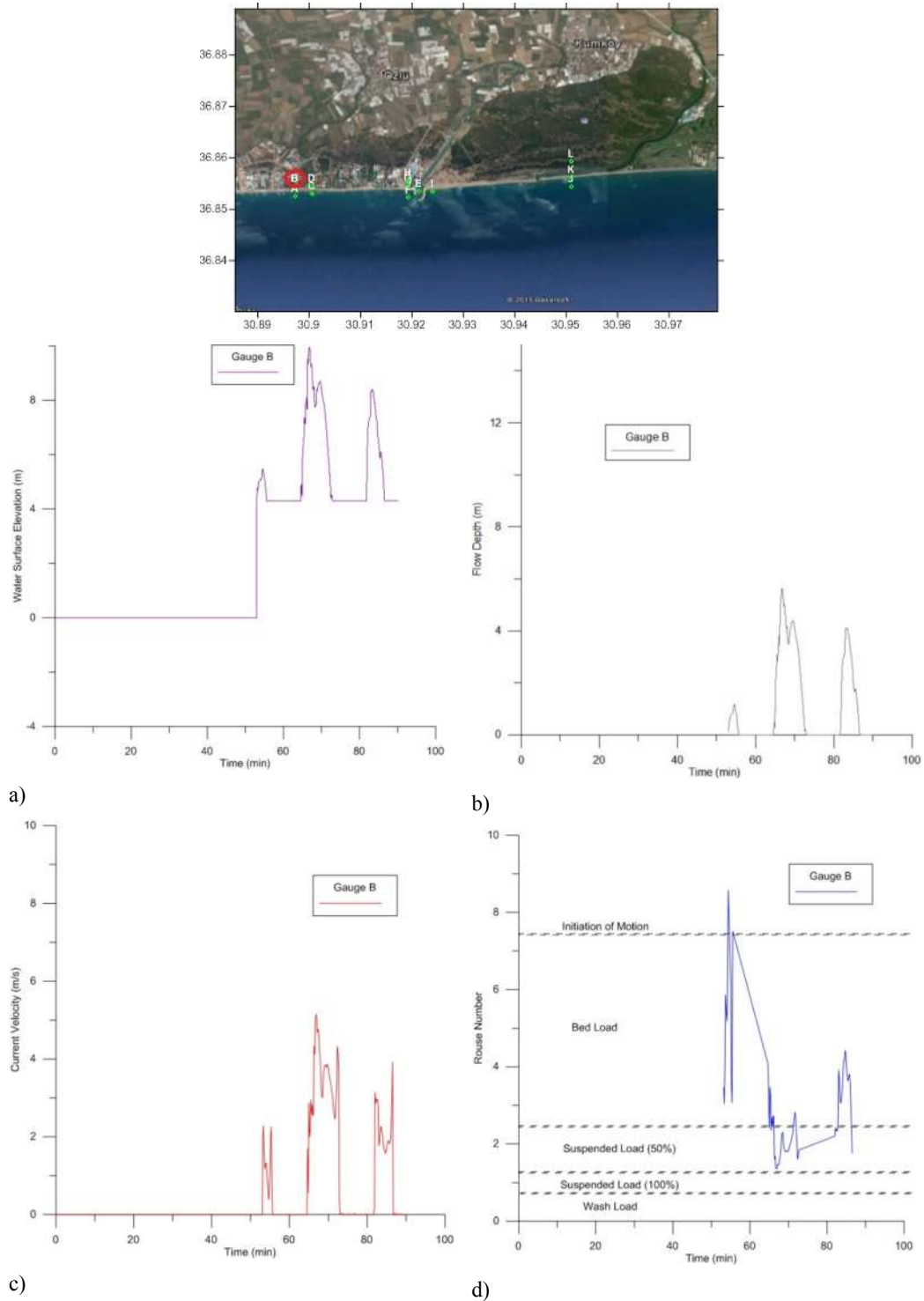


Figure. 5.10. The bathymetry and the gauge points used in the simulations in Belek region in Antalya, a) time history of water surface elevation, b) time history of low depth, c) time history of current velocity d) time history of Rouse number during 90min simulation in Gauge B.

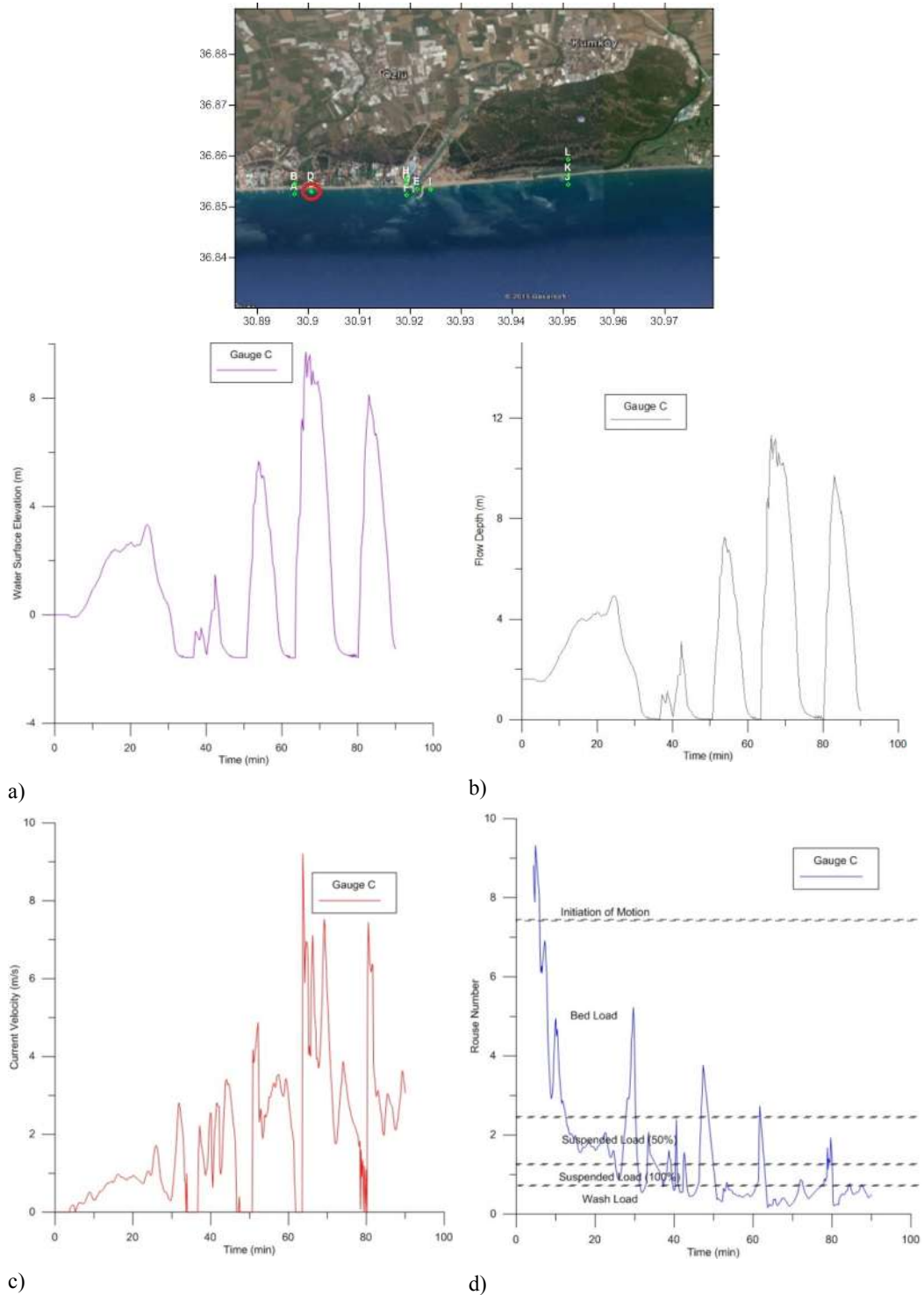


Figure 5.11. The bathymetry and the gauge points used in the simulations in Belek region in Antalya, a) time history of water surface elevation, b) time history of low depth, c) time history of current velocity d) time history of Rouse number during 90min simulation in Gauge C.

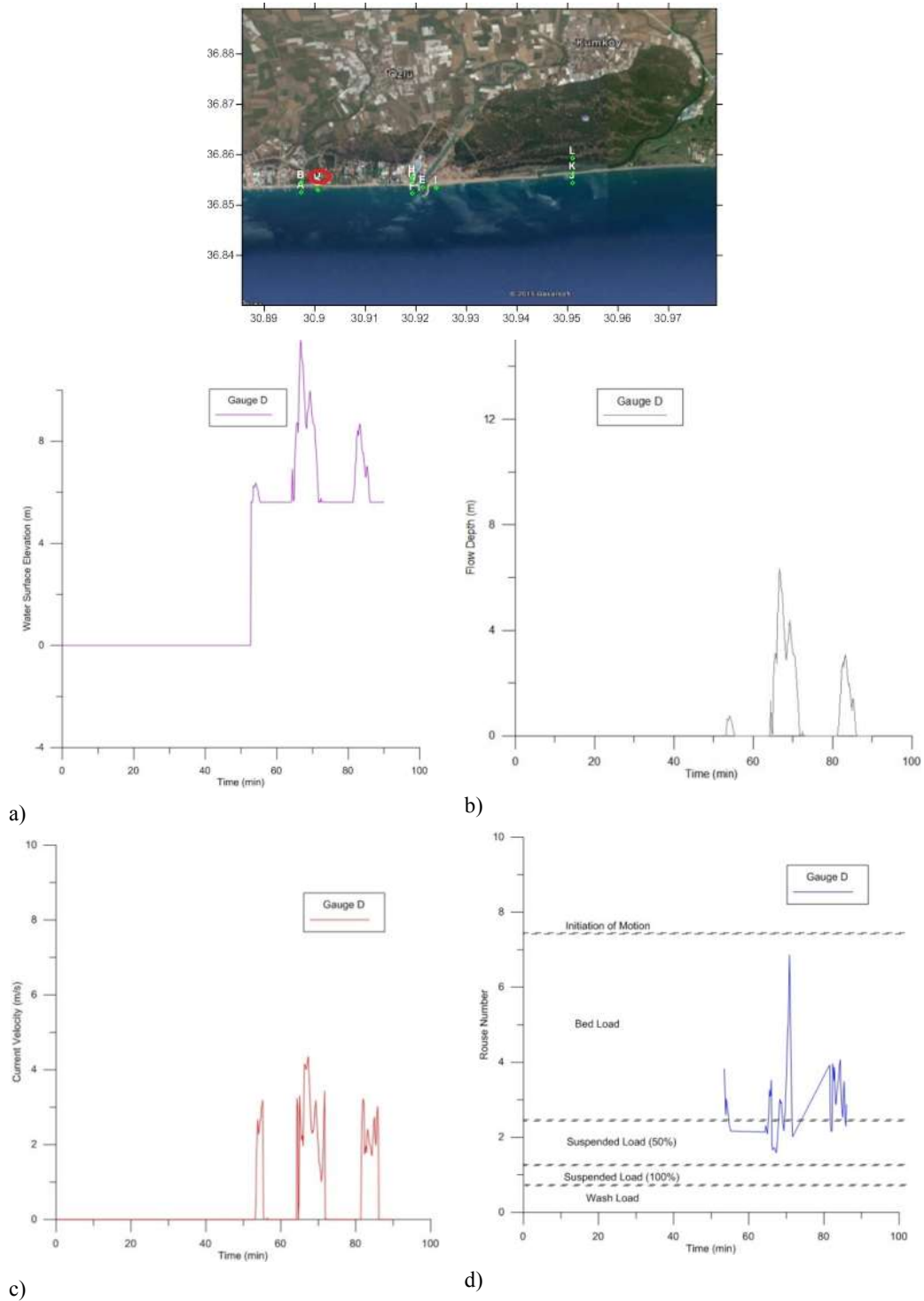


Figure. 5.12. The bathymetry and the gauge points used in the simulations in Belek region in Antalya, a) time history of water surface elevation, b) time history of low depth, c) time history of current velocity d) time history of Rouse number during 90min simulation in Gauge D.

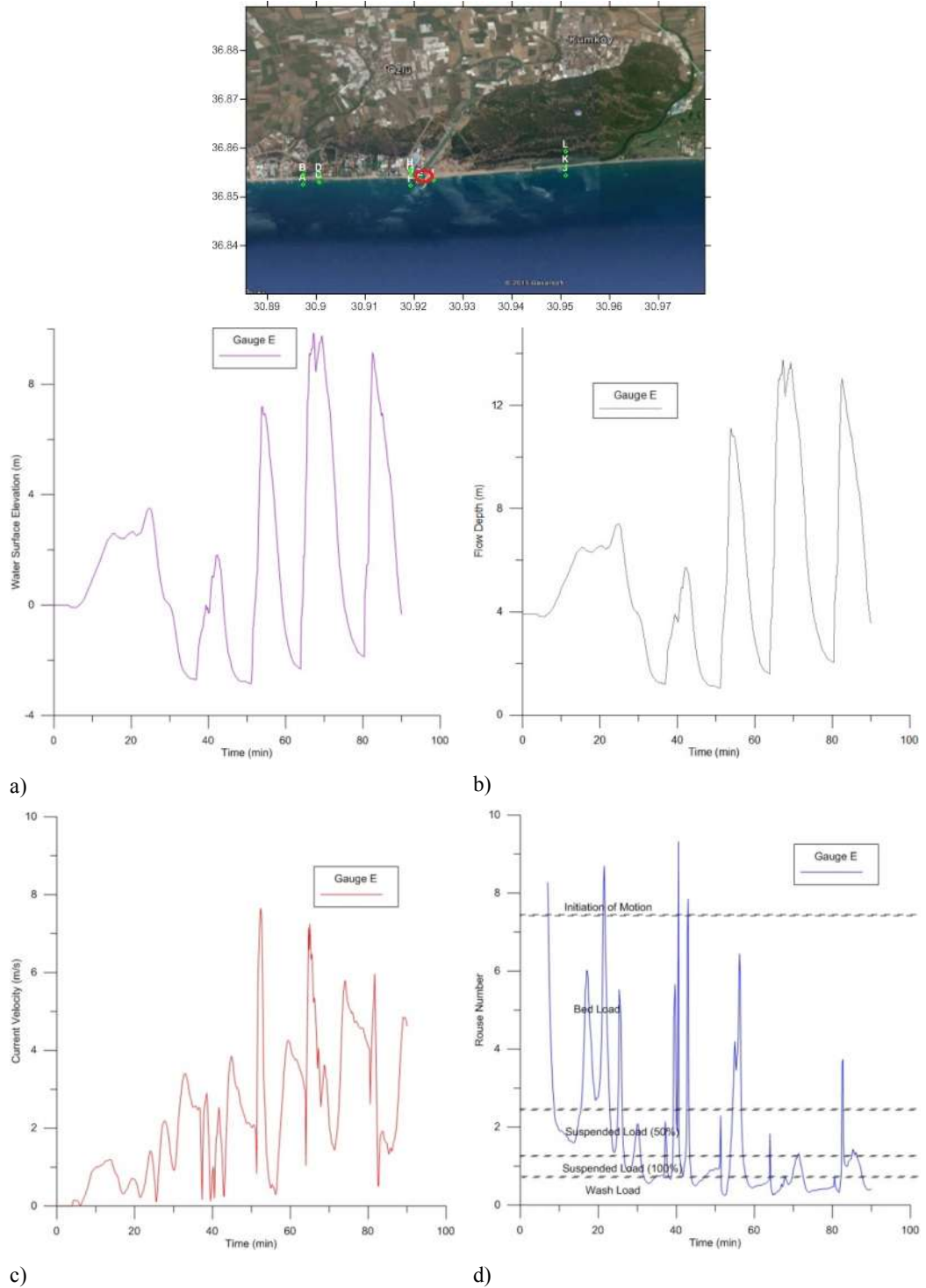


Figure. 5.13. The bathymetry and the gauge points used in the simulations in Belek region in Antalya, a) time history of water surface elevation, b) time history of low depth, c) time history of current velocity d) time history of Rouse number during 90min simulation in Gauge E.

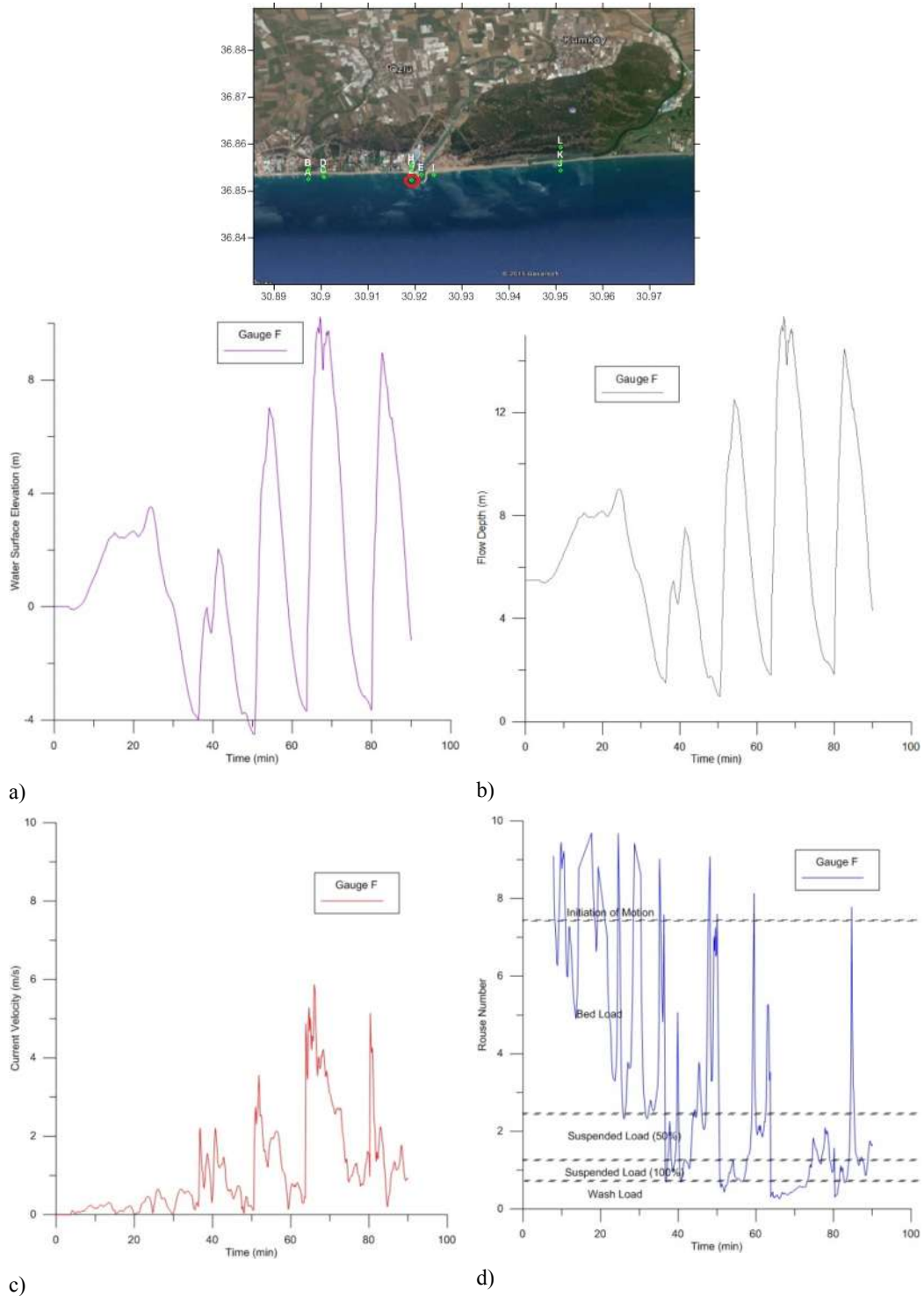


Figure. 5.14. The bathymetry and the gauge points used in the simulations in Belek region in Antalya, a) time history of water surface elevation, b) time history of low depth, c) time history of current velocity d) time history of Rouse number during 90min simulation in Gauge F.

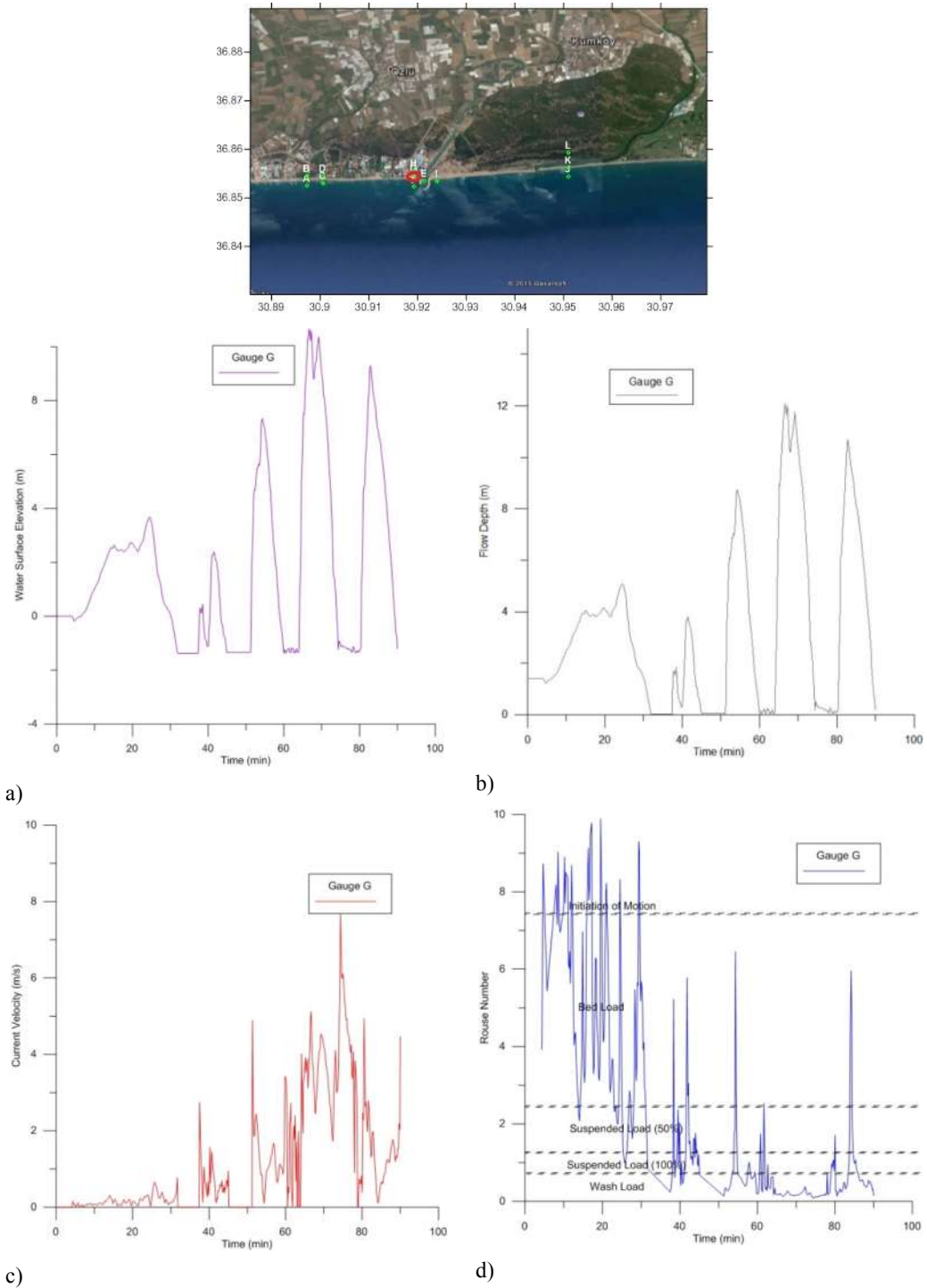


Figure 5.15. The bathymetry and the gauge points used in the simulations in Belek region in Antalya, a) time history of water surface elevation, b) time history of low depth, c) time history of current velocity d) time history of Rouse number during 90min simulation in Gauge G.

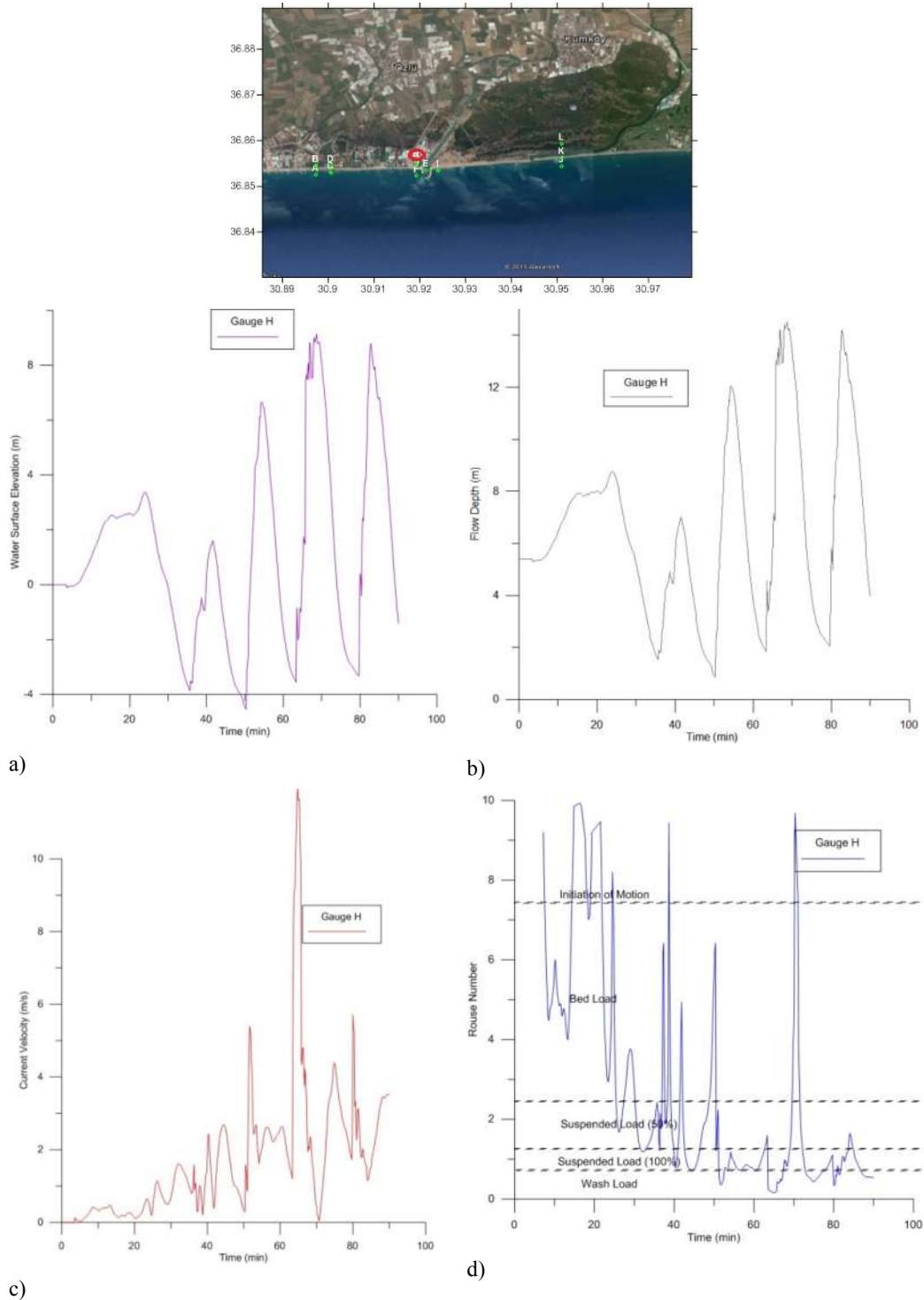


Figure 5.16. The bathymetry and the gauge points used in the simulations in Belek region in Antalya, a) time history of water surface elevation, b) time history of low depth, c) time history of current velocity d) time history of Rouse number during 90min simulation in Gauge H.

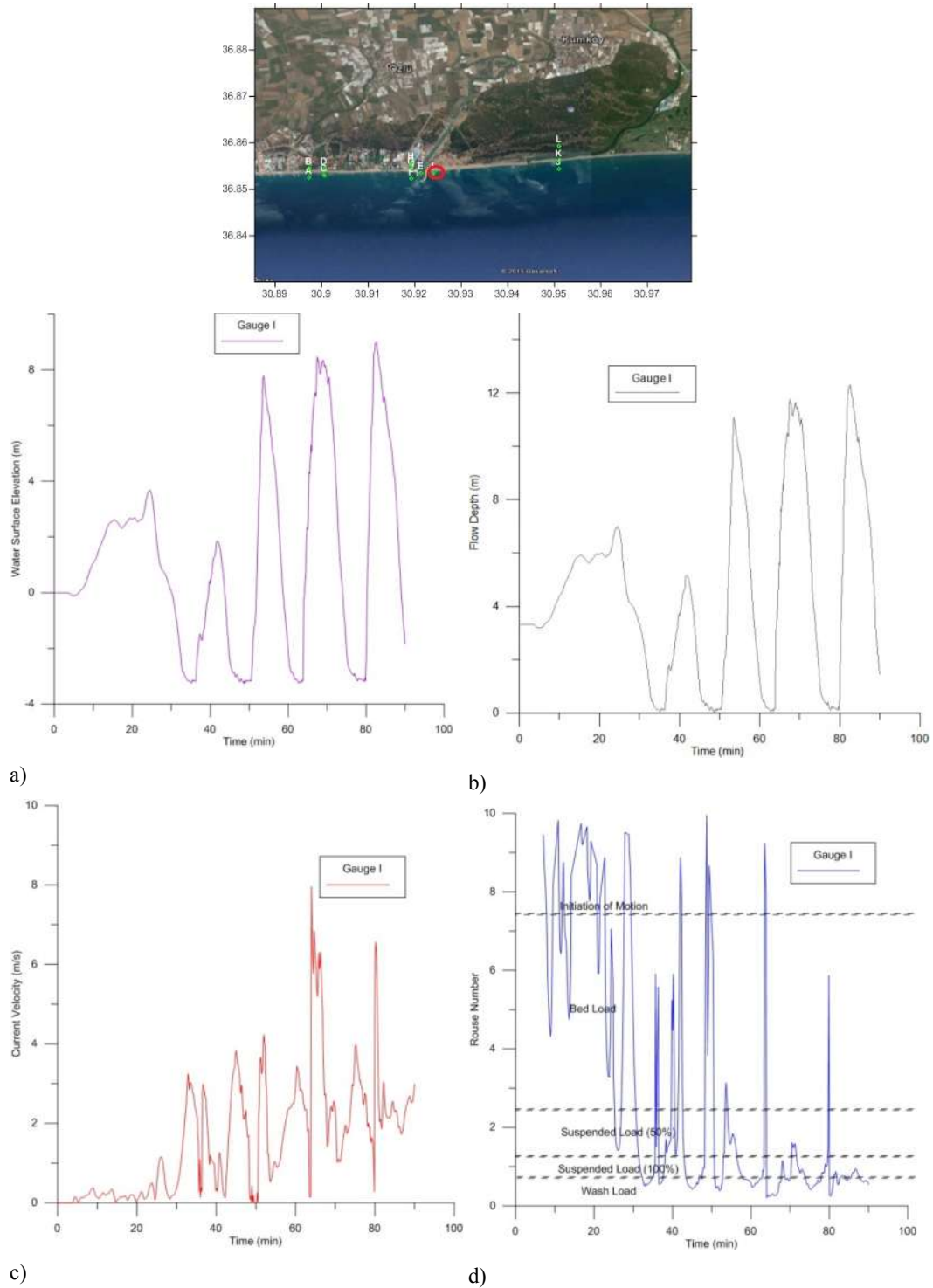


Figure. 5.17. The bathymetry and the gauge points used in the simulations in Belek region in Antalya, a) time history of water surface elevation, b) time history of low depth, c) time history of current velocity d) time history of Rouse number during 90min simulation in Gauge I.

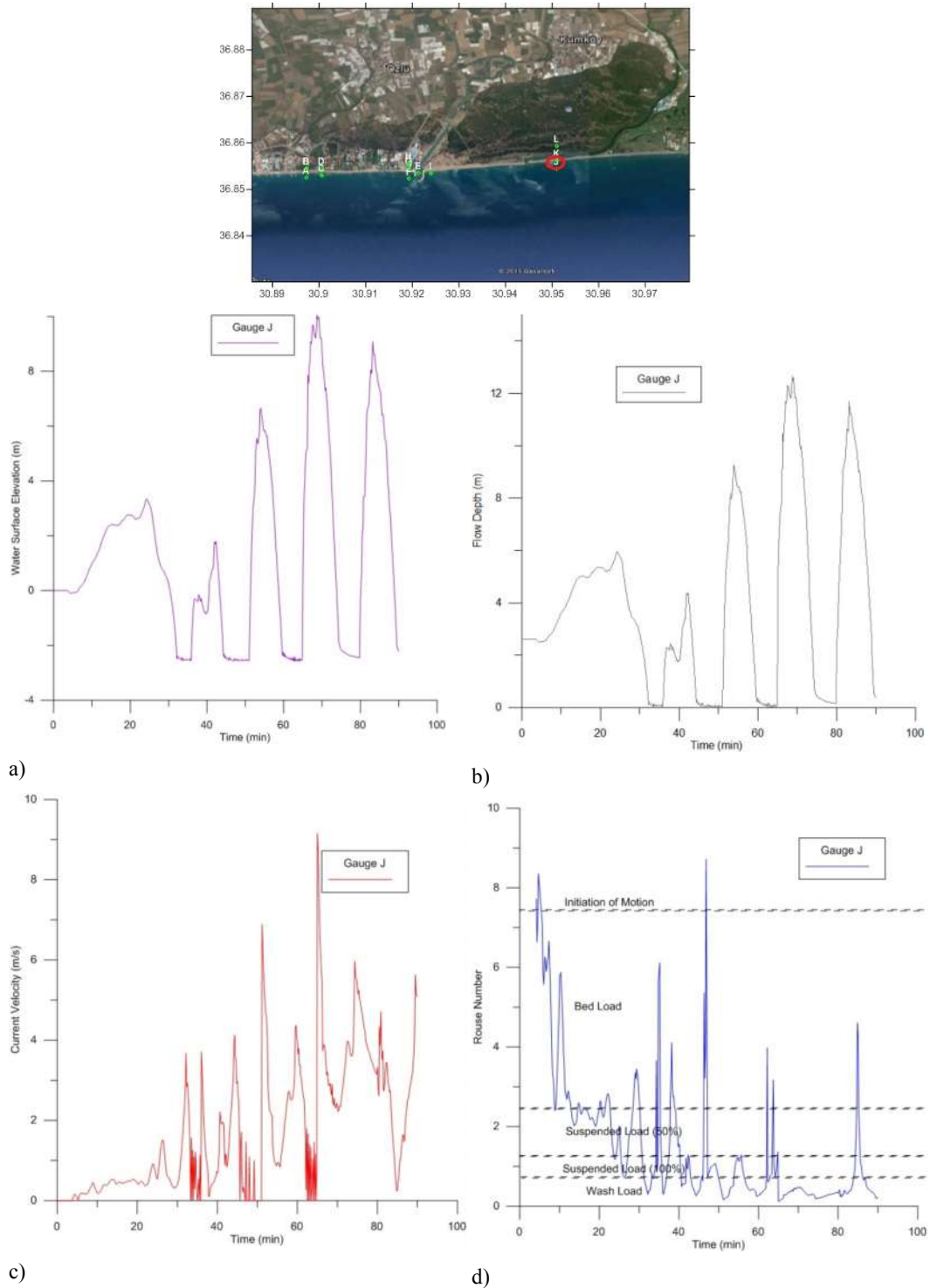


Figure. 5.18. The bathymetry and the gauge points used in the simulations in Belek region in Antalya, a) time history of water surface elevation, b) time history of low depth, c) time history of current velocity d) time history of Rouse number during 90min simulation in Gauge J.

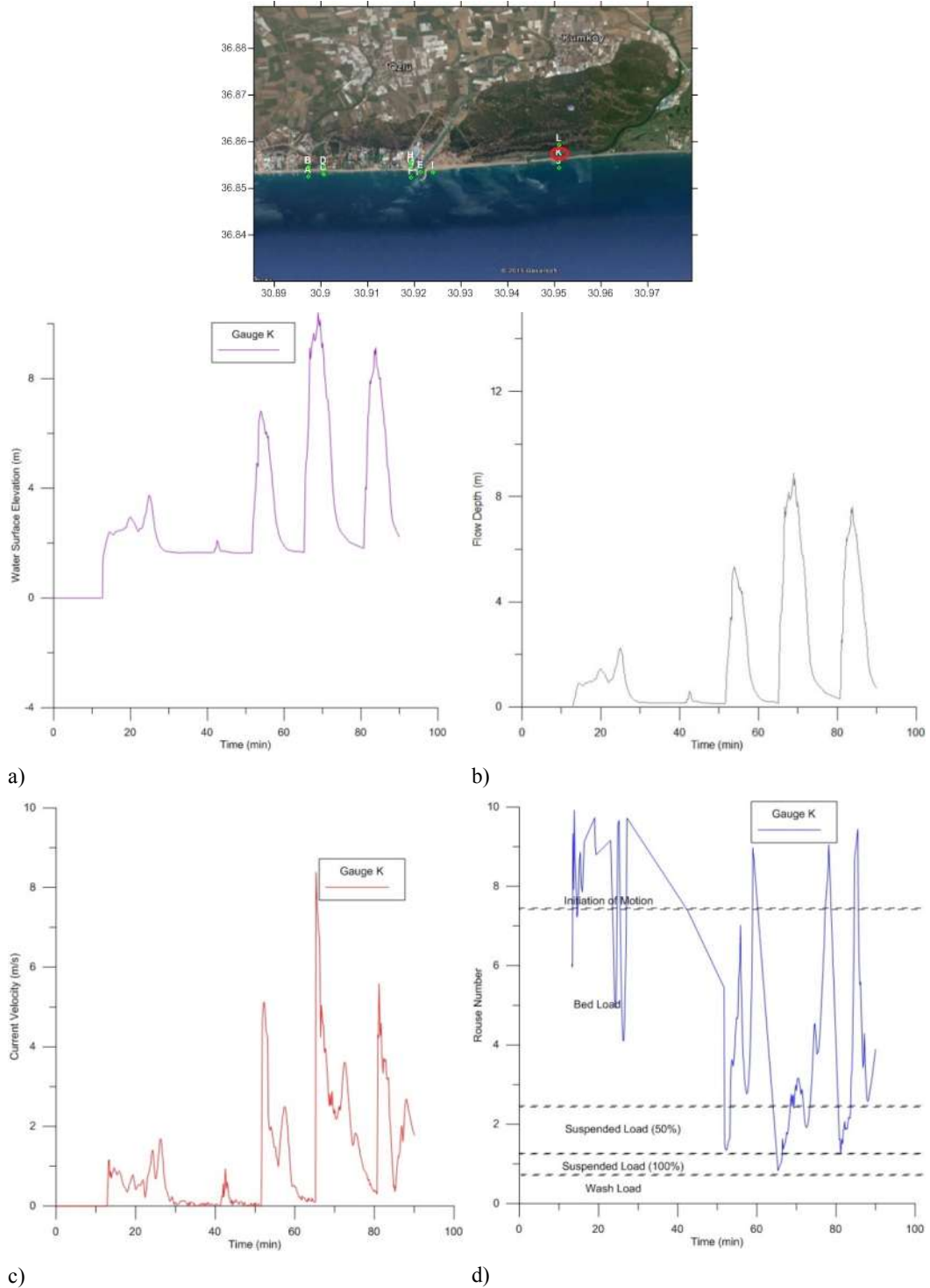


Figure. 5.19. The bathymetry and the gauge points used in the simulations in Belek region in Antalya, a) time history of water surface elevation, b) time history of flow depth, c) time history of current velocity d) time history of Rouse number during 90min simulation in Gauge K.

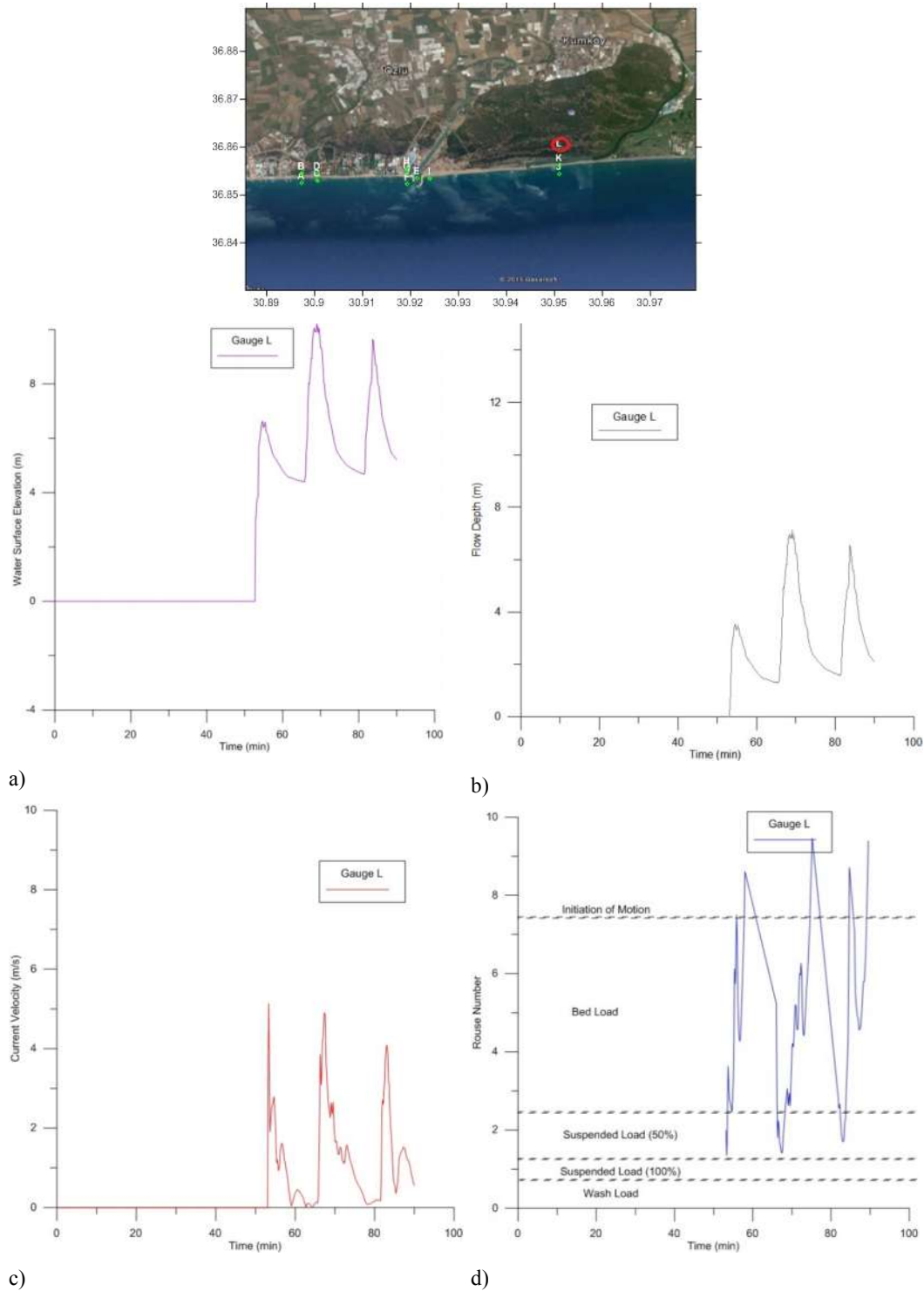


Figure. 5.20. The bathymetry and the gauge points used in the simulations in Belek region in Antalya, a) time history of water surface elevation, b) time history of low depth, c) time history of current velocity d) time history of Rouse number during 90min simulation in Gauge L.

Discussion and Remarks

The general information together with the literature survey is presented to identify the morphological changes due to tsunami inundation. A methodology based on computation of instantaneous Rouse number during tsunami simulation is presented. As a case study a simulation is performed according to a selected tsunami scenario in Eastern Mediterranean basin attacking to Belek region at East of Antalya province South of Turkey (Pamuk, 2014). The computed time histories of water level, current velocity, flow depth and Rouse number change at the border of the study domain is inputted as the triggering wave to the study domain. The aim is to investigate the tsunami motion and calculate the respective sediment movement by computing the spatial and temporal change of Rouse number under tsunami inundation according to the approach given in Yeh et al. (2008). The spatial distribution of sediment properties (diameter, fall velocity and density) is used and a sediment property matrix is developed for the computation of Rouse Number. The instantaneous current velocities at every grid point are used to compute the instantaneous Rouse number from sediment property matrix at each time step during simulation. But Pamuk (2014) calculated the value of sediment property equal to 3.1509 for each grid. However using the sediment property matrix to calculate the Rouse Number in Antalya does not affect the results considerably in comparison to the case of using a constant value for whole the domain.

According to the results of simulations, it is observed that the approach using Rouse number to investigate sediment movement is reasonable if the data is sufficiently accurate. The results showed that the bed material near the shore will certainly move under any tsunami action since the sediment diameter of bed material is small and the current speed of water is high at shallow and near shore regions. The movement of bed material is also observed far distances from the shore at the low areas and river beds at Belek Region. Along with the sediment property matrix, the friction matrix (representing friction coefficients at every grid location) may be helpful to achieve more accurate results of current and other parameters in simulations.

The similar research was studied by Pamuk (2014) in the same region. The aim of re-modeling of some of Pamuk (2014) simulations in this thesis are; To check performance of the module of NAMI DANCE which was added to calculate the Rouse number directly as the model output; To investigate the effect of applying sediment property matrix on the Rouse number results; To obtain time history of Rouse number in certain gauges during the simulation. The achieved Rouse number values show that using friction matrix or sediment property matrix in Belek region does not change the results sensible.

Therefore a method to follow the morphological change under tsunami motion is developed by using the temporal change of Rouse number. Using Rouse number as a controlling parameter may reasonably predict the level of morphological changes in the study region. The results for Belek region show that near the shoreline, the sediment movement is mostly in the form of wash load.

When going towards the land, the sediment movement dependent on the current velocity and Rouse number value turns to the form of suspended load or bed load or even no motion according to the Rouse number. Hence, we can generally conclude that the erosion in shorelines and accretion far from the shorelines are dependent on the mentioned criteria in this study. Results obtained from this study emphasize that even if the flow depth and current velocity are large, the sediment motion would not be in the wash load form if the region is far from the shoreline.

CHAPTER 6

SEDIMENTATION AND RESONANCE IN HARBORS; A CASE STUDY IN HAYDARPASA HARBOR

Verification of the model used in this thesis is investigated in chapter 3 by remodeling of some tests for resonance performance of rectangular shaped basins (Yalciner and Penilovsky, 2007), chapter 4 by modeling L-Type basins and their sedimentation and amplification behaviour, and then simulating the Antalya region for sediment motions. In this chapter Haydarpaşa port is selected to study about sediment motions and resonance effects.

This chapter describes the harbor damage and harbor resonance and sediment motion due to tsunami and shows the resonance periods, wave and current amplifications and morphological changes in Haydarpasa port in Marmara Sea as a case study. It calculates the resonance periods and current velocity and momentum fluxes and Rouse Number in the harbor using the numerical model NAMI DANCE. The key objective of this chapter is to obtain the spatial and temporal changes of main tsunami parameters and their adverse effects on Haydarpasa harbor performance by analysing the critical tsunami parameters (water elevation, current speed, and momentum fluxes) in the port.

Anatolia is surrounded by Aegean, Mediterranean, Black and Marmara Seas and has been exposed to several natural disasters. The Sea of Marmara is an inland sea and its coasts have been attacked and impacted by more than 30 tsunamis in history for two millenniums. The highest populated mega city Istanbul, located at north coast of

the Sea of Marmara is one of the main centers of all economic activities in Turkey. There are numerous ports in Istanbul and those are in different sizes serving different activities from commercial to leisure purposes. One of the main ports in the Sea of Marmara is Haydarpaşa port which serves not only cargo but also passenger transportation. Resonance oscillations and resultant wave amplifications inside the basins are other important adverse effects which cause damage on structures and interruption of harbor functions (Kian et al., 2015a; Yalciner et al., 2015).

The Haydarpaşa port (29.01E, 41N) is Turkey's third biggest port and located at southern entrance of Bosphorus in Istanbul (Figure 6.1). It is an important cargo port, terminal for ro-ro containers and passengers. This port serves the most industrialized and economized region of Turkey. There are two breakwaters with 3km length in total. The annual handling capacity of the Port is 144,000 twenty-foot equivalent units (TEU). In addition to the open storage area of 313,000 m² and covered area of 21,000 m², there exists a container land terminal outside the port in Göztepe district of Istanbul for stocking the empty containers which covers a holding capacity of 52,800 TEU. The total annual cargo volume in the area exceeds six million metric tons (MT). The motion of long waves inside the Haydarpaşa port and the amplification of water level and current speed are investigated by using numerical tools NAMI DANCE. The resonance oscillations, periods of free oscillations and flow pattern of long waves and morphological changes in Haydarpaşa port under the actions of long waves are investigated using numerical model (NAMI DANCE). The details of numerical modeling tool are given in the following together with the results and discussions (Yalciner et al., 2007; Kian et al., 2015a, b).

In order to compute the period of the basin an initial impulse is inputted, and a simulation is performed. The time histories of water surface fluctuations are computed at several numerical gauge points inside the harbor. The spectral analysis by using Fast Fourier Transform technique is applied to the records of all numerical gauge points and respective spectrum curves are obtained. The peaks of spectrum curves of each numerical gauge location are also determined. The peaks of spectrum

curves coincide with the resonance frequencies. The computed frequencies are discussed by comparing with the frequency of the waves which occur in the Marmara Sea in regard to their possible amplification and effects to Haydarpaşa port.



Figure. 6.1 Haydarpaşa Harbor in Istanbul

The simulations in Haydarpaşa port are performed by inputting different impulses inside the port and the motion of the wave, amplification of the water level and current velocities are monitored. In the simulations, the computational domain is selected to be bounded between 28.995E and 29.025E in E-W direction and 40.987N and 41.015N in S-N direction which covers 2km in S-N direction and 1.6km in E-W direction of Haydarpaşa port. The bathymetry is obtained from GEBCO with 30sec resolution in deep sea carefully enhanced by digitization of the navigational charts inside and nearby the port. The numerical grid size is used as 2.4m and the time step is selected as 0.005s for a 60min real time simulation of any impulse inside the harbor. The amplification of water level and current speed are monitored by storing the time series of water level and current speed at 47 gauge points with especial focus on eight numerical gauge points located at the corners or sides of a

rhombohedral shape of a basin inside the port and three of them outside the rhombohedral shaped basin in the corners and then using them for spectrum analysis.

6.1. Source input

Four different impulses are applied to Haydarpasa Port in three different simulations to calculate the period of free oscillations in Haydarpasa port. Those impulses are a) dome shape circular static source with 5m wave amplitude and 80m diameter in the centre of rhombohedral shape basin (R1), b) dome shape circular static source with 5m wave amplitude and 80m diameter out of the rhombohedral shape basin (R2) c) E-W direction, line crested sinusoidal shape time dependent (dynamic) 10 sec period impulse with 1m wave amplitude (R3), d) S-N direction line crested sinusoidal shape time dependent (dynamic) 10 sec period impulse with 1m wave amplitude (R4). The locations of these impulses and the selected numerical gauge locations (1-4) are shown in Figure 6.2. Time history of wave propagation for (R1) is shown in Figure 6.3.

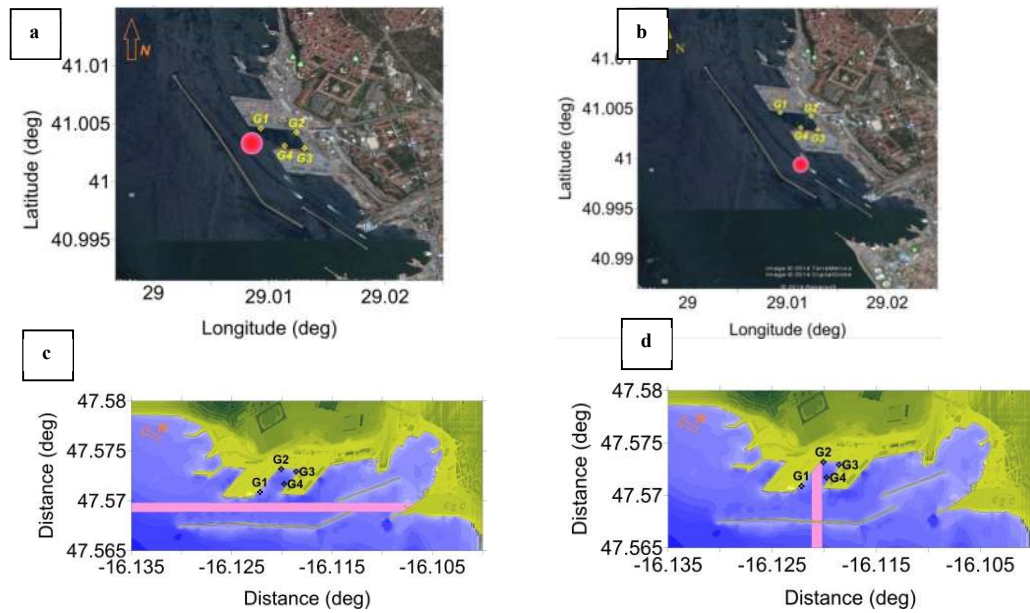


Figure. 6.2. The location of impulse a) dome shaped source inside the rhombohedral shape basin (R1), b) dome shaped source outside the rhombohedral shape basin (R2), c) sinusoidal line source parallel to the main breakwater (R3), d) sinusoidal line source perpendicular to the main breakwater (R4), at numerical gauge locations G1, G2, G3, G4.

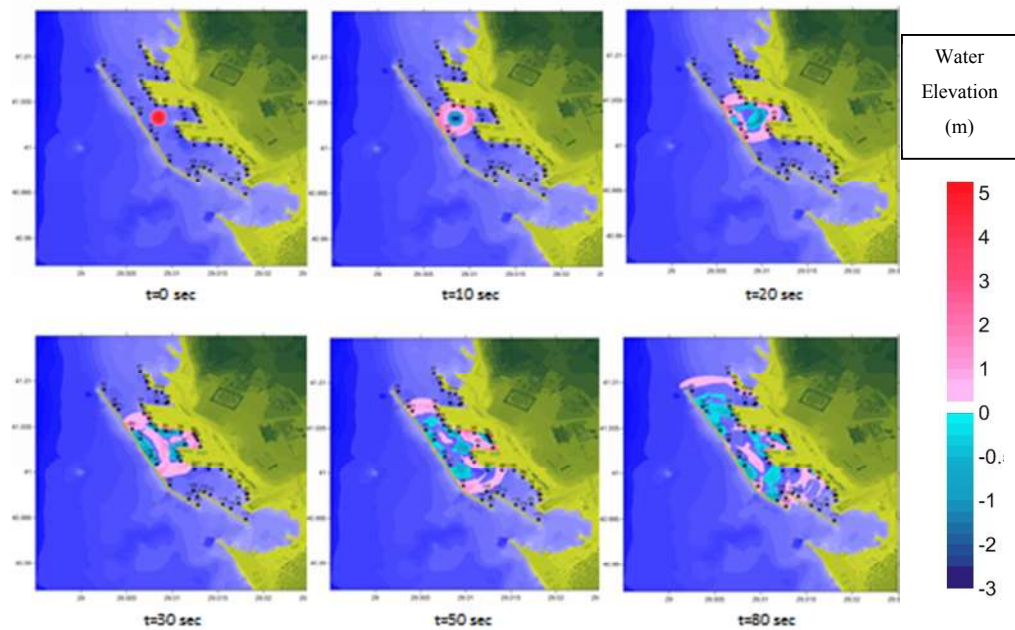


Figure. 6.3. Dome shaped wave (5m amplitude) propagation as time history in a) $t = 0$, b) $t = 10$ s, c) $t = 30$ s, c) $t = 60$ s by the simulation (R1) of dome shaped inside the rhombohedral shape basin.

6.2. Simulations:

In order to determine the level of tsunami hazard and measure the level of the resilience of the study area, it is important to compute and evaluate the effects of main tsunami hydrodynamic parameters in shallow zone and at land. Among important parameters mentioned former, the spatial distribution of maximum water elevation, maximum current velocity, and the momentum flux computed by the simulations. Figure 6.4 shows the results for simulation results with R1 source and Figure 6.5 for R2 source input.

The time history of wave propagation for (R3) is shown in Figure 6.6 and for (R4) in Figure 6.7. The spatial distribution of maximum water elevation, maximum current velocity, and the momentum flux for (R3) and (R4) are shown in Figure 6.8 and Figure 6.9 respectively. It is seen from Figure 6.4 (a-b) and Figure 6.8 (a-b) and Figure 6.9 (a-b) that the highest amplifications of maximum water elevations, current velocities and momentum fluxes occur at the concave (G2, G3 and G6) and convex (G1, G4 and G5) corners comparing to other locations inside the inner rhombohedral shaped basin of the port.

As it is expected, Figure 6.5 (a-b) shows that in R2 cases, G6 shows more amplification for wave amplitude and current waves. Also the gauges in the inner rhombohedral shaped basin have large amount of wave amplitude and current velocity values in R1 case. But the gauges outside the rhombohedral shaped basin show larger values in R2 case simulation which is expected.

It is clear from Figure 6.4.b, Figure 6.5.b, Figure 6.8.b and Figure 6.9.b that the harbor entrance between two breakwaters is a critical region for current velocity due to the channeling behavior of the area in the harbor entrance part. Figure 6.4.c, Figure 6.5.c, Figure 6.8.c and Figure 6.9.c show that the momentum flux which is dependent on the mass of water is spread entirely uniform in the basin as it is expected.

Figure 6.10 shows the time histories of the water levels and Figure 6.11 shows the time histories of the current velocities at numerical gauge locations 1-8 computed by

the simulations (R1, R2, R3 and R4). It is seen from Figure 6.10 that the water level is amplified more at the convex corners (G2, G3 and G6) than the concave corners (G1, G4 and G5). It is seen from Figure 6.11 that in the same fashion the current velocity is amplified more at the convex corners (G2, G3 and G6) than the concave corners (G1, G4 and G5).

Therefore, we can conclude that in rhombohedral shaped basins wave amplifications take place in concave points and current amplifications mostly occur in the convex points. This phenomenon is independent of input source shape and location. The only important effect of input source is to find which of the concave or convex points will be affected more. This is predictable by the shape and location of the source. It is obvious from the Figure 6.4 and Figure 6.5 that G1-G4 are more affected in R1 and G5-G8 are more critical for R2 simulations.

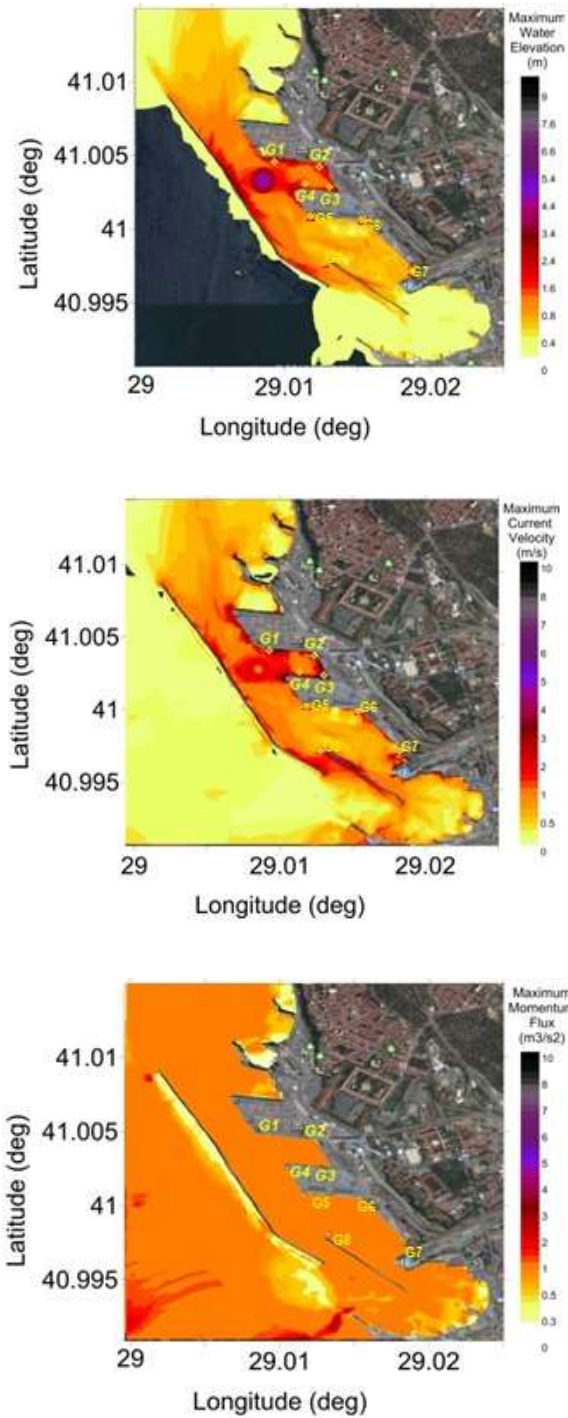


Figure. 6.4. The spatial distribution of maximum water surface elevation, maximum current velocity, and the maximum momentum flux computed by the simulation (R1) of dome shaped source.

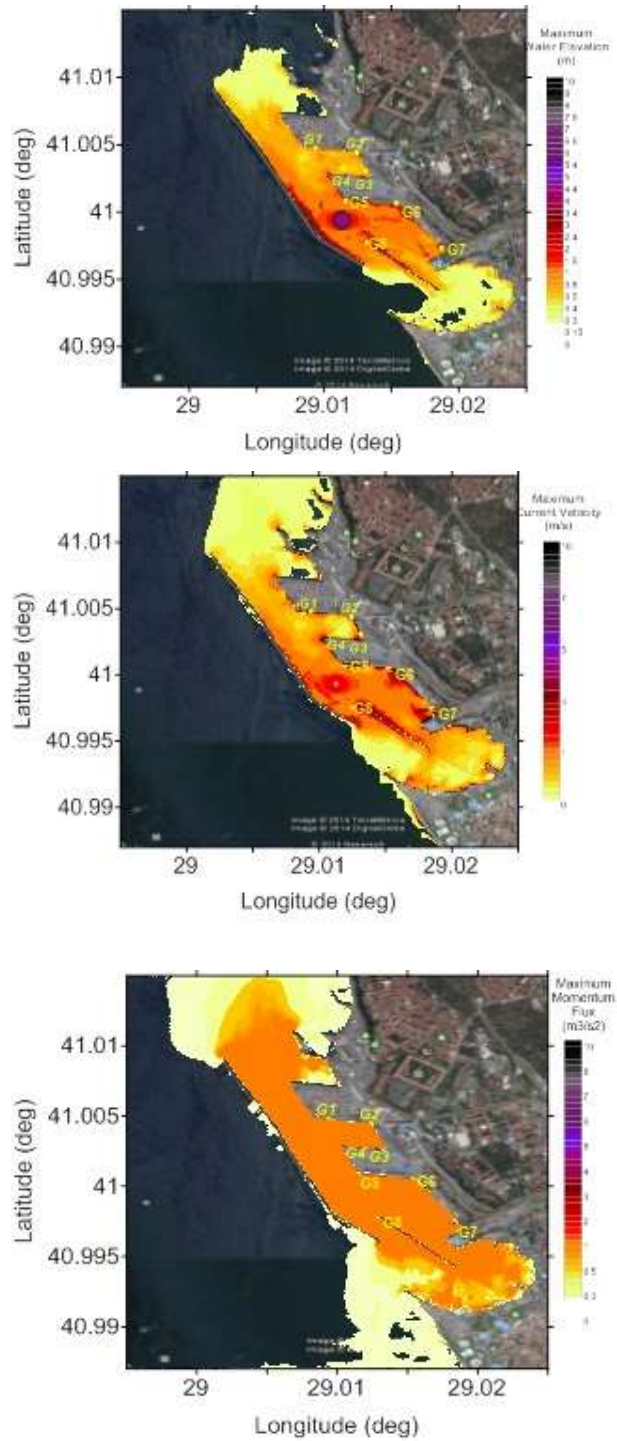


Figure. 6.5. The spatial distribution of maximum water surface elevation, maximum current velocity, and the maximum momentum flux computed by the simulation (R2) of dome shaped source.

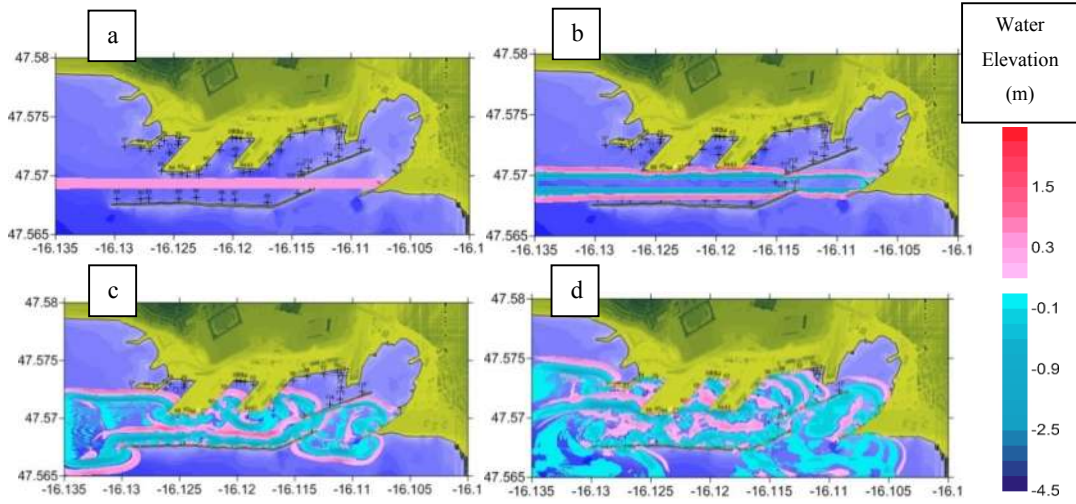


Figure. 6.6 Line impulse in sinusoidal shape (1m amplitude) with crest line parallel to the main breakwater axis in x direction propagates as time history in a) $t = 0$, b) $t = 10s$, c) $t = 30s$, d) $t = 60s$, by the simulation (R3).

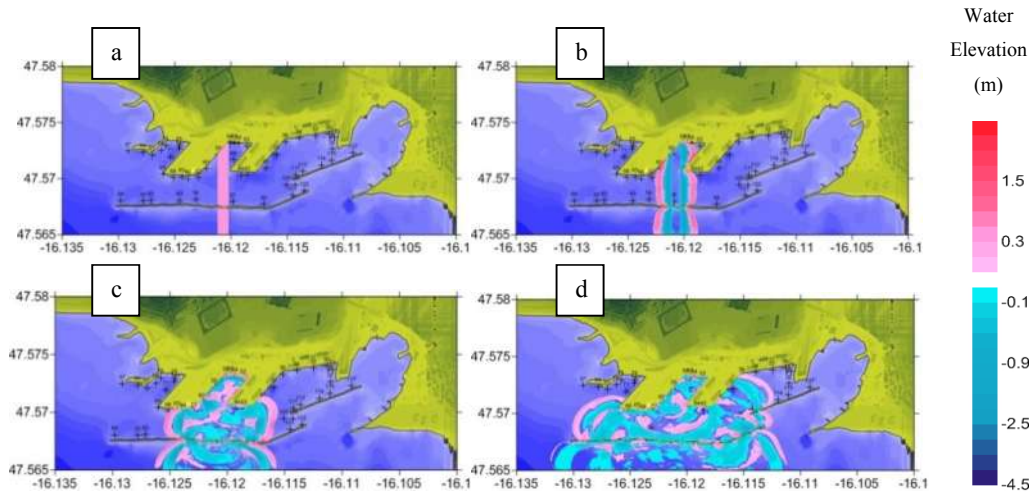


Figure. 6.7. Line impulse in sinusoidal shape (1m amplitude) with crest line perpendicular to the main breakwater axis in x direction propagates as time history in a) $t = 0$, b) $t = 10s$, c) $t = 30s$, d) $t = 60s$, by the simulation (R4).

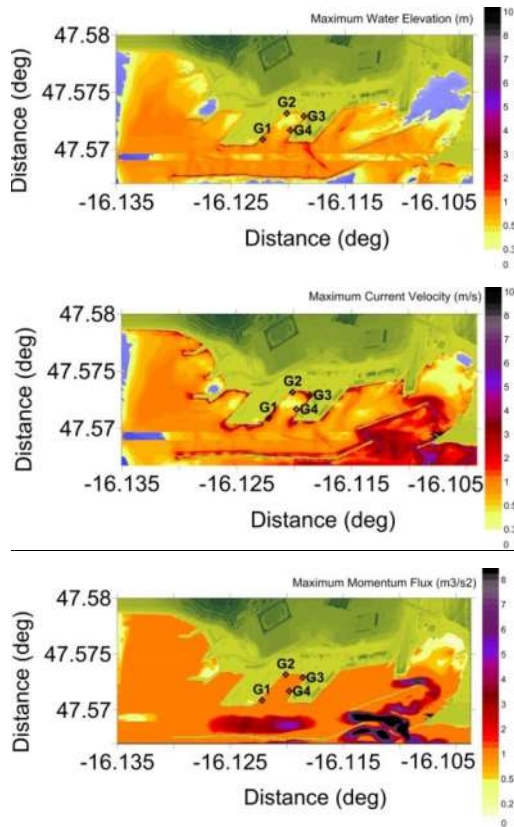


Figure 6.8. The spatial distribution of maximum water surface elevation, maximum current velocity, and the maximum momentum flux computed by the simulation (R3) of sinusoidal shaped line source with the crest parallel to the main breakwater.

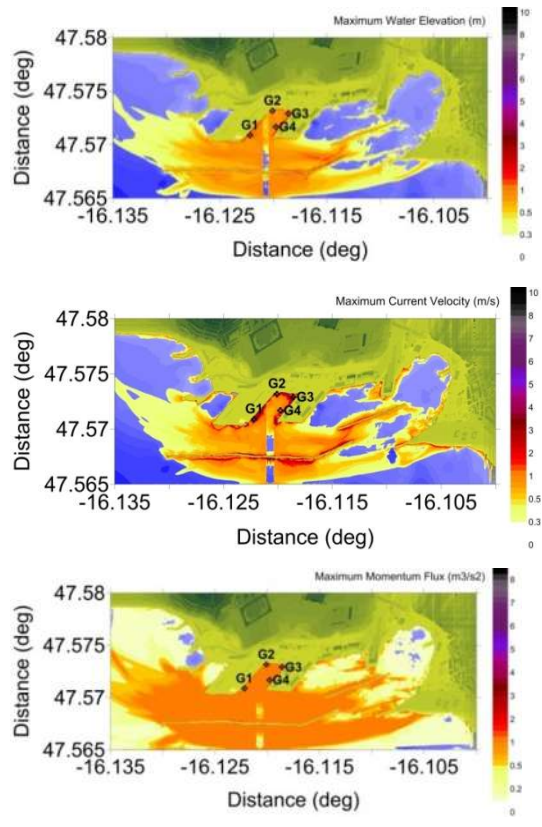


Figure. 6.9. The spatial distribution of maximum water surface elevation, maximum current velocity, and the maximum momentum flux computed by the simulation (R4) of sinusoidal shaped line source with the crest perpendicular to the main breakwater.

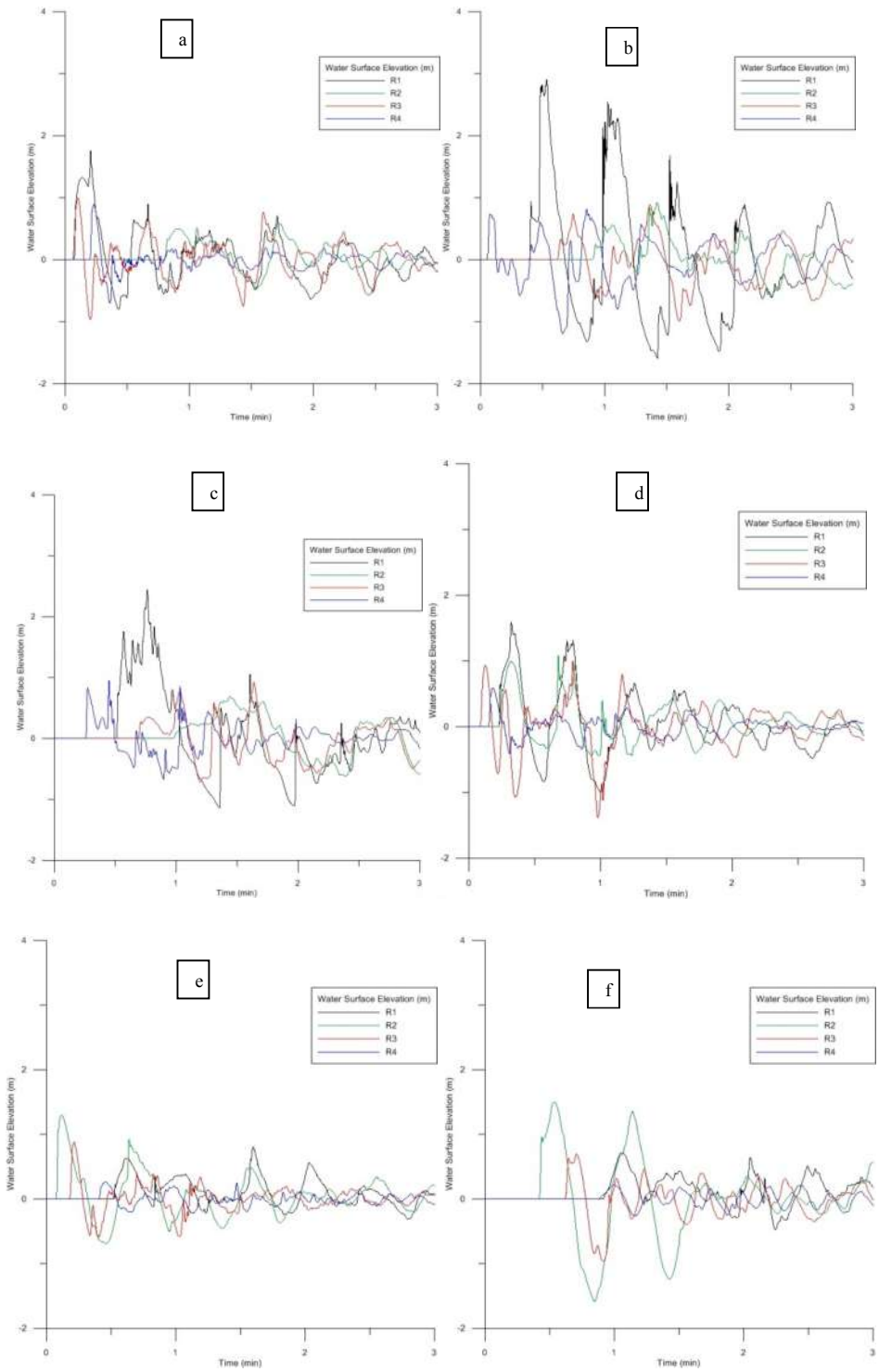


Figure. 6.10. The time histories of water level at numerical gauge locations 1-6 (a-f respectively), computed by the simulations (R1, R2, R3 and R4) for the first 3 minutes of simulation.

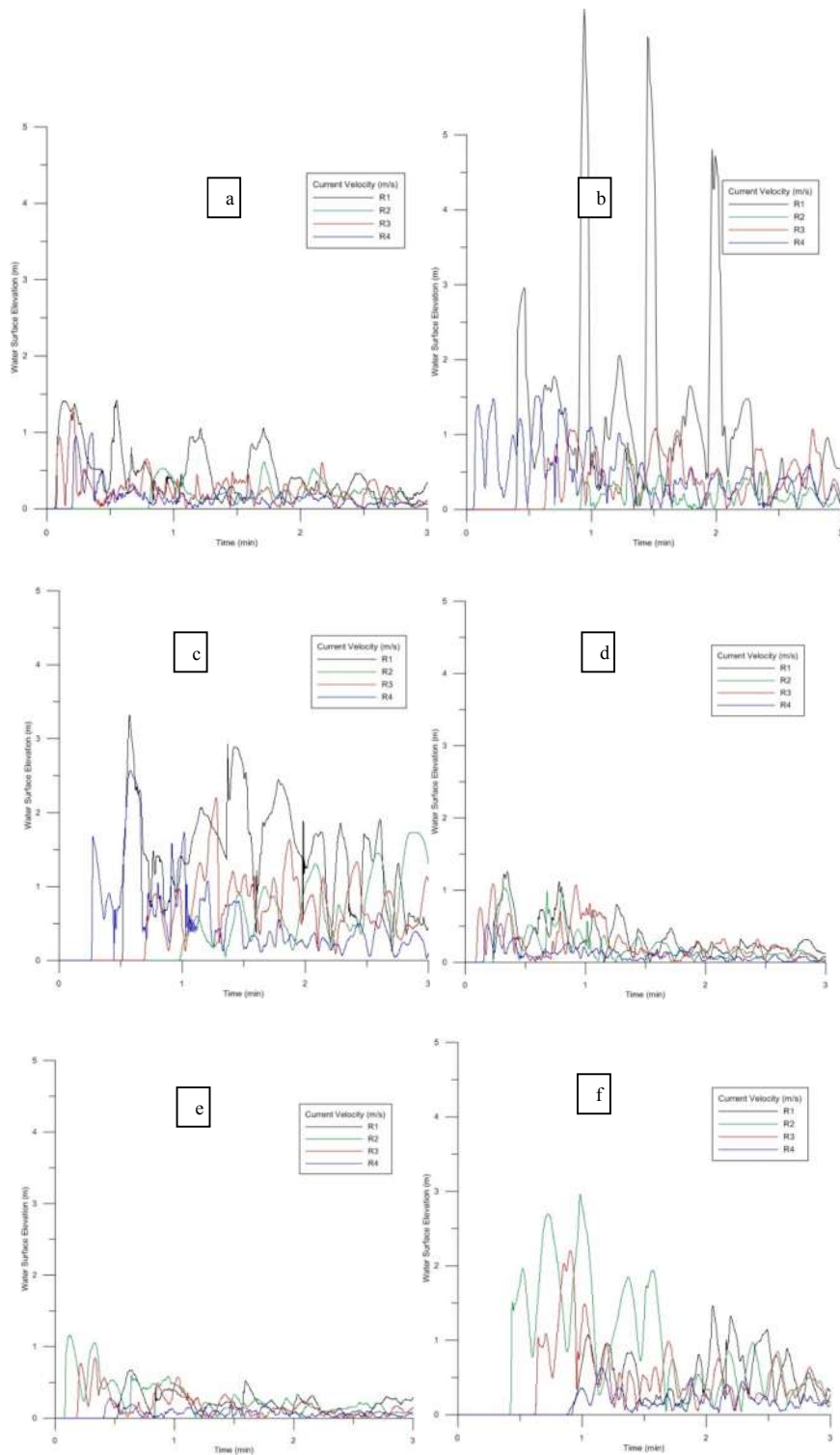


Figure 6.11. The time histories of current velocities at numerical gauge locations 1-6 (a-f respectively), computed by the simulations (R1,R2, R3 and R4) for the first 3 minutes of simulation.

Resilience of harbors and coastal utilities against marine hazards is an important issue. Tsunamis may cause significant damages on ports and may result malfunctioning of the ports during recovery and rescue operations after disasters. Therefore the resilience of ports is one of the important requirements at post disaster conditions. In a closed basin, waves are trapped and last in longer time than semi-enclosed basins. The energy decay is affected by friction, rather than dissipation through an opening. Resonance inside harbors due to tsunami waves can exacerbate the damages by amplifying the water level changes, currents and momentum fluxes.

This chapter has been mainly focused on the assessment of spatial distribution of water level and current velocity amplifications due to the long wave motion inside Haydarpara Port. In the study the inundation of wave has not been considered, however the model is capable to compute inundation. One of the noticeable facts is that the difference in spectral peaks among several gauge records is declarative of effect of basin geometry. The regular (e.g. rhombohedral shaped) basins having fully reflective boundaries (such as in Haydarpara port) can cause resonance and hence amplification of the waves, since the energy inside harbour cannot diminish and may be focused at some locations.

The simulations showed are performed to investigate the resonance periods in Haydarpara harbor using four different input source. It is important to know about these periods because when a long wave with the same period comes to the Haydarpara harbor it causes huge destructions.

6.3. Resonance Periods in Haydarpara Basin

The most common periods coincide with the peaks of spectrum curves (for different initial impulses) are shown in Table 6.1. These periods are selected from the list of periods where the spectrum curve show peak for majority of the gauge locations where the time series are analyzed as given in former sections. Any possible tsunami or long wave approaching to Haydarpara port will cause higher agitation if the period

of the incoming wave coincides with the periods given in Table 6.1. These results are case specific for Haydarpassa Port (Kian et al., 2015a).

Table 6.1. Periods (s) of free oscillations in Haydarpassa Port. Static dome shape wave with 5m amplitude inside the rhombohedral shape basin (first column), Static dome shape wave with 5m amplitude outside the rhombohedral shape basin (second column), Crest line impulses are in parallel (third column) and perpendicular (forth column) directions to the main breakwater with 1m amplitude and 10sec period of sinusoidal wave.

Mode no.	Dome shaped (R1)	Dome shaped (R2)	Line impulse parallel to main breakwater (R3)	Line impulse perpendicular to main breakwater (R4)
1	1311	1311	476.4	1311
2	201.6	201.6	194	218
3	374.4	374.4	150	374.4
4	154.2	154.2	111.6	218.4
5	90.6	90.6	88.8	90.6
6	114	114	66.6	154.2
7	67.2	67.2	55.2	109.2
8	54.6	54.6	45.6	69
9	44.4	44.4	40.2	54.6
10	40.2	40.2	33.6	44.4
11	33.6	34.2	28.2	40.2
12	28.2	33.6	25.2	34.2
13	25.8	28.2	20.4	28.2
14	20.4	25.8	17.4	25.8
15	17.4	20.4	16.2	23.4
16	16.2	17.4	12	20.4
17	12	16.2		17.4
18		12		16.2
19				12

The size, shape and depth of the basin affect the wave amplification according to the period of incident wave when the period coincides with one of the periods of free oscillations of the basin. In general, stronger oscillations occur in long and narrow inlets due to the low rate of energy dissipation and focusing. Inlets with rapid and severe shoal and abrupt contraction are susceptible, when the wave is forced to slow down with decrease in water column depth and the height grows (NOAA, 2014).

The data and experience gained from the simulations and their results indicate that the amplification of water level and current should be expected at corners of the inner basins as shown in the Haydarpaşa port case. The regular shaped inner basins with reflective boundaries can also become critical regions such as the case in Haydarpaşa port.

The resonance periods of the Haydarpaşa port are computed as 1311, 374, 201, 154, 114, 90, 67, 55, 45, 40, 34, 28, 26, 20, 17, 12 seconds (Table 6.1). These results indicate that additional amplifications may be expected in the port if the period of incident waves coincide with one of these values. The periods of tsunamis in the Sea of Marmara may fit some of these periods. Moreover, the periods of waves generated in extreme storms may also be long enough to fit one of these resonance periods.

Wave energy dissipaters (absorbing boundaries) at critical locations inside the basin are one of the options to control the unexpected wave amplifications inside the harbors under extreme conditions and hence become one of the mitigation measures.

6.4. Long Wave Effects on Haydarpaşa Basin.

Wave and current amplifications and consequent sediment transport in Haydarpaşa harbor are investigated to see what happens when it exposed to long waves intrusion with several different long wave periods. Some of these wave periods are selected to identify the resonance in Haydarpaşa. The results are summarized in Table 6.1. The selected wave periods are 67, 90, 154, 200, 800, 900 seconds with 1m and 2m wave amplitude. The periods of 200, 154, 90, 67 seconds are the third, fourth, sixth,

seventh modes of resonance periods of the Haydarpaşa Harbor respectively. Figure 6.12 shows the long wave propagation with 1m amplitude and 90sec period towards the Haydarpaşa Harbor. The simulation is performed for 40 minutes duration with 0.005 second of time steps.

Ayca (2012) studied on six different seismic based tsunami scenarios in the Sea of Marmara. The maximum and minimum wave amplitudes in Haydarpaşa are obtained 1.4m and -4.5m in his study. Therefore, in this thesis 1m and 2m are selected as the most representative wave amplitudes of tsunami and used as inputs in simulations for Haydarpaşa Harbor.

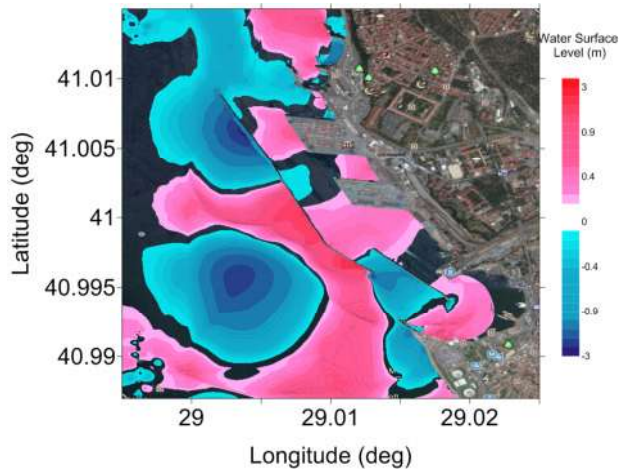
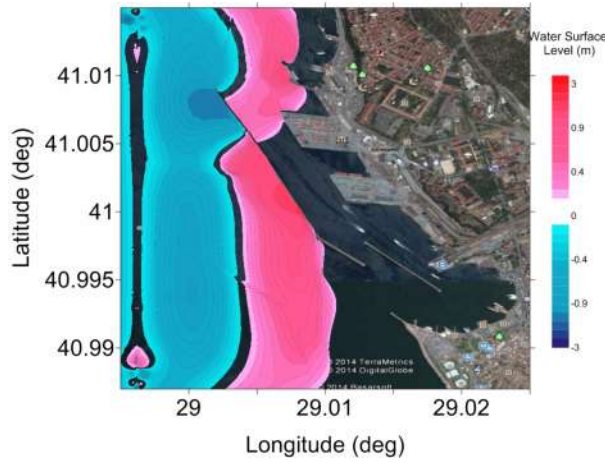
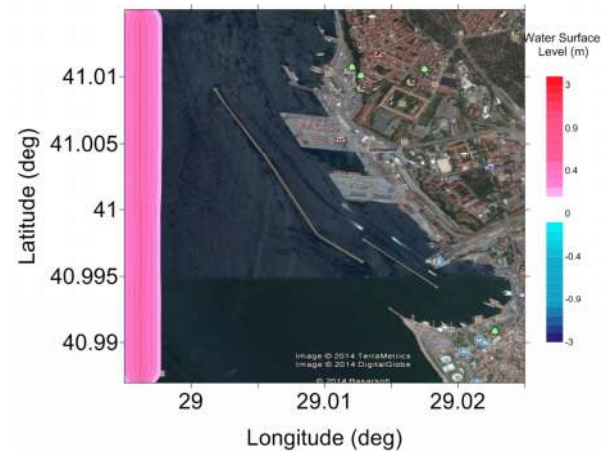


Figure. 6.12. Long wave with 1m amplitude and 90s period, propagates towards the Haydarpasa Harbor in a) $t = 10$, b) $t = 90$ s, c) $t = 200$ s.

Figures 6.13 and 6.14 represent the maximum water surface elevation for sinusoidal crest line wave input with 67, 90, 154, 200, 800 and 900 seconds of wave period in 6.13 (a-f) with 1m amplitude and 6.14 (a-f) for 2m wave amplitude respectively. The source distance to the main breakwater is about 1km. In the same fashion figures 6.15 (a-f) shows the simulation results for maximum current velocity for 1m wave amplitude and figures 6.16 (a-f) for 2m wave amplitude. Figure 6.17 (a-f) and Figure 6.18 (a-f) represent the minimum Rouse Number with maximum velocity vectors on the map for 1m wave amplitude in Figure 6.17 and 2m wave amplitude in Figure 6.18.

Figure 6.13 (a-d) and Figure 6.14 (a-d) show that maximum water elevation inside the rhombohedral basin increases by wave period increasing when the periods are resonance periods. The behavior is similar outside of the basin, behind the main breakwater, when wave periods are 800sec and 900sec (normal periods) there is no wave amplification inside the inner rhombohedral shaped basin, but for the outer rhombohedral shaped basin the maximum wave elevation is higher than the inner ones.

Comparing the results of the maximum current velocity in Figure 6.15 and Figure 6.16 for 1m and 2m input wave amplitude show that increasing the input wave height increases the current velocity in the selected gauge points in the harbor. Current amplification in the Haydarpaşa Harbor entrance is increases by increasing the wave period value and it is independent of the resonance period even if the period is equal to the resonance period or not. Behind the main breakwater outside the Haydarpaşa Harbor, when the period is equal to the resonance period, the current velocity increases along the period increasing.

6.5. Amplification in Haydarpaşa Harbor

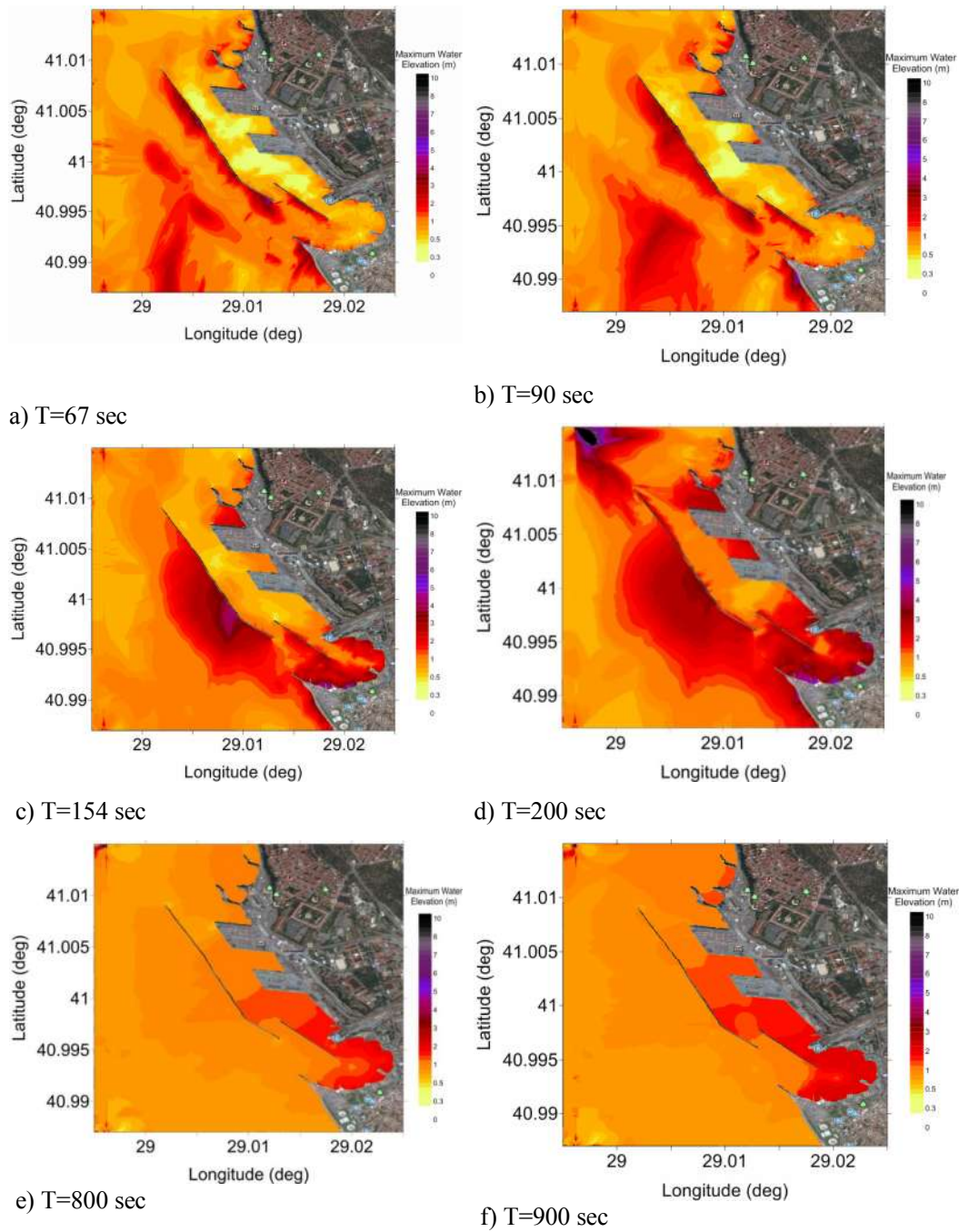


Figure. 6.13. The spatial distribution of maximum water surface elevation (m) computed by the simulation of sinusoidal line crest long wave with 1m wave amplitude with a) T=67s, c) T=90s, c) T=154s, d) T=200s, e) T=800s and f) T=900s respectively.

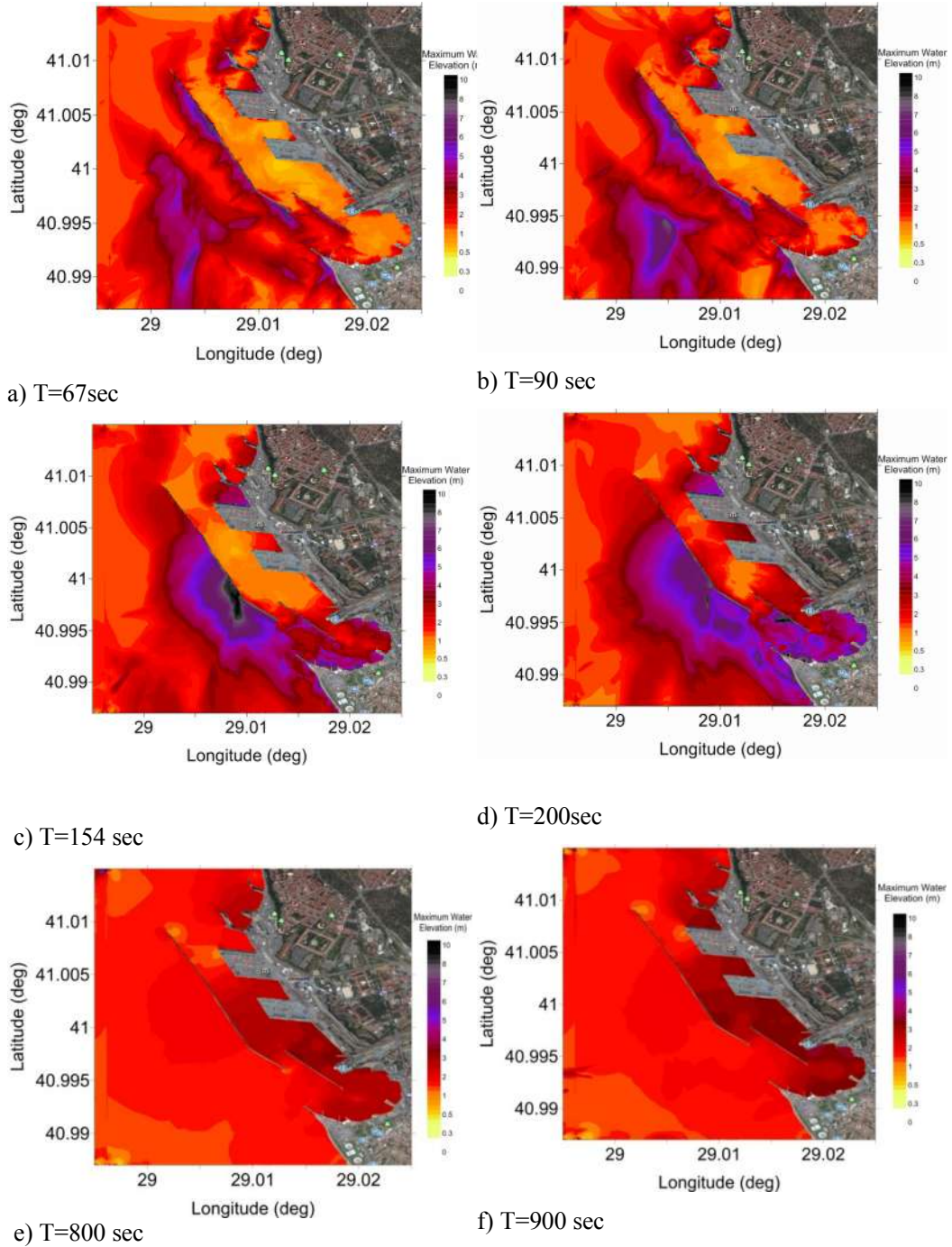


Figure. 6.14. The spatial distribution of maximum water surface elevation (m) computed by the simulation of sinusoidal line crest long wave with 2m wave amplitude with a) $T=67\text{s}$, c) $T=90\text{s}$, c) $T=154\text{s}$, d) $T=200\text{s}$, e) $T=800\text{s}$ and f) $T=900\text{s}$ respectively.

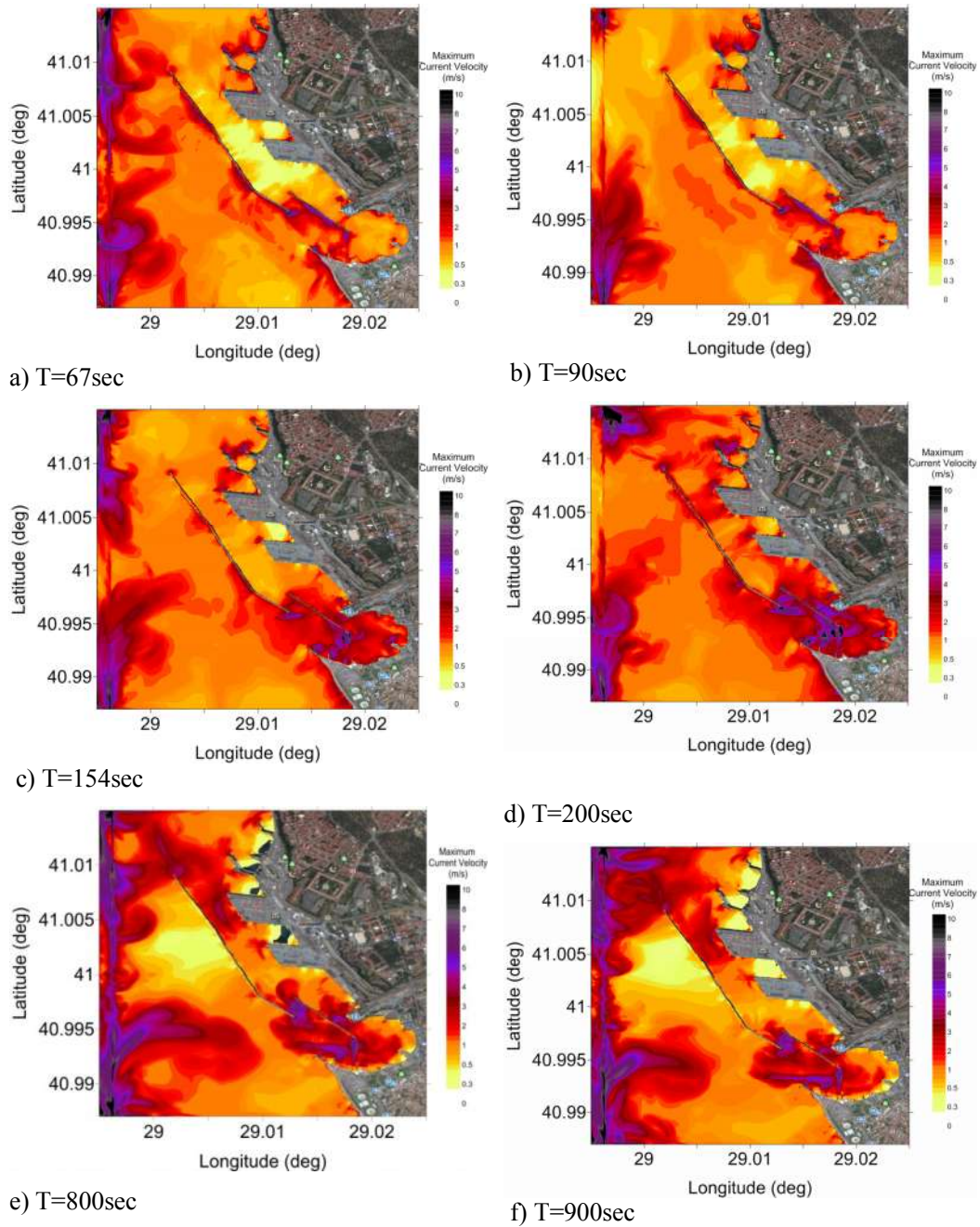


Figure. 6.15. The spatial distribution of maximum current velocity (m/s) computed by the simulation of sinusoidal line crest long wave with 1m wave amplitude with a) $T=67\text{s}$, c) $T=90\text{s}$, c) $T=154\text{s}$, d) $T=200\text{s}$, e) $T=800\text{s}$ and f) $T=900\text{s}$ respectively.

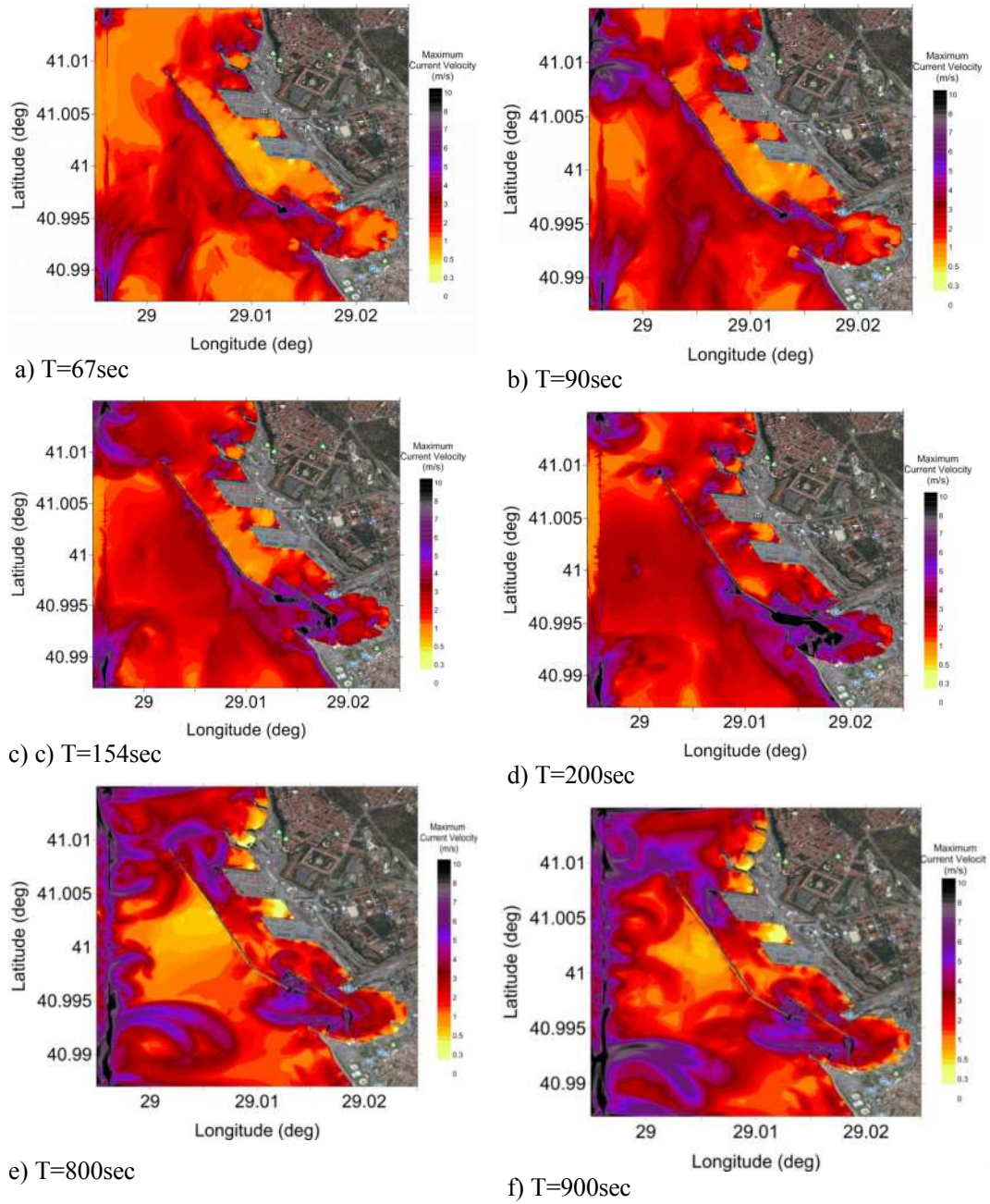


Figure. 6.16. The spatial distribution of maximum current velocity (m/s) computed by the simulation of sinusoidal line crest long wave with 2m wave amplitude with a) $T=67s$, c) $T=90s$, c) $T=154s$, d) $T=200s$, e) $T=800s$ and f) $T=900s$ respectively.

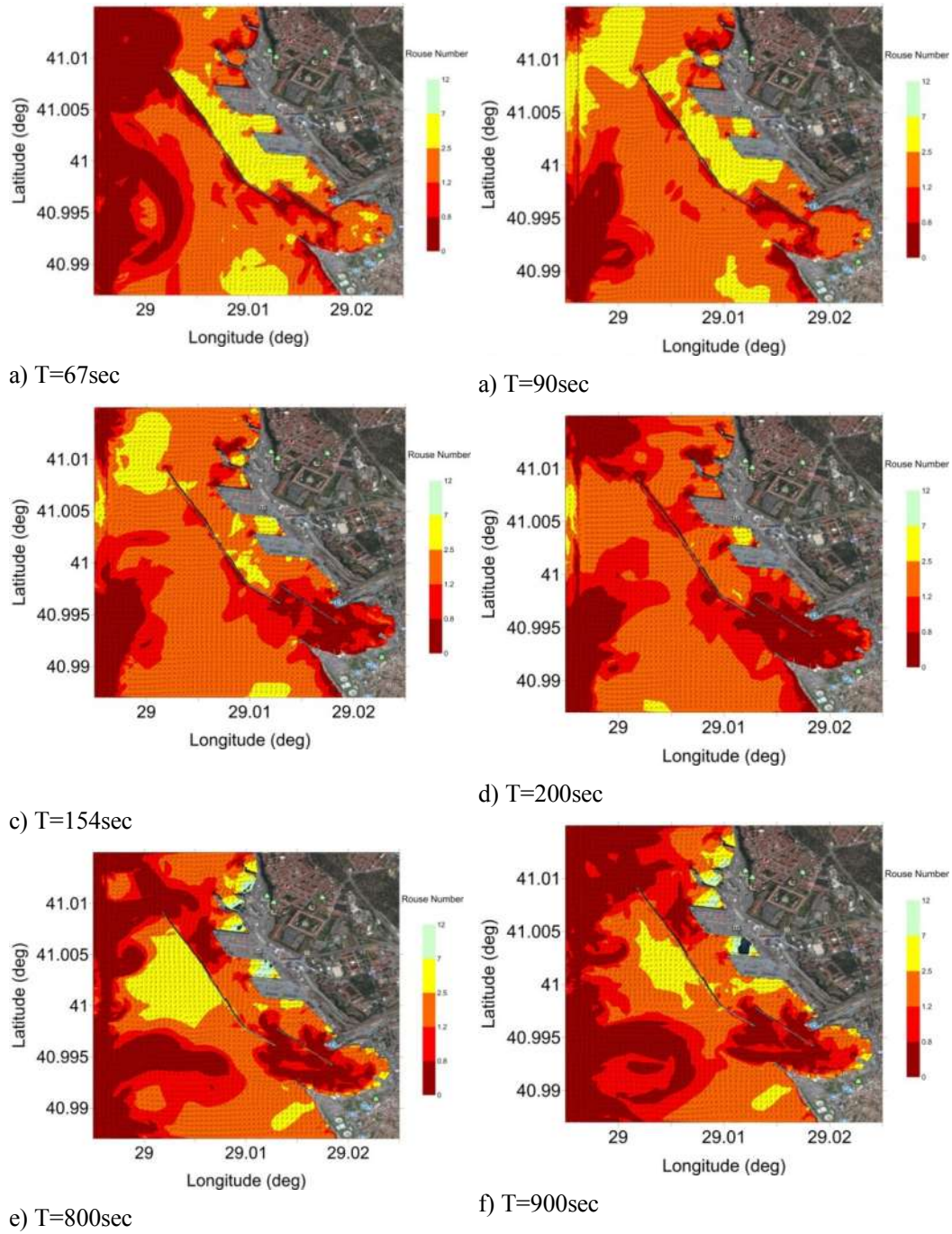


Figure. 6.17. The spatial distribution of minimum Rouse Number computed by the simulation of sinusoidal line crest long wave with 1m wave amplitude with a) T=67s, c) T=90s, c) T=154s, d) T=200s, e) T=800s and f) T=900s respectively. The maximum velocity vectors are also shown on each case.

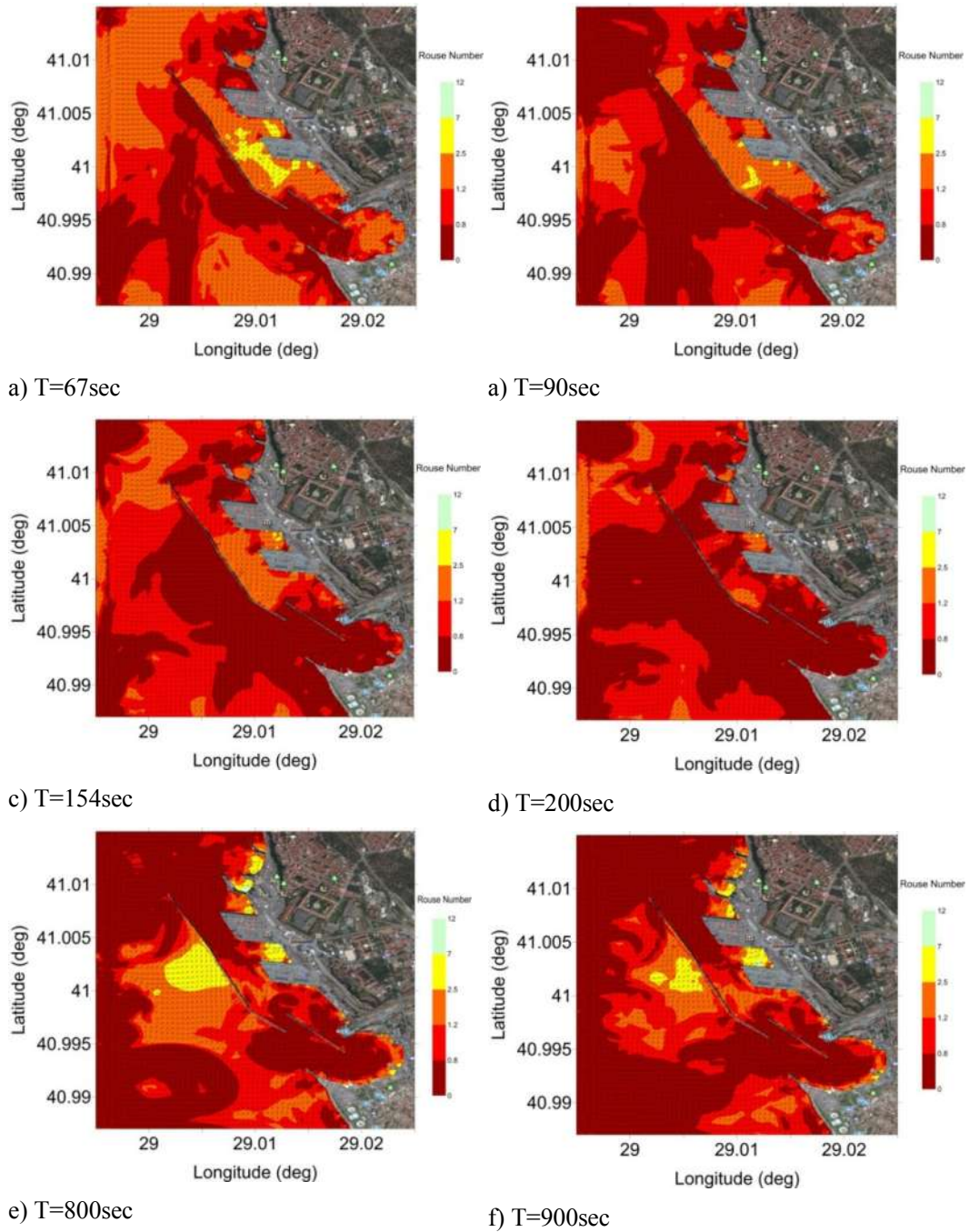


Figure. 6.18. The spatial distribution of minimum Rouse Number computed by the simulation of sinusoidal line crest long wave with 2m wave amplitude with a) T=67s, c) T=90s, c) T=154s, d) T=200s, e) T=800s and f) T=900s respectively. The maximum velocity vectors are also shown on each case.

In order to see the wave and current amplification results and the morphological changes in critical points in Haydarpasa Harbor, eight gauge points are selected and then the time history of related water surface elevation and current velocity are plotted for the first 30 minutes of simulation. Figure 6.19 shows the time history of water surface elevation and current velocity and the Rouse Number in G7. The graphs in Figure 6.19 to 6.26 show the results for the periods of 67, 90, 154, 200, 800 and 900 seconds which the first four periods are selected among the resonance periods listed in Table 6.1. Figure 6.19 show that when the period is 90sec wave amplification takes place but the current amplification occurs in 90, 154 and 200 seconds of wave period. The sediment motion in G7 is in bed load form.

Figure 6.20 shows that in G6 in the concave part of the basin, both wave and current amplifications occur when the wave period is equal to 200 sec. The G5 in the convex part of the outer rhombohedral basin, we have wave and current amplifications for 154sec and 200sec wave periods. Also, the sediment movement is mostly in bed load form. When the wave period is 200 sec the sediment movement is shortly in suspended load form and it turns into the bed load form (Figure 6.21).

At G4 (Figure 6.22) in the corner point of rhombohedral shaped basin, amplification occurs in both wave amplitude and current velocity when the wave period is 200 seconds. The sediment movement in this point is generally in the form of bed load, however, shortly after 10 minutes of wave propagation the sediments there move like suspended loads. The sediments mostly move in bed load form in Haydarpasa Harbor.

Figure 6.23 shows that in G3 in the concave part of the basin, the wave amplitude amplifies when the wave period is equal to 200 sec and the current velocity amplifies when the period is 154 and 200sec. The sediment movement in the gauge point is almost in bed load mode for smaller periods but in higher periods it is suspended load. The amplification situation and the sediment motion in G2, the corner point in concave part of the basin in Figure 6.24 and the G1 is similar to the G4 in Figure 6.22, except the sediment movement in G1 is suspended load. In the Harbor entrance at G8, wave amplifies when wave period is 200sec and the current velocity amplifies

when the wave period is 154 sec and 200 sec. The Rouse Number value is mostly larger than 2.5 between two break waters and therefore the sediment movement is bed load form and when the period is 154 sec, 200-sec and 800 sec the movement is in suspended form.

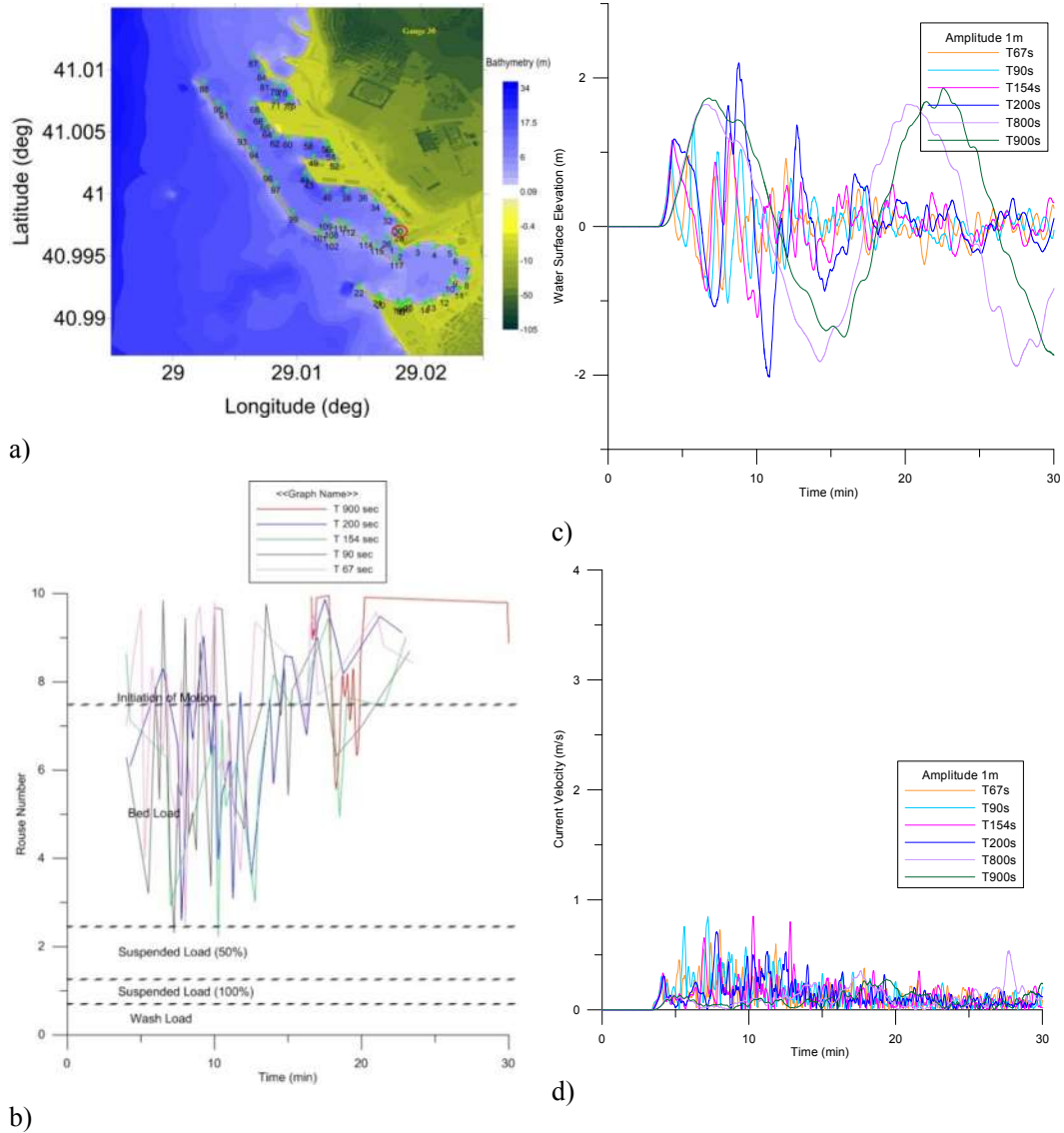


Figure. 6.19. Haydarpasa Harbor a) bathymetry and the gauge points used in the simulations, b) Rouse Number, c) time history of water surface elevation d) time history of current velocity in G7.

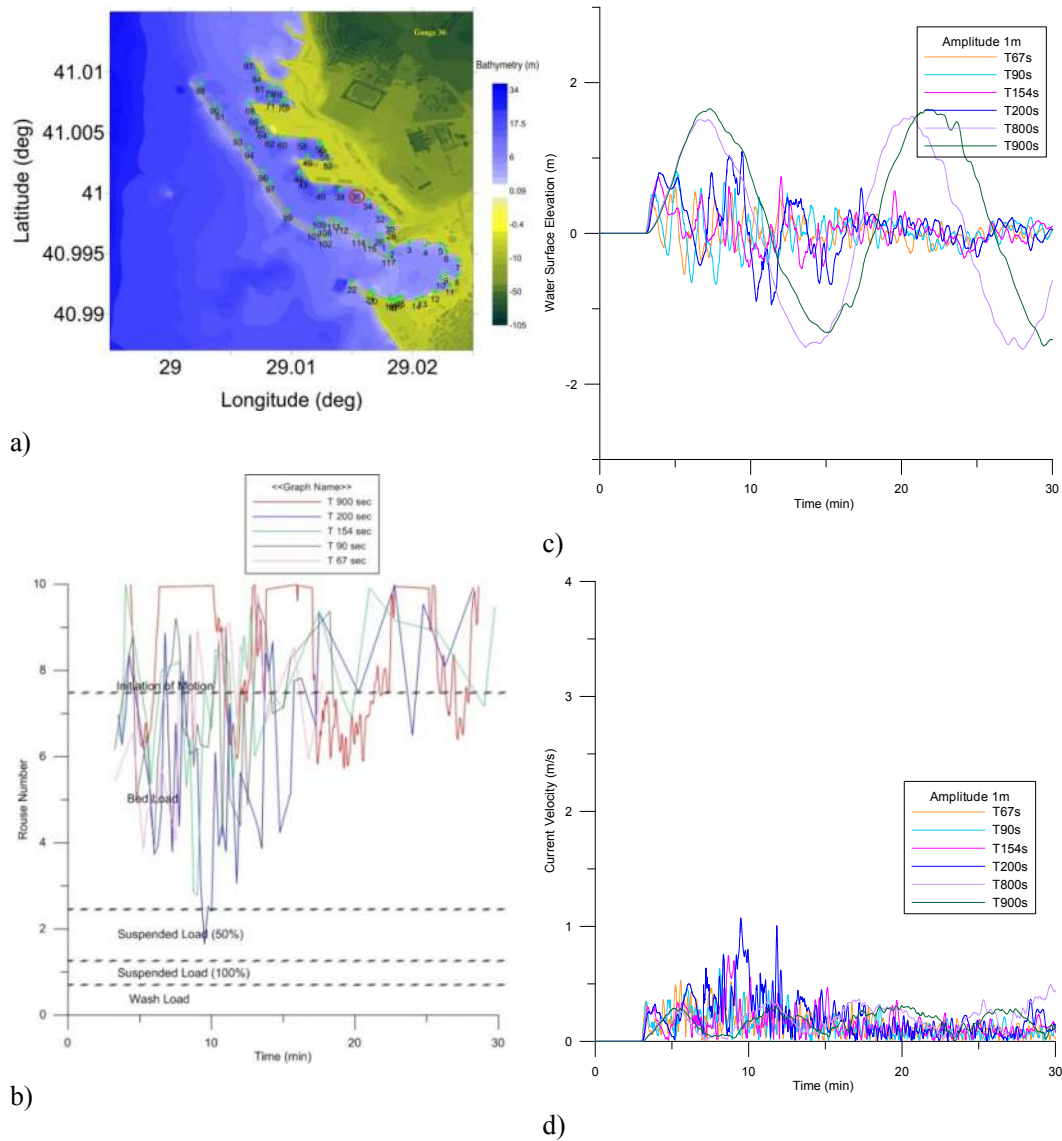


Figure 6.20. Haydarpasa Harbor a) bathymetry and the gauge points used in the simulations, b) Rouse Number, c) time history of water surface elevation d) time history of current velocity in G6.

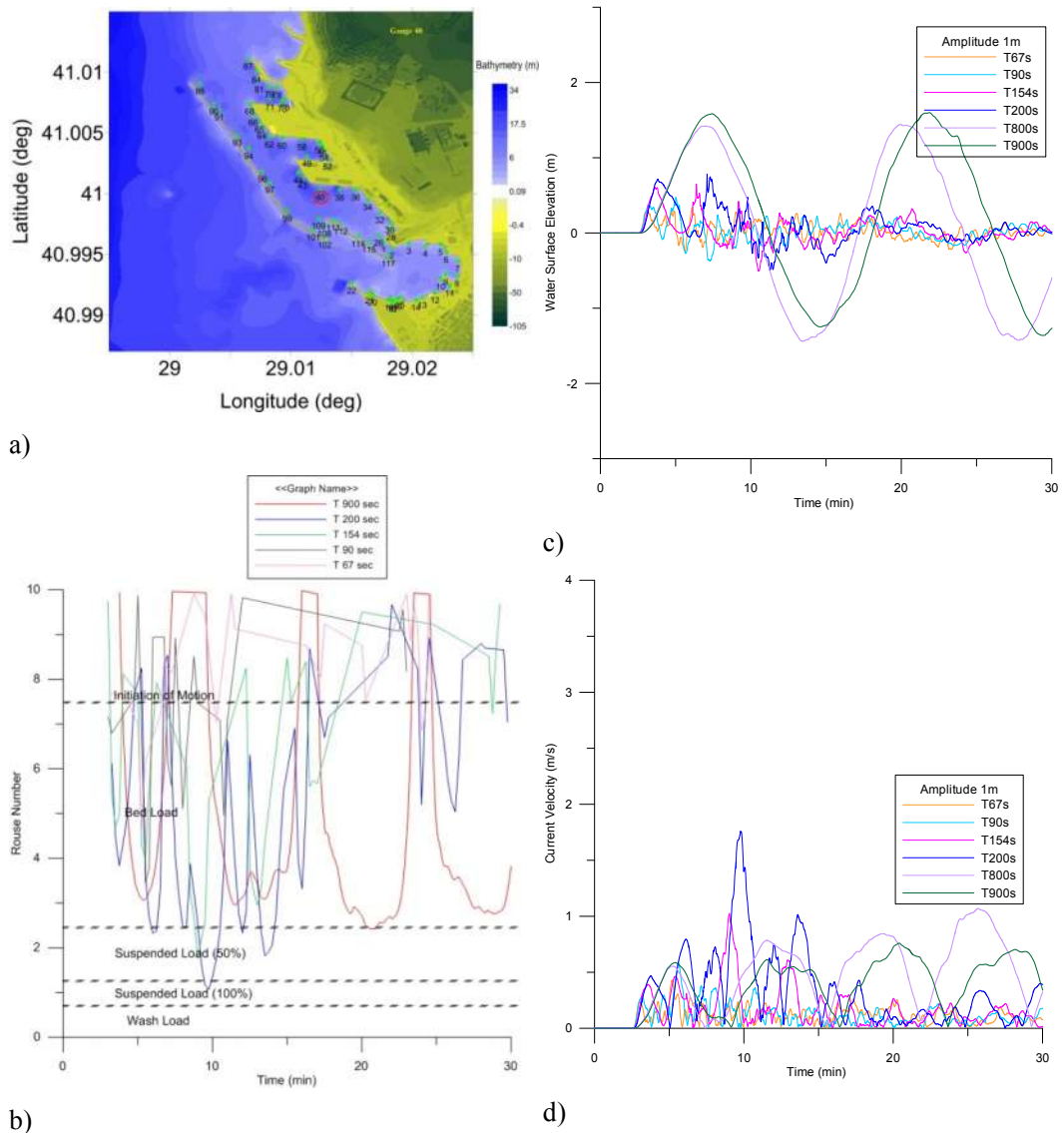
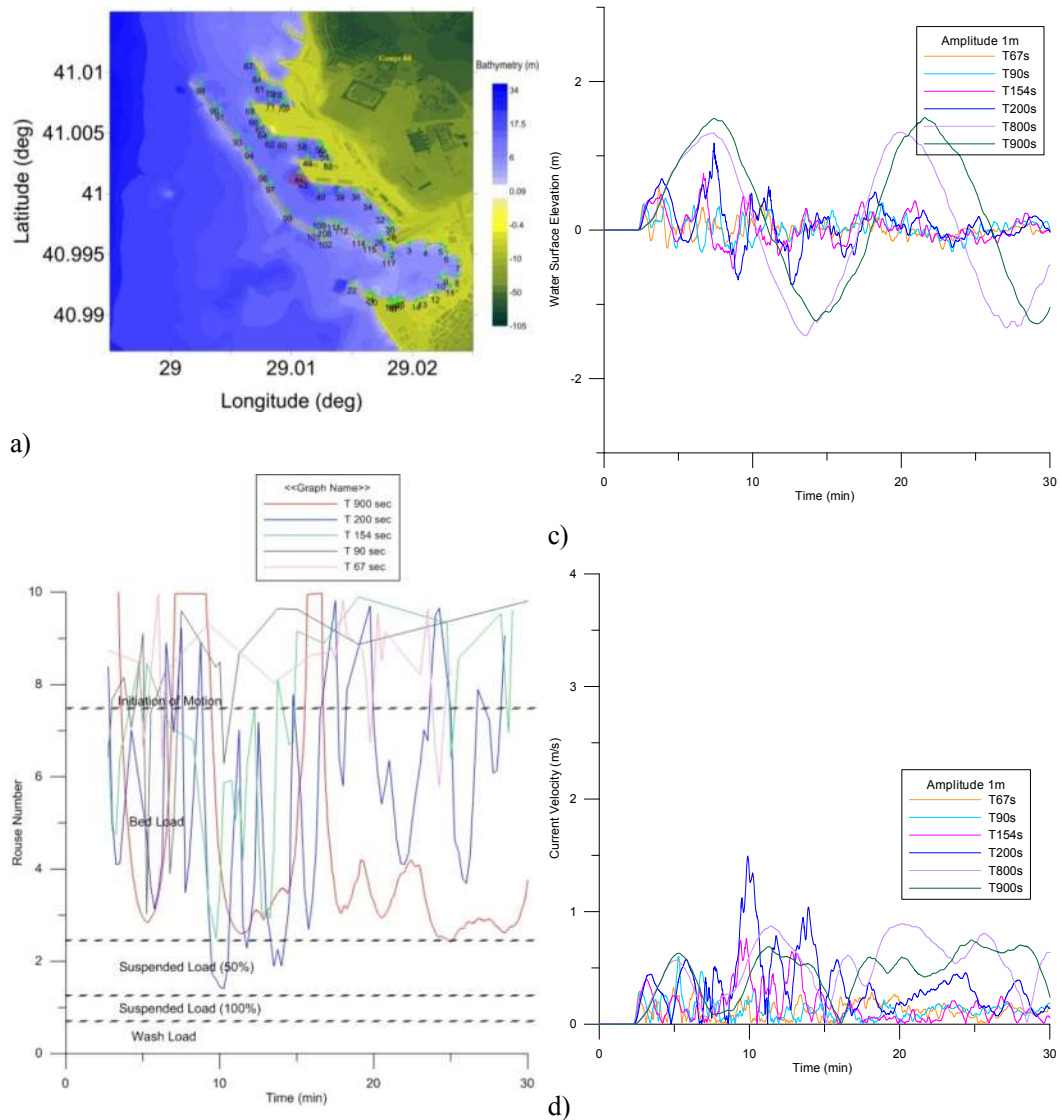


Figure. 6.21. Haydarpasa Harbor a) bathymetry and the gauge points used in the simulations, b) Rouse Number, c) time history of water surface elevation d) time history of current velocity in G5.



b) Figure. 6.22. Haydarpasa Harbor a) bathymetry and the gauge points used in the simulations, b) Rouse Number, c) time history of water surface elevation d) time history of current velocity in G4.

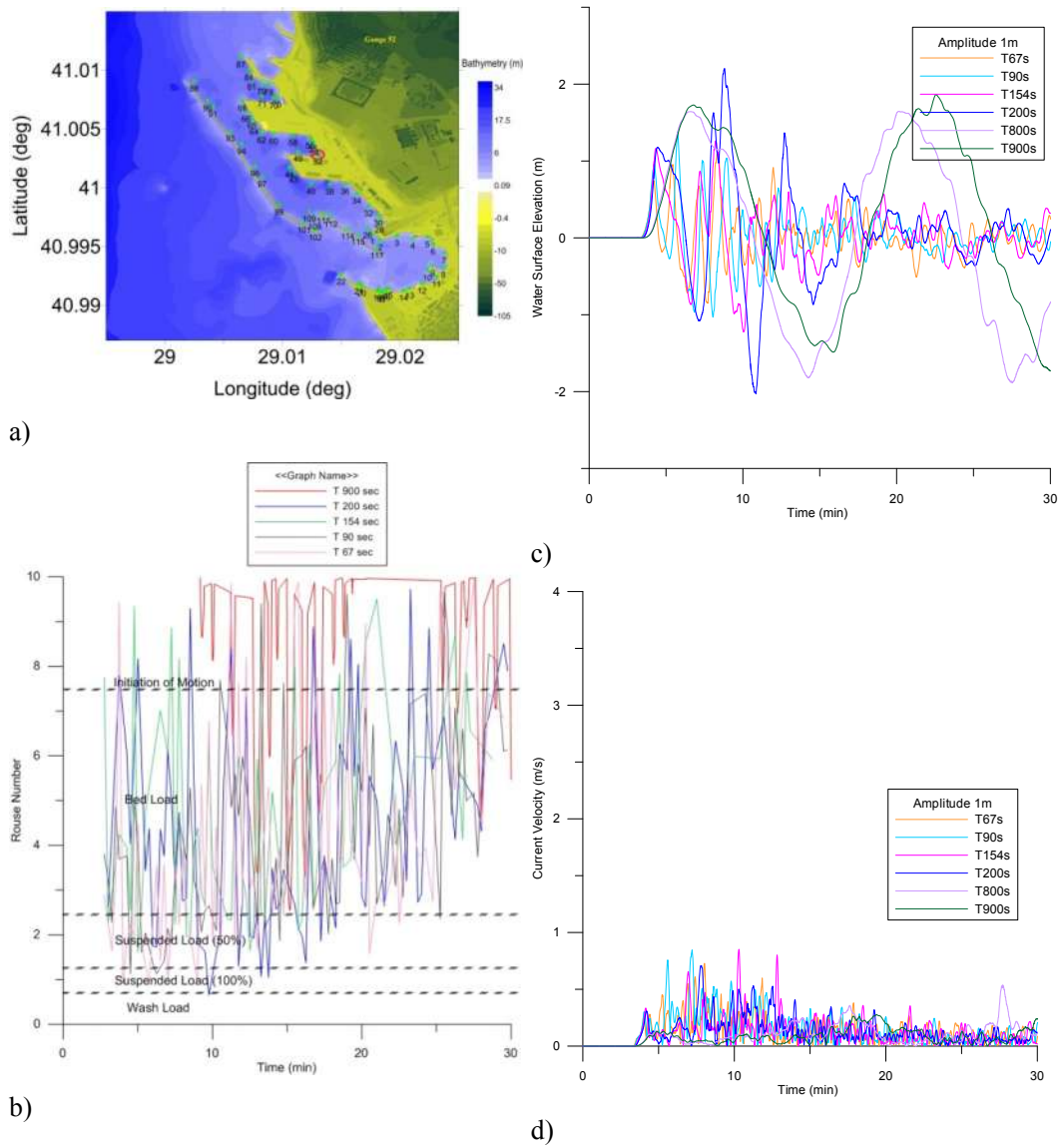


Figure. 6.23. Haydarpasa Harbor a) bathymetry and the gauge points used in the simulations, b) Rouse Number, c) time history of water surface elevation d) time history of current velocity in G3.

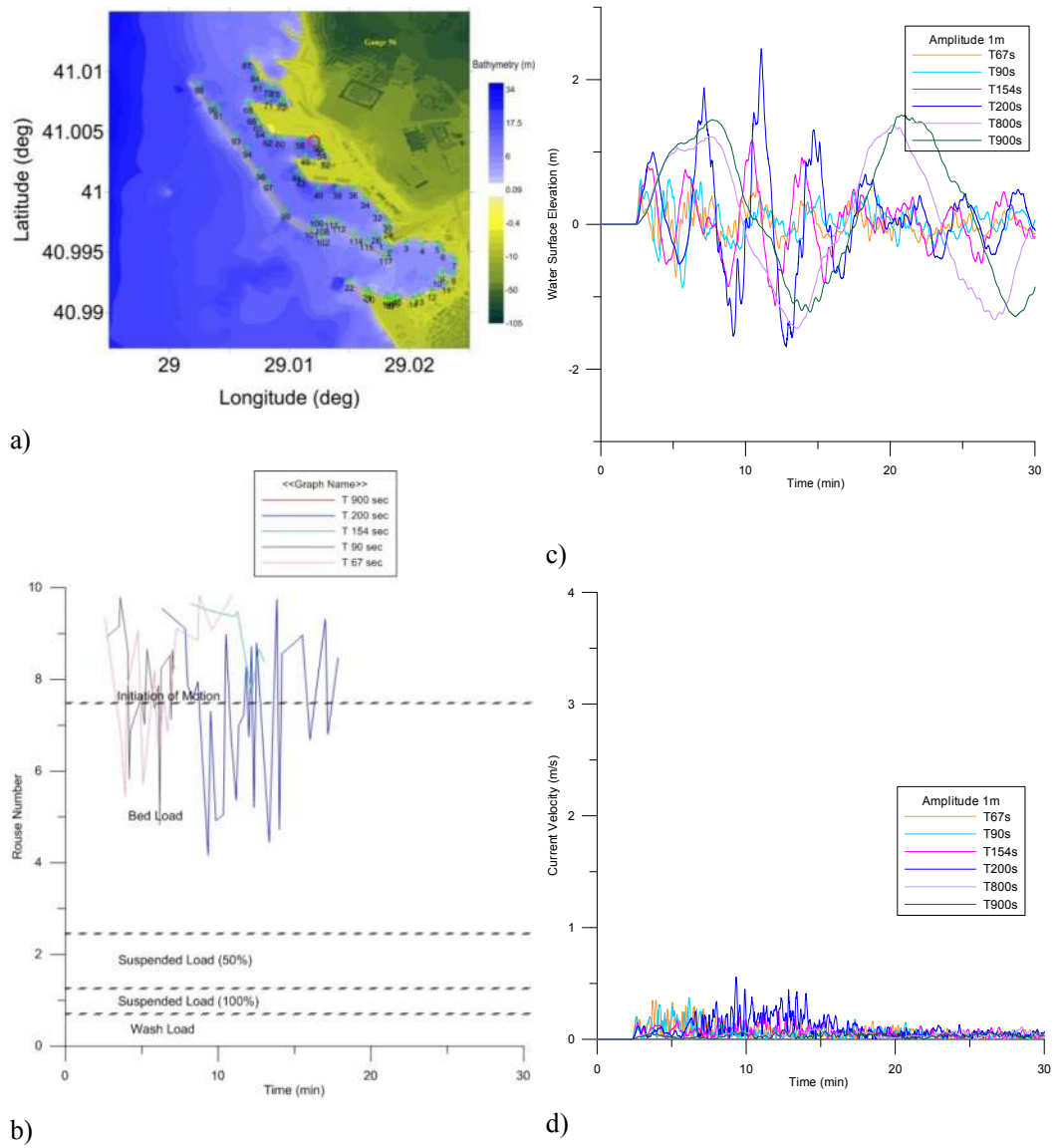


Figure 6.24. Haydarpasa Harbor a) bathymetry and the gauge points used in the simulations, b) Rouse Number, c) time history of water surface elevation d) time history of current velocity in G2.

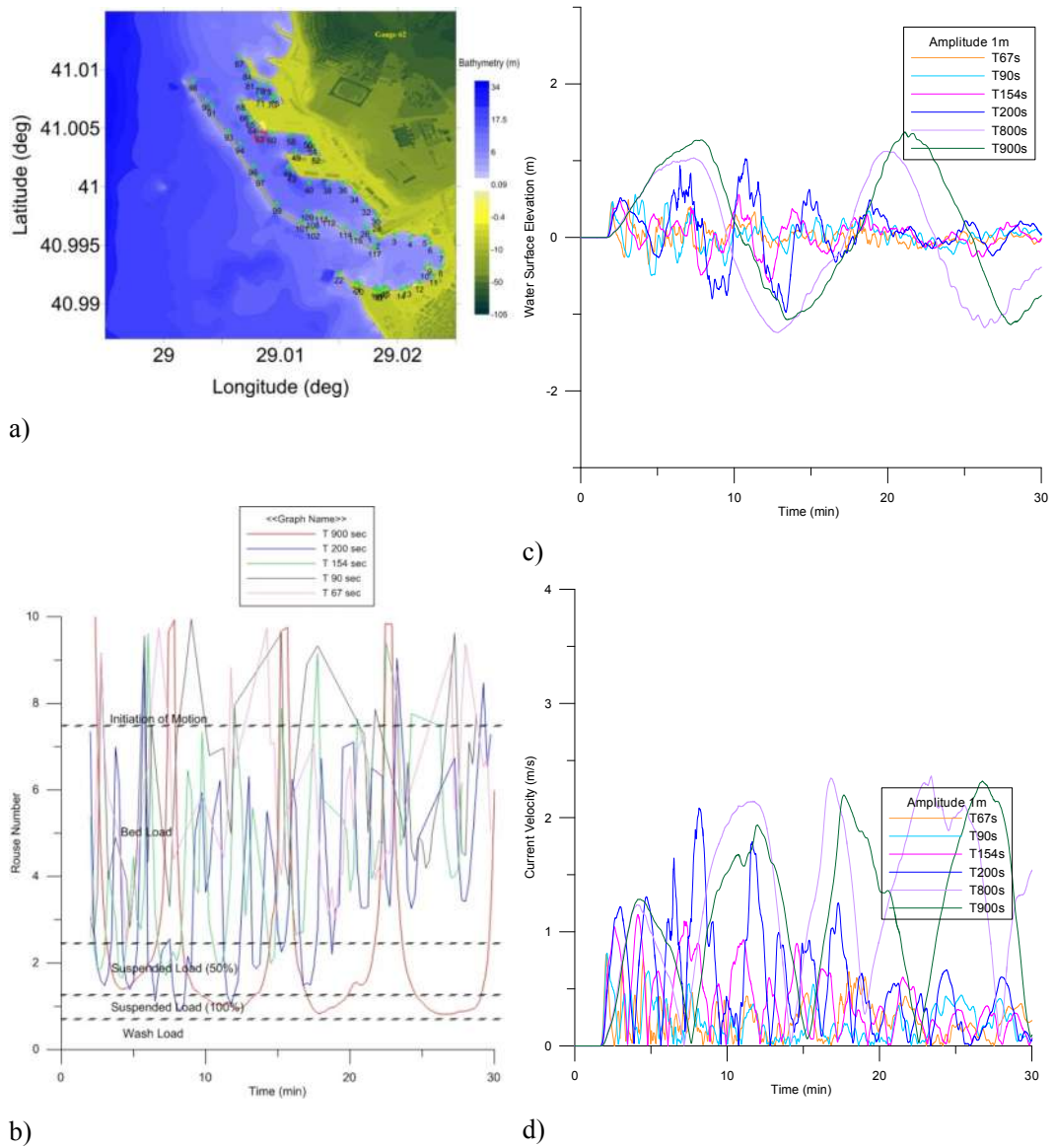


Figure. 6.25. Haydarpasa Harbor a) bathymetry and the gauge points used in the simulations, b) Rouse Number, c) time history of water surface elevation d) time history of current velocity in G1.

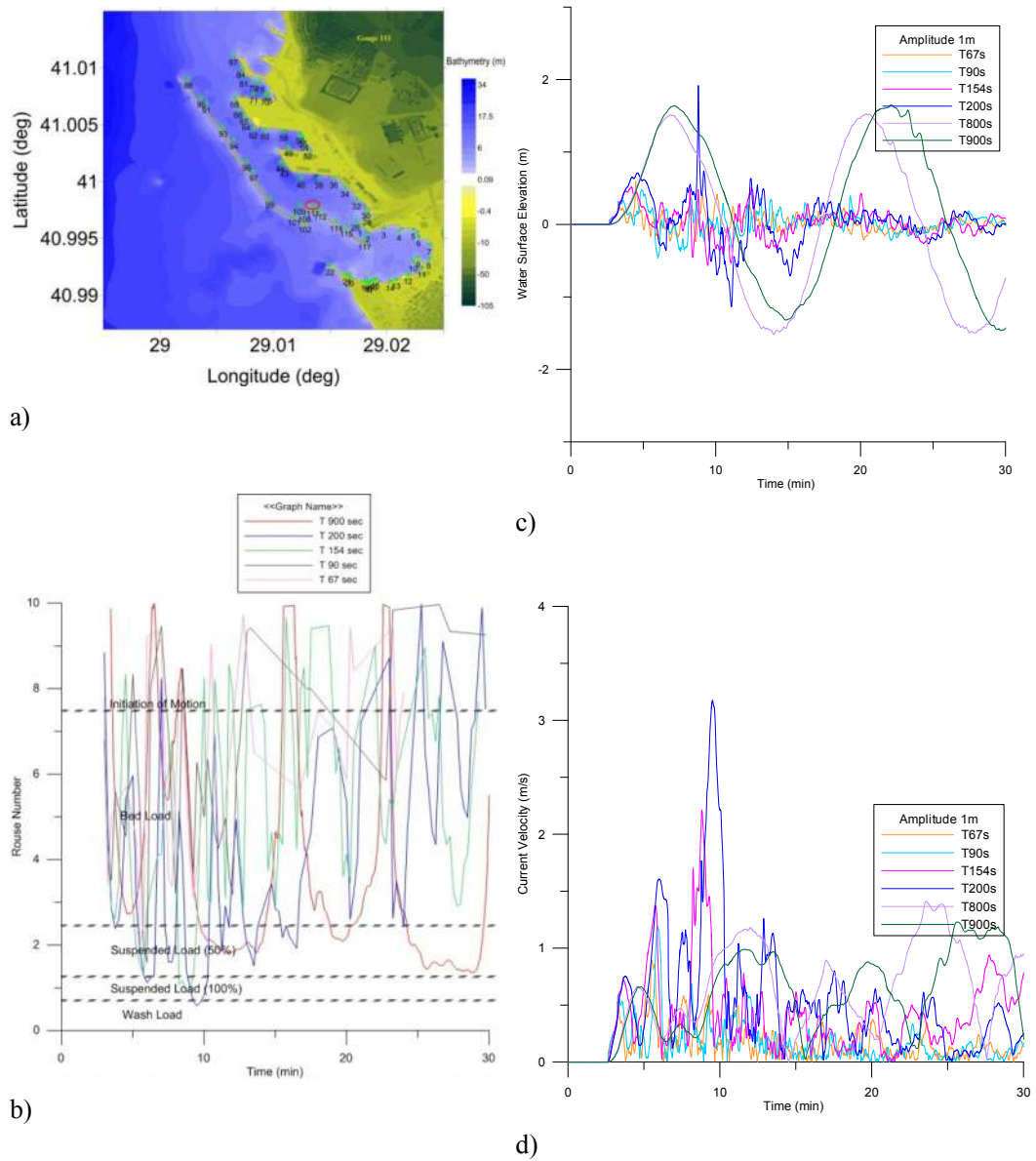


Figure. 6.26. Haydarpaşa Harbor a) bathymetry and the gauge points used in the simulations, b) Rouse Number, c) time history of water surface elevation d) time history of current velocity in G8.

The Tables 6.2 to 6.7 summarize the Figures 6.13 to 6.26. The tables show that the G3 in the concave corner of rhombohedral shaped basin as a critical point, the amplifications occur in most of the wave periods. Generally the wave amplification and the current amplification take place simultaneously. According to the results, in

most of cases G1 is more disposed to the both wave and current amplification occurrences. Generally wave and current amplifications take place simultaneously. For most wave periods the point at the convex corner of the rhombohedral shaped basin at Haydarpaşa Harbor G1 is more probable to current amplification occurrence.

Table 6.2. Maximum water surface elevation, maximum current velocity and minimum Rouse Number in G7, G6, G5, G4, G3, G2, G1 and G8 in Haydarpaşa Harbor in 67sec wave period in columns 4, 5, 6 respectively. Sinusoidal line crest 1m wave amplitude is 1km far from the main breakwater. X coordinate of the gauge point (second column), Y coordinate of the gauge point (third column).

Gauge No	X-coord (deg)	Y-coord (deg)	Max. Water Surface Elevation (m)	Max. Current (m/s)	Min. Rouse Number
G7	29.0182	40.9976	1.1	0.7	2.5
G6	29.0153	41.0003	0.6	0.6	3.4
G5	29.0124	41.0003	0.4	0.5	4
G4	29.0106	41.0017	1.6	0.4	5.4
G3	29.0130	41.0029	1.4	3.2	0.8
G2	29.0123	41.0042	0.7	0.4	5.4
G1	29.0082	41.0047	0.5	0.8	2.4
G8	29.0135	40.9978	0.7	0.9	2

Table 6.3. Maximum water surface elevation, maximum current velocity and minimum Rouse Number in G7, G6, G5, G4, G3, G2, G1 and G8 in Haydarpaşa Harbor in 90sec wave period in columns 4, 5, 6 respectively. Sinusoidal line crest 1m wave amplitude is 1km far from the main breakwater. X coordinate of the gauge point (second column), Y coordinate of the gauge point (third column).

Gauge No	X-coord (deg)	Y-coord (deg)	Max. Water Surface Elevation (m)	Max. Current (m/s)	Min. Rouse Number
G7	29.0182	40.9976	1.5	0.9	2
G6	29.0153	41.0003	0.9	0.7	3
G5	29.0124	41.0003	0.5	0.6	3
G4	29.0106	41.0017	0.5	0.6	3.1
G3	29.0130	41.0029	1.7	1.8	1
G2	29.0123	41.0042	0.8	0.4	4.8
G1	29.0082	41.0047	0.6	0.8	2.5
G8	29.0135	40.9978	0.5	1.3	1.6

Table 6.4. Maximum water surface elevation, maximum current velocity and minimum Rouse Number in G7, G6, G5, G4, G3, G2, G1 and G8 in Haydarpasa Harbor in 154sec wave period in columns 4, 5, 6 respectively. Sinusoidal line crest 1m wave amplitude is 1km far from the main breakwater. X coordinate of the gauge point (second column), Y coordinate of the gauge point (third column).

Gauge No	X-coord (deg)	Y-coord (deg)	Max. Water Surface Elevation (m)	Max. Current (m/s)	Min. Rouse Number
G7	29.0182	40.9976	1.3	0.9	2.1
G6	29.0153	41.0003	0.8	0.8	2.4
G5	29.0124	41.0003	0.7	1.1	1.6
G4	29.0106	41.0017	0.9	0.7	2.5
G3	29.0130	41.0029	1.3	1.8	1.7
G2	29.0123	41.0042	1.2	0.3	7.5
G1	29.0082	41.0047	0.7	1.2	1.7
G8	29.0135	40.9978	0.5	2.3	0.9

Table 6.5. Maximum water surface elevation, maximum current velocity and minimum Rouse Number in G7, G6, G5, G4, G3, G2, G1 and G8 in Haydarpasa Harbor in 200sec wave period in columns 4, 5, 6 respectively. Sinusoidal line crest 1m wave amplitude is 1km far from the main breakwater. X coordinate of the gauge point (second column), Y coordinate of the gauge point (third column).

Gauge No	X-coord (deg)	Y-coord (deg)	Max. Water Surface Elevation (m)	Max. Current (m/s)	Min. Rouse Number
G7	29.0182	40.9976	2.2	0.7	2.4
G6	29.0153	41.0003	1.1	1.1	1.6
G5	29.0124	41.0003	0.8	1.8	1
G4	29.0106	41.0017	1.2	1.5	1.3
G3	29.0130	41.0029	2.2	2.6	0.6
G2	29.0123	41.0042	2.5	0.6	4
G1	29.0082	41.0047	1	2.1	0.9
G8	29.0135	40.9978	2	3.2	0.5

Table 6.6. *Maximum water surface elevation, maximum current velocity and minimum Rouse Number in G7, G6, G5, G4, G3, G2, G1 and G8 in Haydarpasa Harbor in 800sec wave period in columns 4, 5, 6 respectively. Sinusoidal line crest 1m wave amplitude is 1km far from the main breakwater. X coordinate of the gauge point (second column), Y coordinate of the gauge point (third column).*

Gauge No	X-coord (deg)	Y-coord (deg)	Max. Water Surface Elevation (m)	Max. Current (m/s)	Min. Rouse Number
G7	29.0182	40.9976	1.7	0.6	5.1
G6	29.0153	41.0003	1.6	0.5	3.5
G5	29.0124	41.0003	1.5	1.1	2
G4	29.0106	41.0017	1.4	0.9	2
G3	29.0130	41.0029	1.5	0.7	2.7
G2	29.0123	41.0042	1.5	0.2	10
G1	29.0082	41.0047	1.2	2.4	0.8
G8	29.0135	40.9978	1.6	1.5	1.3

Table 6.7. *Maximum water surface elevation, maximum current velocity and minimum Rouse Number in G7, G6, G5, G4, G3, G2, G1 and G8 in Haydarpasa Harbor in 900sec wave period in columns 4, 5, 6 respectively. Sinusoidal line crest 1m wave amplitude is 1km far from the main breakwater. X coordinate of the gauge point (second column), Y coordinate of the gauge point*

Gauge No	X-coord (deg)	Y-coord (deg)	Max. Water Surface Elevation (m)	Max. Current (m/s)	Min. Rouse Number
G7	29.0182	40.9976	1.9	0.3	5.2
G6	29.0153	41.0003	1.8	0.4	5.8
G5	29.0124	41.0003	1.6	0.8	2.4
G4	29.0106	41.0017	1.6	0.7	2.4
G3	29.0130	41.0029	1.6	0.6	2.5
G2	29.0123	41.0042	1.6	0.2	10
G1	29.0082	41.0047	1.5	2.4	0.8
G8	29.0135	40.9978	1.7	1.2	1.2

G8 in the harbor entrance is one of the critical points for current amplification. The results also show that the minimum Rouse Number takes place mostly in G3, where the maximum current velocity exists. Also it is seen that minimum Rouse Number in all selected gauges are 0.8 which represents the sediment motion does not have wash load pattern. They are all less than 1.2 which means that the sediment movement there has suspended load condition.

The minimum Rouse Number for the simulation periods is approximately equal to 0.055 which is less than 0.8 and the movement is wash load. These points are the corner points but the Figure 6.17 and Figure 6.18 shows that for 1m wave amplitude for all wave periods the sediment movement in the inner rhombohedral shaped basins is in bed load form in resonance periods which leads to deposition in that part of the basin and initiation of motion occurs for non-resonance periods. Also the current is vortex as the velocity vectors show.

When the input wave amplitude is 2m then the Rouse Number is changed to suspended load for resonance periods and bed load for the non-resonance periods even though the currents are vortex inside the basin. Therefore, the current velocity pattern is as important as its value. Also we conclude that increasing the input wave amplitude leads to fast erosion in the same condition of periods in Haydarpassa Harbor.

Sakakiyama et al. (2011) studied about the effects of tsunami on the topography changes inside the harbors by some experiments and found out deposition occurs where there is vortex current which is mostly in the center of harbors. The results for Haydarpassa Harbor, inside the basin in G3 and G4 satisfies their finding for 1m wave amplitude, but the pattern is changed for 2m wave amplitude which means that the sediment movement in the center of the basins is not just dependent on the current vectors pattern but also the vectors amount are important.

CHAPTER 7

CONCLUSIONS

Coastal structures usually have encountered extreme events with small or huge damaging scales. Oscillation effects and morphological changes are two of main important tasks in the basins under short and long waves attack. Tsunamis as long waves lead to sedimentation as erosion and accretion in the basins which in this study its relation to the current pattern is noticed. Also wave and current amplifications may generally cause problems in ports and harbors especially in shipping and cargo transportation. This dissertation consists of two main parts. The first part, focuses on the wave and current amplification as a result of resonance in the closed basins such as harbors and the second part, involves the sediment movement as morphological changes under tsunami events in ports and harbors.

In this study the existing knowledge and related studies have been compiled and summarized in regard to tsunami induced resonance in basins and therefore, wave and current amplifications are investigated by examples. When the studies on harbour resonance and amplifications are reviewed, one of the relevant approaches to investigate morphological change in the basins can be proposed to focus on a non-dimensional number (Rouse number). Therefore the Rouse number is introduced and the sediment motion according to the Rouse number is categorized in terms of modes of sediment movements. Friction matrix and sediment property matrix are used to represent their values at each grid. The periods of free oscillations of several different closed and semi-enclosed basins with regular or irregular shape and

bathymetry are summarized. Seiche mechanism is explained with a differential equation and the importance of the damping factor is noticed in order to determine the resonant frequency and maximum mass displacement.

In the simulations, the numerical model of NAMI DANCE is used to compute the time history and maximum and/or minimum values of water surface elevations, current velocities, Rouse number, flow depth and momentum flux at selected numerical gauge points and throughout the study domain. Moreover the Fast Fourier Transform technique is used to obtain the energy spectrum from the time history of water surface elevation. The resonance periods are determined by using energy spectrum curves, the maximums in the spectrum curves represent the resonance periods of each mode (resonance periods of free oscillations). Finally the model verifications have been performed by modeling some of simulations given in Yalciner and Pelinovsky (2007) which used TUNAMI N2 model in rectangular basins in order to calculate the basin resonance in enclosed and semi-enclosed basins. Computed results are plotted with different initial parameters to compare and discuss. The results are found in reasonable well agreement with the existing data, and the errors are in acceptable range.

The long wave induced oscillations in enclosed basins and their effect as wave and current amplifications in L-type basins are also investigate. Then the morphology changes as a result of wave amplification and current pattern are studied according to the Rouse number changes in L-type basins. How the shape and dimension parameters of these basins affect the results are also discussed. In the applications, the model similar to the L-type model given in Kakinuma et al. (2009) is used. They have studied the wave amplification during the first and second mode of oscillations. Re-modeling and verifying the problem, the behavior of L-type basin is studied for wave and current amplification and the sediment motion as a morphological change pattern are investigated via 10 selected gauge points.

Sediments movement as a morphology change issue is one of the important and challenging topics which should be paid attention in coastal areas, ports and shallow basins. But the sedimentation as a result of tsunami and other long waves has not been noticed that much until 2011 Great East Japan tsunami event (Tanaka et al., 2012). Therefore Pamuk (2014) studied sediment movement by using Rouse number as a non-dimensional parameter and considering friction matrix in Antalya, Turkey.

In this study, sedimentation by sedimentation in Antalya region is studied using the minimum and time history of Rouse number during 90 minutes simulation. Unlike Pamuk studies, friction is assumed a fixed and constant value; instead a sediment property matrix is assigned to the grids. The general information together with the literature survey is presented to identify the morphological changes due to tsunami inundation. A methodology based on computation of instantaneous Rouse number during tsunami simulation is presented. As a case study a simulation is performed according to a selected tsunami scenario in Eastern Mediterranean basin attacking to (Belek region) at East of Antalya in South of Turkey (Pamuk, 2014). The computed time histories of water level, current velocity, flow depth and Rouse number change at the border of the study domain is inputted as the triggering wave to the study domain.

The aim is to investigate the tsunami motion and calculate the respective sediment movement by computing the spatial and temporal change of Rouse number under tsunami inundation according to the approach given in Yeh et al. (2008). The spatial distribution of sediment properties (diameter, fall velocity and density) is used and a sediment property matrix is developed for the computation of Rouse Number. The instantaneous current velocities at every grid point are used to compute the instantaneous Rouse number from sediment property matrix at each time step during simulations. But Pamuk (2014) calculated the value of sediment property equal to a constant value representing all grid locations as 3.1509. However using the sediment property matrix to calculate the Rouse Number in Antalya does not properly compute the results in comparison to the case of using a constant value for whole domain.

According to the results of simulations, it is observed that the approach using Rouse number to investigate sediment movement is reasonable if the data is sufficiently accurate and employment of spatial distribution of sediment property matrix.

The results showed that the bed material near the shore will certainly move under any tsunami action since the sediment diameter of bed material is small and the current speed of water is high in shallow and near shore regions. The movement of bed material is also observed far distances from the shore at the low elevation areas and river beds at Belek Region. Along with the sediment property matrix, the friction matrix (representing friction coefficients at every grid location) may be helpful to achieve more accurate results of current and other parameters in simulations.

The main concluding remarks achieved in this study are presented in the following:

The corner points on the sides of the L-type basin are always the critical points (G63, G57). The pattern of sediment motion in these mentioned two corner points depend on both current pattern and amount. In vortex currents, if the current is large the sediment move in wash load form but if the current is small enough sediment motion are in bed load mode and therefore, erosion is expected. In all other points, wave and current amplify simultaneously if the wave period meets the resonance period in related basin. It is noticeable that in interior side of L shape basin, the amplification is higher than the exterior side of it. Large periods affect the end parts of the basin more than the smaller wave periods. This phenomenon is more sensible in wave amplification and not in the current amplifications. The effect of the L-type basin's side dimensions is negligible. The amplification factor especially for the current is a little larger in vertical part of the basin (before bending) when its dimension is smaller.

The aim of re-modeling of some of Pamuk (2014) simulations in this thesis are; To check performance of the module of NAMI DANCE which was added to calculate the Rouse number directly as the model output; To investigate the effect of applying

sediment property matrix on the Rouse number results; To obtain time history of Rouse number in certain gauges during the simulation. The achieved Rouse number values show that using friction matrix or sediment property matrix in Belek region does not change the results sensible.

Using Rouse number as a controlling parameter may reasonably predict the level of morphological changes in the study region. The results for Belek region show that near the shoreline, the sediment movement is mostly in the form of wash load.

When going towards the land, the sediment movement dependent on the current velocity and Rouse number value turns to the form of suspended load or bed load or even no motion according to the Rouse number. Hence, we can generally conclude that the erosion in shorelines and accretion far from the shorelines are dependent on the mentioned criteria in this study. Results obtained from this study emphasize that even if the flow depth and current velocity are large, the sediment motion would not be in the wash load form if the region is far from the shoreline.

The morphology change, resonance periods, wave and current amplifications discussed throughout this study are also applied to a case study in Haydarpaşa Harbor, Turkey. According to the incident wave amplitudes used in this study, although currents are vortex inside the basin, the Rouse number values are found to be suspended load in resonance periods and bed load in the non-resonance periods. Therefore, the current pattern becomes important. Moreover, we conclude that increasing the input wave amplitude causes fast erosion in the same condition wave periods in Haydarpaşa Harbor. These results are in agreement with Sakakiyama et al. (2011), which studied the effects of tsunami on the topography changes inside the harbors by some experiments and found out deposition occurs where there is vortex current which is mostly in the center of harbors. According to the experience gained in this study, it can also be indicated that the locally increased current velocities as well as current pattern are also important.

Suggestions for Future Studies:

In the sediment transport studies in this thesis friction coefficient is used as a constant value during the simulations but the sediment properties are assigned as a matrix. In order to achieve more accurate results of current velocity, water surface elevation and other parameters in simulations, it is recommended to apply friction matrix (representing friction coefficients at every grid location) along with the sediment property matrix

The sediment property matrix used in the simulations is developed according to the properties of ground materials in small regions in the study domain. The sediment property matrix can be improved by using the accurate parameters at each point in the study area.

Morphology changes in this dissertation is studied by observing the sediment transport properties according to the Rouse number ranges but the volume of the sediment transport during wave motion can be computed by considering the direction of sediment transport as well.

REFERENCES

- Altinok, Y., Alpar, B., Ersoy, S. and Yalciner, A.C., (2000). Tsunami generation of the Kocaeli Earthquake (August 17th 1999) in the Izmit Bay: coastal observations, bathymetry and seismic data. Turkish Journal of Marine Sciences, Institute of Marine Sciences and Management, University of İstanbul. December, 1999.
- Altinok, Y., Ersoy, S., Yalciner, A. C., Alpar B., Kuran U., (2001). Historical tsunamis in the Sea of Marmara. International Tsunami Symposium ITS 2001, Seattle, August 7-9, 2001, 527-535
- Amanda R. Admire, Lori A. Dengler, Gregory B. Crawford, Burak U. Uslu, Jose C. Borrero, S. Dougal Greer, and RICK I. WILSON, 1982: Long-period motions of a moored ship induced by harbor oscillations, Coast. Eng. Japan, 25, 261-275.
- Ayca, A. (2012). Development of a Web GIS-Based Tsunami Inundation Mapping Service; A Case Study For Marmara Sea Region, Master of Science Thesis, Middle East Technical University, Department of Civil Engineering, Ocean Engineering Research Center, Ankara, Turkey.
- Carr, J. H., Long period waves or surges in harbors, Trans. ASCE, 118, Paper no. 2556 (1953), 588-603.
- Djumagaliev, E.A. Kulikov, and S.L. Soloviev, 1993: Analysis of ocean level oscillations in Malokurilsk Bay caused by tsunami of 16 February 1991, Science Tsunami Hazards, 11, (1), 47-58.

- Dongarra, J.; Sullivan, F. (January 2000). "Guest Editors Introduction to the top 10 algorithms". *Computing in Science Engineering* 2 (1): 22-23. doi:10.1109/MCISE.2000.814652. ISSN 1521-9615.
- Ergin, M., Keskin, S., Dogan, A. U., Kadioglu, Y. K., & Karakas, Z. (2007). "Grain size and heavy mineral distribution as related to hinterland and environmental conditions for modern beach sediments from the Gulfs of Antalya and Finike, eastern Mediterranean," *Marine Geology*, 240(1-4), 185–196. doi:10.1016/j.margeo.2007.02.006
- Feldens, P., Schwarzer, K., Szczuciński, W., & Stattegger, K. (2009). "Impact of 2004 Tsunami on Seafloor Morphology and Offshore Sediments, Pakarang Cape," Thailand. *Polish J. of Environ. Stud.*, 18(1), 63–68.
- Girolamo, P. D., 1996: An experiment on harbour resonance induced by incident regular waves and irregular short waves, *Coastal Engineering*, 27, 47-66.
- Heideman, M. T.; Johnson, D. H.; Burrus, C. S. (1984). "Gauss and the history of the fast Fourier transform". *IEEE ASSP Magazine* 1 (4): 14–21. doi:10.1109/MASSP.1984.1162257.
- Henry, R.F., and Murty, T.S., 1995: Tsunami amplification due to resonance in Alberni Inlet: Normal modes, in *Tsunami: Progress in Prediction, Disaster Prevention and Warning*, edited by Y. Tsuchiya and N. Shuto, Kluwer Acad. Publ., Dordrecht, The Netherlands, 117-128.
- Honda, K., Terada, T., Yoshida, Y., and Isitani D., 1908: An investigation on the secondary undulations of oceanic tides, *J. College Sci., Imper. Univ. Tokyo*, 108 p.
- Imamura, F. (1996). Review of Tsunami Simulation with a Finite Difference Method, Long-Wave Runup Models, *Proceedings of the International Workshop, Friday Harbour, USA*, pp. 25-42.
- Ippen, A. (1966). *Estuary and coastline hydrodynamic*. MacGraw-Hill, Inc.

- Kakinuma, T., T. Toyofuku, and T. Inoue. (2009). Numerical analysis of harbor oscillation in harbors of various shapes, Proceedings of Coastal Dynamics 2009, World Scientific Publishing Co.
- Keshtpour, M., Puleo, J. A., Shi, F. (2014a). Downtide beach erosion adjacent to the Indian River inlet, Delaware, USA, Journal of Shore & Beach, Vol. 82, pp. 31-41.
- Keshtpour, M., Puleo, J. A., Shi, F. (2015). Numerical simulation of nearshore hydrodynamics and sediment transport downtide of tidal inlet, Journal of Waterway, Port Coastal and Ocean Engineering, Vol. 141, p. 16.
- Kian R., Yalciner A.C., Zaytsev A (2014a). Evaluating the performance of tsunami propagation models // Proc. Bauhaus Summer School in Forecast Engineering: Global climate change and the challenge for built environment (17-29 August 2014, Weimar, Germany). 2014. 10 pages. https://www.uni-weimar.de/summerschool/fileadmin/media/FE_Paper/KianRozita_FE2014.pdf [last accessed on 01.11.2015]
- Kian R., Yalciner A.C. and Zaytsev A., (2014b). Dispersion of long wave on varying bathymetry// Coastal Engineering Proceedings, Vol. 34, p.19.
- Kian R., Yalciner A.C. and Zaytsev A., Aytore, B., (2015a). Wave amplification and resonance in enclosed basins; A case study in Haydarpasa Port of Istanbul// Proc. Current, Waves and Turbulence Measurement (CWTM), IEEE 2015, Vol. 11, 7pages. doi: 10.1109/CWTM.2015.7098153
- Kian R., Yalciner A.C. and Zaytsev A., Aytore, B., (2015b). Tsunami induced resonance in enclosed basins; Case study of Haydarpasa Port in Istanbul// EGU General Assembly Conference Abstracts, Vol. 17, p.154.
- Kian R., Pamuk, A., Yalciner A.C. and Zaytsev A., (2015c). Effects of tsunami parameters on the sedimentation// Proc. Coastal Sediments 2015, Vol. 8, pp. 67-74.

- Knapp, R. T. and Vanoni, V. A., Wave and surge study for the Naval Operating Base, Terminal Island, California, Calif. Inst. Tech., Hyd. Structures Lab., January, 1945.
- Korgen, B.J., 1995: Seiches, *American Scientist*, 83, 330-341.
- Lee, J.J., 1971: Wave induced oscillations in harbors of arbitrary geometry, *J. Fluid Mech.*, 45, 375-394.
- Le Méhauté, B., 1954. Two-Dimensional seiche in a basin subjected to incident wave, *Peoc. Fifth Conf. on Coastal Eng.*, pp. 119-149, 1954.
- Le Méhauté, B., 1960. Periodical gravity wave on a discontinuity, *J. Hydraulics Div., ASCE*, pp. 11-41, Nov. 1960.
- Li, L., Qiu, Q., & Huang, Z. (2012). Numerical modeling of the morphological change in Lhok Nga, west Banda Aceh, during the 2004 Indian Ocean tsunami: understanding tsunami deposits using a forward modeling method. *Natural Hazards*, 64(2), 1549–1574. doi:10.1007/s11069-012-0325-z
- Liu, P. L.-F., Cho, Y.-S. Yoon, S.B., Seo. S.N. (1994). Numerical Simulations of the 1960 Chilean Tsunami Propagation and Inundation at Hilo, Hawaii, *Recent Development in Tsunami Research*, pages 99–115, Kluwer Academic Publishers, 1994.
- Liu, P. L.-F., Woo, S-B., Cho, Y.-S. (1998). *Computer Programs for Tsunami Propagation and Inundation*, Technical report, Cornell University, 1998.
- Miles, J., and Munk, W., 1961: Harbor paradox, *J. Waterways Harbor Division, ASCE*, 87, 111-130.
- Miller, G.R., 1972: Relative spectra of tsunamis: Hawaii Inst. Geophys, *HIG-72-8*, 7 p.
- Monserrat, S., Ibberson, A., and Thorpe, A.J., 1991: Atmospheric gravity waves and the “rissaga” phenomenon, *Q. J. R. Meteorol. Soc.*, 117, 553-570.

- Mori, N., Takahashi, T. & The 2011 Tohoku Earthquake Tsunami Joint Survey Group (2012). Nationwide post event survey and analysis of the 2011 Tohoku earthquake tsunami. *Coast. Eng. J.* 54(1), 1250001.
- Murty, T.S., 1977: Seismic Sea Waves - Tsunamis. *Bull. Fish. Res. Board Canada* 198, Ottawa, 337 p.
- Nakano, M., 1933: Possibility of excitation of secondary undulations in bays by tidal or oceanic currents, *Proc. Imp. Acad. Japan*, 9, 152-155.
- Nakano, M., and T. Abe, 1959: Standing oscillation of bay water induced by currents, *Records Oceanogr. Works in Japan, Spec. No. 3*, 75-96.
- Nakano, M., and Unoki, S., 1962: On the seiches (secondary undulations of tides) along the coast of Japan, *Records Oceanogr. Works Japan, Spec. No.6*, 169-214.
- NAMI DANCE Manual (2010). Developed by Zaytsev, C., Yalciner, Pelinovsky, Kurkin. Tsunami Simulation/Visualization Code NAMI DANCE versions 4.9. <http://www.namidance.ce.metu.edu.tr> (Reviewed on July 3, 2014).
- NOAA Technical Report NOS CO-OPS 079 An Examination of the June 2013 East Coast Meteotsunami Captured By NOAA Observing Systems, Silver Spring, Maryland November 2014
- Ozer, C. and Yalciner, A.C. (2011). Sensitivity Study of Hydrodynamic Parameters during Numerical Simulations of Tsunami Inundation, *Pure Appl. Geophys.*, pp. 2083-2095.
- Ozer, C., Karakus, H., Yalciner, A.C. (2008). Investigation of Hydrodynamic Demands of Tsunamis in Inundation Zone, *Proceedings of 7th International Conference on Coastal and Port Engineering in Developing Countries*, Dubai, UAE, February 24-28.
- Ozer, C. (2012). "Tsunami hydrodynamics in coastal zones," PhD Thesis, Middle East Technical University.

- Pamuk, A. (2014). "Assessment of Inland tsunami parameters and their effects on morphology," MS Thesis, Middle East Technical University.
- PIANC (2009). Tsunami Disasters in Ports due to the Great East Japan Earthquake, PIANC Report 53, PIANC.
- PIANC (2014). Tsunami Disasters in Ports due to the Great East Japan Earthquake, PIANC Report 122, PIANC, Bruxelles.
- Pritchard, D., & Dickinson, L. (2008). Modelling the sedimentary signature of long waves on coasts: implications for tsunami reconstruction. *Sedimentary Geology*, 206(1-4), 42–57. doi:10.1016/j.sedgeo.2008.03.004
- Proudman, J. (1953), "Dynamic Oceanography," John Wiley and Sons., New York
- Raichlen, F., 1966: Harbor resonance, in *Estuary and Coastline Hydrodynamics*, Edited by A.T. Ippen, McGraw Hill Book Comp., New York, 281-340.
- Rabinovich, A.B., 1997: Spectral analysis of tsunami waves: Separation of source and topography effects, *J. Geophys. Res.*, 102, (C6), 12,663-12,676.
- Rabinovich, A.B., R.E. Thomson, and F.E. Stephenson, 2006: The Sumatra tsunami of 26 December 2004 as observed in the North Pacific and North Atlantic oceans, *Surveys in Geophysics*, 27, 647-677.
- Rabinovich, A.B., and R.E. Thomson, 2007: The 26 December 2004 Sumatra tsunami: Analysis of tide gauge data from the World Ocean Part 1. Indian Ocean and South Africa, *Pure Appl. Geophys.*, 164, (2/3), 261-308.
- Rabinovich, A. B. (2008), Seiches and Harbour Oscillations. *Handbook of Coastal and Ocean Engineering*, edited by Y. C. Kim, World Sci., Singapore.
- Sakakiyama, T., Matsuyama, M., & Yoshii, T. (2011). "Experimental study on bottom topography change in harbor due to tsunami," *Coastal Engineering Proceedings*, 1(32), sediment-76.

- Sawaragi, T., and Kubo, M., 1982: Long-period motions of a moored ship induced by harbor oscillations, *Coast. Eng. Japan*, 25, 261-275.
- Shimamoto, T., Tsutsumi, A., Kawamoto, E., Miyawaki, M., And Hiroshi, S., (1995), Field survey report on tsunami disasters caused by the 1993 Southwest Hokkaido earthquake, *Pure Appl. Geophys.* 144(3-4), 665-691.
- Sorensen, R.M. and E.F. Thompson, 2002: Harbor hydrodynamics, in *Coastal Engineering Manual, Part II*, U.S. Army Corps. Of Engineers, Washington, D.C., New York, Chapter 7, 1-92.
- Soulsby, R. (1997). *Dynamics of marine sands*. Thomas Telford Publications, London (270 pp. ISBN 0 7277 2584 X).
- Strang, Gilbert (May-June 1994). "Wavelets". *American Scientist* 82 (3): 253. JSTOR 29775194.
- Sugawara, D., Goto, K., & Jaffe, B. E. (2014a). Numerical models of tsunami sediment transport — Current understanding and future directions. *Marine Geology*, 352, 295-320. doi:10.1016/j.margeo.2014.02.007
- Sugawara, D., Takahashi, T., & Imamura, F. (2014b). Sediment transport due to the 2011 Tohoku-oki tsunami at Sendai: Results from numerical modeling. *Marine Geology*. doi:10.1016/j.margeo.2014.05.005
- Sumer, B. M. (2014). Flow-structure-seabed interactions in coastal and marine environments. *Journal of Hydraulic Research*, 52(1), 1-13. doi:10.1080/00221686.2014.881927.
- Synolakis, C.E. (2003). Tsunami and Seiche, in *Earthquake Engineering Handbook*, W.F. Chen and C. Scawthorn (eds), CRC Press, New York, 9-1 to 9-99.
- Synolakis, C. and Bernard, E. (2006). Tsunami Science before and beyond Boxing Day 2004, *Phil. Trans. R. Soc. A* 2006, Vol. 364, pp. 2231-2265, doi: 10.1098/rsta.2006.1824

- Takahashi, T., N. Shuto, F. Imamura and D. Asai (2000). “Modelling sediment transport due to tsunamis with exchange rate between bed load layer and suspended load layer,” Proceedings of International Conference on Coastal Engineering 2000, Vol.2, ASCE, pp.1508-1519.
- Tanaka, H., Tinh, N. X., Hirao, R., Pradjoko, E., Mano, A, Udo, K. (2012). “Coastal and estuarine morphology changes induced by the 2011 great East Japan earthquake tsunami,” Coastal Engineering Journal, 54(01), 1-25.
- Titov, V. and Synolakis, C.E. (1998). Numerical modeling of tidal wave run-up, Journal of Waterway, Port, Coastal and Ocean Engineering, Vol. 124 (4), pp. 157-171.
- Titov, V.V., A.B. Rabinovich, H. Mofjeld, R.E. Thomson, and F.I. González, 2005: The global reach of the 26 December 2004 Sumatra tsunami, Science, 309, 2045-2048.
- Tsutsumi, A., Shimamoto, T., Kawamoto, E., And Logan, J., (2000), Nearshore flow velocity of Southwest Hokkaido earthquake tsunami, J. Waterw., Port, Coastal, Ocean Eng. 126(3), 136–143.
- TUNAMI-N2 (2001). “Tsunami Modelling Manual (Tunami Model)” by Imamura, F., Yalciner, A. C. and Ozyurt, G.
- Van Dorn, W.G., 1984: Some tsunami characteristics deducible from tide records, J. Phys. Oceanogr. 14, 353-363.
- Velioglu, D., Yalciner A.C. Kian, R. and Zaytsev A., Aytore, B., (2015). Validation of Numerical Codes to Compute Tsunami Runup And Inundation// EGU General Assembly Conference Abstracts, Vol. 17, p.8419.
- Weiss, R. (2004). Modeling of generation , propagation and runup of tsunami waves caused by oceanic impacts. Westfälische Wilhelms-Universität Münster.

- Wemelsfelder, P. J. (1954), The disaster in the Netherlands caused by the storm food of February 1, 1953, Proc. Fourth Conf. Coastal Eng., Berkely, Calif.: The Engineering Foundation Council on Wave Reseach, 1954, pp. 258-71
- Wiegel, R.L., 1964: Tsunamis, storm surges, and harbor oscillations. Ch. 5 in Oceanographical Engineering, Prentice-Hall, Englewood Cliffs, N.J., 95-127.
- Wilson, B., 1972: Seiches, Advances in Hydrosiences, 8, 1-94.
- Yalciner, A. C., Kuran, U., Akyarli, A., and Imamura, F., (1995), An investigation on the propagation of tsunamis in the Aegean Sea by mathematical modeling, in Tsuchiya, Y., and Shuto, N., eds., Tsunami: Progress in prediction, disaster prevention and warning: Dordrecht, Kluwer Academic Publishers, p. 55–70.
- Yalciner, A. C., Pelinovsky, E., Cakiroglu, Yesim, Imamura, F., Akyarli, A. (1996a). The attenuation of tsunami height in the irregular bathymetry. In: International Conference on Mitigation of Natural Hazards”, HAZARDS’96 by Natural Hazards Society, 22–26 July, 1996, Toronto, Canada.
- Yalciner, A. C., Pelinovsky, E., Cakiroglu Yesim, Imamura, F. (1996b). The Properties of resonance due to the geometry of the basins XXV. General Assembly of European Geophysical Society, Session NH5, Tsunamis Impacting on the European Coasts: Modelling, Observation and Warning, 6-11, May, 1996, The Hague, Netherlands.
- Yalciner A. C. Alpar B., Altinok Y., Ozbay I., Imamura F., (2002). Tsunamis in the Sea of Marmara: Historical documents for the Past, models for future. Special Issue of Marine Geology, 190, 445-463
- Yalciner, A. C. and Pelinovsky, E. N., (2007): A short cut numerical method for determination of periods of free oscillations for basins with irregular geometry and bathymetry, Ocean. Eng., 34(5–6), 747– 757.
- Yalciner, A.C., Ozer, C., Karakus, H., Zaytsev, A., Guler, I. (2010). Evaluation of Coastal Risk at Selected Sites against Eastern Mediterranean Tsunamis,

- Proceedings of 32nd International Conference on Coastal Engineering (ICCE 2010), Shanghai, China.
- Yalciner, A. C., Zaytsev, A., Aytore, B., Heidarzadeh, M., Kian, R., & Imamura, F. (2014). A possible submarine landslide and associated tsunami at the northwest Nile delta, Mediterranean sea. *Oceanography*, 27(2), 68–75.
- Yalciner, A. C. Kian, R., Aytore, B. and Zaytsev, A., “Harbors and Tsunami Threat; A case study in the Sea of Marmara,” Proceedings of 36th IAHR World Congress, 4pages, Delft, Netherland, 28Jun-3July, 2015.
- Yao, L.S., 1999. A resonant wave theory. *Journal of Fluid Mechanics*, 395 237-251. (Printed in the United Kingdom c 1999. Cambridge University Press, Cambridge).
- Yeh, H. and Li, W. (2008). “Tsunami scour and sedimentation,” Proc. 4nd International Conference on Scour and Erosion, 95-106.
- Yoshii, T., Ikeno, M., Matsuyama, M., & Fujii, N. (2011). Pick-up rate of suspended sand due to tsunami. *Coastal Engineering Proceedings*, 1(32), sediment-12.
- Zahibo, N., Pelinovsky, E., Yalciner, A.C., Kurkin, A., Kozelkov, A., Zaitsev, A. (2003). Modeling the 1867 Virgin Island Tsunami, *Journal of Natural Hazards and Earth System Sciences*, European Geosciences Union, 3, June-2003, pp. 367-376
- Zaitsev, A., Yalciner, A. C., Pelinovsky, E., Kurkin, A., Ozer, C., Insel, I., Karakus, H., Ozyurt, G. (2008). Tsunamis in Eastern Mediterranean, Histories, Possibilities and Realities, Proceedings of 7th International Conference on Coastal and Port Engineering in Developing Countries, Dubai, UAE, February 24-28
- https://en.wikipedia.org/wiki/Fast_Fourier_transform [last accessed on 04.11.2015]

APPENDIX A

A. APPLIED EQUATIONS IN THE MODEL

A.1. Non-Linear Shallow Water Equation (NLSWE)

Equations used in the numerical model, NAMI DANCE, are the shallow water equations and based on assumptions; the equations for conservation of mass and momentum in two-dimensional unsteady solution are as according to equations [A.1], [A.2], [A.3] and [A.4]:

$$\frac{1}{b + \eta} \frac{\partial \eta}{\partial t} + \frac{\partial u}{\partial x} + \frac{\partial v}{\partial y} = 0 \quad [\text{A.1}]$$

$$\frac{\partial u}{\partial t} + u \frac{\partial u}{\partial x} + v \frac{\partial u}{\partial y} + \frac{1}{\rho} \frac{\partial p}{\partial x} + \frac{1}{\rho} \left(\frac{\partial \tau_{xx}}{\partial x} + \frac{\partial \tau_{xy}}{\partial y} \right) = 0 \quad [\text{A.2}]$$

$$\frac{\partial v}{\partial t} + u \frac{\partial v}{\partial x} + v \frac{\partial v}{\partial y} + \frac{1}{\rho} \frac{\partial p}{\partial y} + \frac{1}{\rho} \left(\frac{\partial \tau_{xy}}{\partial x} + \frac{\partial \tau_{yy}}{\partial y} \right) = 0 \quad [\text{A.3}]$$

$$g + \frac{1}{\rho} \frac{\partial p}{\partial z} = 0 \quad [\text{A.4}]$$

where t is time, η is water surface elevation above still water level up to free surface. x , y and z are the axes of Cartesian coordinate system that z is in vertical direction, u and v are the depth averaged velocities of water particles in x and y directions respectively, τ_{ij} is the shear stress in i direction on the j normal plane, g is gravitational acceleration and ρ is the density of water. In order to solve equations

[A.1], [A.2], [A.3] and [A.4], boundary condition should be applied. The dynamic and kinematic boundary conditions at the sea surface and the kinematic boundary condition at the impermeable sea bottom are given as equations [A.5], [A.6] and [A.7] respectively.

$$p = 0 \quad \text{at } z = \eta \quad [\text{A.5}]$$

$$w = \frac{\partial \eta}{\partial t} + u \frac{\partial \eta}{\partial x} + v \frac{\partial \eta}{\partial y} \quad \text{at } z = \eta \quad [\text{A.6}]$$

where w is the depth averaged velocities of water particles in z direction.

$$w = -u \frac{\partial b}{\partial x} - v \frac{\partial b}{\partial y} \quad \text{at } z = -b \quad [\text{A.7}]$$

Considering the boundary condition at the free surface with hydrostatic pressure assumption, the equation of momentum in z -direction is derived as Eq. [A.8]:

$$p = \rho g (\eta - z) \quad [\text{A.8}]$$

Applying Leibnitz Rule and considering the boundary conditions at the surface and bottom of sea, the two-dimensional Shallow Water Equations is derived as equations [A.9], [A.10] and [A.11] (Ozer, 2012);

$$\frac{\partial \eta}{\partial t} + \frac{\partial M}{\partial x} + \frac{\partial N}{\partial y} = 0 \quad [\text{A.9}]$$

$$\frac{\partial M}{\partial t} + \frac{\partial}{\partial x} \left(\frac{M^2}{D} \right) + \frac{\partial}{\partial y} \left(\frac{MN}{D} \right) + gD \frac{\partial \eta}{\partial x} + \frac{\tau_x}{\rho} = A \left(\frac{\partial^2 M}{\partial x^2} + \frac{\partial^2 M}{\partial y^2} \right) \quad [\text{A.10}]$$

$$\frac{\partial N}{\partial t} + \frac{\partial}{\partial x} \left(\frac{MN}{D} \right) + \frac{\partial}{\partial y} \left(\frac{N^2}{D} \right) + gD \frac{\partial \eta}{\partial y} + \frac{\tau_y}{\rho} = A \left(\frac{\partial^2 N}{\partial x^2} + \frac{\partial^2 N}{\partial y^2} \right) \quad [\text{A.11}]$$

where D is the total water depth, $D = b + \eta$, τ_x and τ_y are the bottom shear stresses, M and N are the discharge fluxes in the x - and y - directions respectively, A is the

eddy viscosity constant. The discharge fluxes are defined by equations [A.12], [A.13].

$$M = \int_{-b}^{\eta} u d\zeta = u(b + \eta) = uD \quad [\text{A.12}]$$

$$N = \int_{-b}^{\eta} v d\zeta = v(b + \eta) = vD \quad [\text{A.13}]$$

where \bar{u} and \bar{v} are the depth average velocities in x and y directions respectively. When the flow is considered uniform, the shear stress terms are defined as equations [A.14], [A.15].

$$\frac{\tau_x}{\rho} = \frac{1}{2g} \frac{f}{D^2} M \sqrt{M^2 + N^2} \quad [\text{A.14}]$$

$$\frac{\tau_y}{\rho} = \frac{1}{2g} \frac{f}{D^2} N \sqrt{M^2 + N^2} \quad [\text{A.15}]$$

where f is the friction coefficient. Manning's roughness n is generally estimated to be assumed equal to the friction coefficient f in most of the engineering problems and it is represented in Eq. [A.16]. The value of Manning's roughness is considered equal to 0.025 in this thesis. Substituting the n , the shear stress is obtained in [A.17], [A.18].

$$n = \sqrt{\frac{fD^{1/3}}{2g}} \quad [\text{A.16}]$$

$$\frac{\tau_x}{\rho} = \frac{n^2}{D^{7/3}} M \sqrt{M^2 + N^2} \quad [\text{A.17}]$$

$$\frac{\tau_y}{\rho} = \frac{n^2}{D^{7/3}} N \sqrt{M^2 + N^2} \quad [\text{A.18}]$$

Since the horizontal eddy viscosity can be neglected in tsunami case due to its value in comparison to the bottom friction, therefore, equations [A.9], [A.10] and [A.11] become to equations [A.19], [A.20] and [A.21] in order to be solved in NAMI DANCE.

$$\frac{\partial \eta}{\partial t} + \frac{\partial M}{\partial x} + \frac{\partial N}{\partial y} = 0 \quad [\text{A.19}]$$

$$\frac{\partial M}{\partial t} + \frac{\partial}{\partial x} \left(\frac{M^2}{D} \right) + \frac{\partial}{\partial y} \left(\frac{MN}{D} \right) + gD \frac{\partial \eta}{\partial x} + \frac{n^2}{D^{7/3}} M \sqrt{M^2 + N^2} = 0 \quad [\text{A.20}]$$

$$\frac{\partial N}{\partial t} + \frac{\partial}{\partial x} \left(\frac{MN}{D} \right) + \frac{\partial}{\partial y} \left(\frac{N^2}{D} \right) + gD \frac{\partial \eta}{\partial y} + \frac{n^2}{D^{7/3}} N \sqrt{M^2 + N^2} = 0 \quad [\text{A.21}]$$

A.2. Stability of the Model

The scheme used in NAMI DANCE is leap-frog in finite difference technique and the stability of the calculations is achieved when Courant-Friedrichs-Lewy (CFL) condition in simulations satisfied. It means that the numerical speed ($\frac{\Delta x}{\Delta t}$) must be faster than the maximum speed of the tsunami (c_{\max}) which practically means the waves should move from one grid in x or y direction faster than the maximum speed of the wave moving via that grid during one time step of the simulation.

This condition is presented in Eq. [A.22]

$$\frac{\Delta x}{\Delta t} > c_{\max} \quad , \quad \frac{\Delta y}{\Delta t} > c_{\max} \quad [\text{A.22}]$$

where $c_{\max} = \sqrt{gD_{\max}}$ and $D_{\max} = (b + \eta)_{\max}$.

CURRICULUM VITAE

PERSONAL INFORMATION

Surname, Name: Kian, Rozita
Nationality: Iranian
Date and Place of Birth: 21 March 1984, Tabriz
Marital Status: Single
Phone: +90 312 210 54 30
email: kian.rozita@gmail.com

EDUCATION

Degree	Institution	Year of Graduation
MS	Sharif Univ. of Tech., Civil Eng., Tehran, Iran	2009
BS	Sharif Univ. of Tech., Civil Eng., Tehran, Iran	2006
High School	Bagherol Olum, Tabriz, Iran	2002

WORK EXPERIENCE

Year	Place	Enrollment
2011-present	METU Department of Civil Engineering Ocean Engineering Research Center	Research/Teaching Assistant
2006-Jun-Sep	Sazeh Consultants Engineering and Construction	Intern Engineering Student

TEACHING EXPERIENCES:

CE761- Marine Hazards and Tsunamis (Guest Lecturer)
CE594- Modeling of Coastal Engineering Problems (Teaching Assistant)
CE596- Coastal Pollution (Teaching Assistant)
CE594- Coastal Engineering (Teaching Assistant)

FOREIGN LANGUAGES

English, Turkish

PUBLICATIONS

Journal Papers:

Yalciner, A.C., A. Zaytsev, B. Aytore, I. Insel, M. Heidarzadeh, **R. Kian**, and F. Imamura. (2014), "A possible submarine landslide and associated tsunami at the Northwest Nile Delta", *Mediterranean Sea. Oceanography*, 27(2):68–75.

Kian, R., Yalciner, A. C. and Zaytsev, A., “Gridding Effect on Tsunami Numerical Modeling”, *Ocean Engineering* (under review).

Kian, R., Yalciner, A. C. and Zaytsev, A., “Change of Sediment inside Harbors due to Long Wave and Tsunami motion”, (to be submitted).

Kian, R., Yalciner, A. C. and Zaytsev, A., “Effects of Harbor Shape on the Sedimentation and Oscillation”, (to be submitted)

Conference Papers and Presentations:

Kian, R., Pamuk, A., Yalciner, A. C., Zaytsev, A., 2015, “Effect of Tsunami Parameters on the Sedimentation”, *Coastal Sediments Conference (CS15)*, in San Diego, California, U.S.A., 11-15 May, 2015.

Kian, R., Yalciner, A. C., Zaytsev, A., Aytore, B., 2015, “Wave Amplification and Resonance in Enclosed Basins; A Case Study in Haydarpasa Port of Istanbul”, *Waves and Turbulence Measurement Workshop (CWTM)*, St.Petersburg, Florida, U.S.A., 2-6 March 2015.

Kian, R., Velioglu, D., Yalciner, A. C., Zaytsev, A., 2015, “Tsunami induced sedimentation in Haydarpasa harbor, Marmara Sea”, *American Geophysical Union (AGU2015)*, San Francisco, California, U.S.A, 14-18 Dec 2015 (accepted).

Velioglu, D., **Kian, R.**, Yalciner, A. C., Zaytsev, A., 2015, “Validation and Performance Comparison of Numerical Codes for Tsunami Inundation”, *American Geophysical Union (AGU2015)*, San Francisco, California, U.S.A, 14-18 Dec 2015 (accepted).

Yalciner, A. C., **Kian, R.**, Aytore, B., Zaytsev, A., 2015, “Harbors and Tsunami Threat; A case study in the Sea of Marmara”, E-Proceedings of the 36th IAHR World Congress, Hague, Netherland, 28 Jun-3 July 2015.

Kian, R., Yalciner, A. C., Zaytsev, A., Aytore, B., 2015, “Tsunami Induced Resonance in Enclosed Basins; Case Study of Haydarpasa Port in Istanbul”, Geophysical Research Abstracts (EGU2015), Vienna, Austria, 12-17 April 2015.

Velioglu, D., Yalciner, A. C., **Kian, R.**, Zaytsev, A., 2015, “Validation of Numerical Codes to Compute Tsunami Runup and Inundation”, Geophysical Research Abstracts (EGU2015), Vienna, Austria, 12-17 April 2015.

Kian, R., Zaytsev, A. and Yalciner, A. C., 2014, “Dispersion of Long Waves on Varying Bathymetry”, 34th International Conference on Coastal Engineering (ICCE 2014), Seoul, Korea, Jun 2014.

Kian, R., Yalciner, A. C. and Zaytsev, A., 2014, “Evaluating The Performance of Tsunami Propagation Models”, Bauhaus Summer School in Forecast Engineering: Global Climate change and the challenge for built environment, Weimar, Germany, 17-29 August 2014.

Kian, R., Zaytsev, A. and Yalciner, A. C., 2013, “The Performance of Tsunami Numerical Models with Dispersion; A Comparative Study between NAMI DANCE and FUNWAVE”, 26th International Tsunami Symposium, Gocek, Turkey, Sep 2013.

Kian, R., Velioglu, D., Yalciner, A. C. and Zaytsev, A., 2014, “Comparing The Performance of Tsunami Numerical Models Nami Dance And Funwave”, 8th Kiyi Muhendisligi Simposiyumu (TMMOB 2014), Istanbul, Turkey, Nov 2014.

Kian, R. and Jamali, M.M., 2009, “Establishment of selective withdrawal in a two-layer reservoir with a bottom sill”, 33rd IAHR Congress on Environmental & Water Resources Institute of ASCE, University of British Columbia, Vancouver, Canada, Aug 2009.

Kian, R. and Jamali, M.M., 2009, “Theoretical and experimental study of selective withdrawal from two layer fluid with sill effects”, 8th International Congress on Civil Engineering, Shiraz University, Shiraz, Iran, May 2009.